

2018

Rotating Magnetometry For Terrestrial And Extraterrestrial Subsurface Explorations

Robert Farrell
University of Vermont

Follow this and additional works at: <https://scholarworks.uvm.edu/graddis>



Part of the [Mechanical Engineering Commons](#)

Recommended Citation

Farrell, Robert, "Rotating Magnetometry For Terrestrial And Extraterrestrial Subsurface Explorations" (2018). *Graduate College Dissertations and Theses*. 945.

<https://scholarworks.uvm.edu/graddis/945>

This Thesis is brought to you for free and open access by the Dissertations and Theses at ScholarWorks @ UVM. It has been accepted for inclusion in Graduate College Dissertations and Theses by an authorized administrator of ScholarWorks @ UVM. For more information, please contact donna.omalley@uvm.edu.

ROTATING MAGNETOMETRY FOR TERRESTRIAL AND EXTRATERRESTRIAL
SUBSURFACE EXPLORATIONS

A Thesis Presented

by

Robert J. Farrell

to

The Faculty of the Graduate College

of

The University of Vermont

In Partial Fulfillment of the Requirements
for the Degree of Master of Science
Specializing in Mechanical Engineering

October, 2018

Defense Date: July 9, 2018

Thesis Examination Committee:

Dryver Huston, Ph.D., Advisor

Mandar Dewoolkar, Ph.D., Advisor

Tian Xia, Ph.D., Chairperson

Yves Dubief, Ph.D.

Cynthia J. Forehand, Ph.D., Dean of the Graduate College

ABSTRACT

Signaling and sensing with rotating magnet sources has both Terrestrial and Extraterrestrial applications. The dual spinning magnet unit presented in this paper is a simple, lightweight solution to help understand soil densities and locate water and ice pockets on Mars. Traditional magnetic telemetry systems that use energy-inefficient large induction coils and antennas as sources and receivers are not practical for extraterrestrial sensing applications. The recent proliferation of strong rare-earth permanent magnets and high-sensitivity magnetometers enables alternative magnetic telemetry system concepts with significantly more compact formats and lower energy consumption. There are also terrestrial applications, for example, subterranean objects such as underground infrastructure and unexploded ordnances (UXO) are often unmapped and difficult to find on Earth. Current ground penetrating radar units are expensive, large, and heavy. Traditional megahertz radio communication systems are often unable to penetrate through multiple feet of earthen and manmade materials and have impractically large energy requirements. Low-power magnetic signaling systems do not suffer from this drawback: low-frequency electromagnetic waves easily penetrate well through several feet of earth and water. The research presented and proposed explores the viability and possibility to develop a unit that will induce an oscillating magnetic field to reliably locate buried pipes, soils, and unexploded ordnances (UXO) while remaining lightweight and cost effective. The Dual Rotating Magnet (DRM) design will be tested to assess the following hypotheses for both Mars and Earth applications: 1) detect differences in soil densities, 2) detect water and ice pockets at shallow depths in the subsurface, and 3) reliably detect subterranean objects of interest.

ACKNOWLEDGEMENTS

Thank you to my committee for your help through this process. I would like to especially thank Dr. Huston and Dr. Dewoolkar for their endless support and invaluable advice and guidance. This research was funded by the Vermont Space Grant Consortium under NASA Cooperative Agreement NNX15AP86H and the U.S. National Science Foundation grants 1647095 and 1640687.

TABLE OF CONTENTS

	Page
ACKNOWLEDGEMENTS.....	ii
LIST OF FIGURES.....	vii
CHAPTER 1: Introduction	1
1.1 Literature Review	1
1.1.1 Martian Soil.....	2
1.1.2 Martian Rovers	5
1.1.3 Magnetometers	7
1.1.4 Electromagnetic Induction	10
1.1.5 Eddy Currents.....	12
CHAPTER 2: Quasi-Static Multi-Dipole Model of Rotating Magnet Arrays.....	14
2.1 Multiple Dipole Local to Global Coordinate Theory	14
CHAPTER 3: Mathematical Analysis.....	23
3.1. Local 2-D Mathematical Analysis.....	23
3.2. Halbach Array Analysis.....	26
3.2.1 Mathematical Confirmation	26
3.2.2 Analysis of Halbach Array.....	32
3.3 Rotating Dual Magnet Analysis	33
3.4. FEA Comparison.....	39
3.4.1 Dual Rotating Magnet Comparison.....	39
3.4.2 Halbach Array FEA Analysis.....	41

3.5.1 Dual Magnet FEA.....	43
3.5.2 Halbach Array FEA	50
3.5.3 Discussion	51
Chapter 4: Equipment Design.....	53
4.1 Proposed Designs	53
4.1.1 Dual Rotating Magnet Unit.....	53
4.1.2. Spinning Halbach Array Unit.....	54
4.1.3 Spinning Halbach Array with Two Degrees of Freedom	55
4.1.4 Spinning Halbach Array with Five Degrees of Freedom.....	56
4.2 Preliminary Designs	57
4.3 Final Design	60
4.3.1 Motor Sizing.....	61
4.3.2 Magnetometer.....	65
4.3.3 Motion Control and Electronic Gearing.....	73
4.3.2.1 Motion Controller	74
4.3.3.2 Electronic Gearing	78
4.3.3.3 Electronic Gearing Test.....	84
4.3.4 Final Design	86
Chapter 5: Testing Results.....	89
5.1 Motor Testing.....	89
5.1.1 Rotation Rate Test	89
5.1.2 Magnetic Field Motor Test.....	92
5.2. Laboratory Testing	93
5.2.1 Ferromagnetic Testing	94
5.2.1.1 3 Buried Targets	94

5.2.2 Depth Isolation Tests	96
5.2.2.1. Iron Cylinder Depth Test.....	96
5.2.1.2 Pipe Depth Test.....	100
5.2.1.3 Iron Weight Test.....	104
5.2.3 Eddy Currents.....	108
5.2.3.1 Extension Cord	109
5.2.3.1 Extension Cord Unplugged	110
5.2.3.3 Aluminum.....	111
5.2.4 Aluminum Depth Test.....	115
5.2.5 Martian Soil Simulant Testing.....	119
5.2.5.1 Single Martian Simulant	119
5.2.5.2 Two Martian Simulants.....	121
5.2.5.3 Martian Simulant – Air, Water, and Ice Tests.....	123
5.3 Additional Post Processing	126
5.4 Discussion	129
Chapter 6: Conclusions and Future Work	131
6.1 Results.....	131
6.1.1 Ferromagnetic Results	131
6.1.2 Eddy Current Results.....	132
6.1.3 Martian Simulant.....	134
6.1.4 Post Processing.....	134
6.2 Unit.....	134
6.3 Magnetometer.....	135
Works Cited.....	137

Appendix A Steps for Processing Data in Matlab	139
Appendix B Initial Testing	148
Appendix C Additional Results	150

LIST OF FIGURES

Figure	Page
Figure 1: Magnetic Hysteresis Curve Associated with Forced Magnetism [1].....	4
Figure 2: Pathways for the Formation of Ferromagnetic Materials [4].....	5
Figure 3: Depiction of Martian Rover.....	6
Figure 4: DC SQUID Circuit [38]	9
Figure 5: EMI Units [13]	12
Figure 6: Eddy Currents [39]	13
Figure 7: Magnets in Space.....	14
Figure 8: Angle Depiction.....	15
Figure 9: Point in Space.....	18
Figure 10: Point of Interest Geometrical Relationship.....	24
Figure 11: Magnet 1 Geometrical Relationship.....	25
Figure 12: Magnet 2 Geometrical Relationship.....	25
Figure 13: Halbach Array.....	27
Figure 14: Rotation Coordinates.....	28
Figure 15: Vector Plot of Halbach Array.....	32
Figure 16: Polar Alignment of Magnet 1: 0°and Magnet 2: 180°.....	35
Figure 17: Polar Alignment of Magnet 1: 15°and Magnet 2: 195°.....	35
Figure 18: Polar Alignment of Magnet 1: 30° and Magnet 2: 210°.....	35
Figure 19: Polar Alignment of Magnet 1: 45° and Magnet 2: 225°.....	36
Figure 20: Polar Alignment of Magnet 1: 60° and Magnet 2: 240°.....	36
Figure 21: Polar Alignment of Magnet 1: 75° and Magnet 2: 255°.....	36
Figure 22: Polar Alignment of Magnet 1: 90° and Magnet 2: 270°.....	37
Figure 23: Polar Alignment of Magnet 1: 105° and Magnet 2: 285°.....	37
Figure 24: Polar Alignment of Magnet 1: 120° and Magnet 2: 300°.....	37
Figure 25: Polar Alignment of Magnet 1: 135° and Magnet 2: 315°.....	38
Figure 26: Polar Alignment of Magnet 1: 150° and Magnet 2: 330°.....	38
Figure 27: Polar Alignment of Magnet 1: 165° and Magnet 2: 345°.....	38
Figure 28: Magnetic Flux Density Plot with 9-inch Spacing Between Magnets.....	40
Figure 29: Magnetic Flux Density vs. Distance with 3in Magnet Spacing.....	40
Figure 30: FEA of Halbach Array.....	41
Figure 31: Closeup FEA of Halbach Array.....	42
Figure 32: Magnetic Flux Density vs. Distance Plot of Halbach Array.....	42
Figure 33: Iron Bar Geometrical Relationship.....	44
Figure 34: Magnet 1: 0° Magnet 2: 0°.....	45
Figure 35: Magnet 1: 0° Magnet 2: 90°.....	45
Figure 36: Magnet 1: 0°Magnet 2: 180°.....	46
Figure 37: Magnet 1: 0°Magnet 2: 270°.....	46
Figure 38: Magnet 1: 90° Magnet 2: 90°.....	47
Figure 39: Magnet 1: 90° Magnet 2: 180°.....	47

Figure 40: Magnet 1: 90° Magnet 2: 270°	48
Figure 41: Magnet 1: 180° Magnet 2:180°	48
Figure 42: Magnet 1: 180° Magnet 2: 270°	49
Figure 43: Magnet 1: 270° Magnet 2: 270°	49
Figure 44: Halbach Array Flux Density Plots.....	50
Figure 45: Magnetic Field of Two Adjacent Dipoles with Same Polar Orientation [28]..	51
Figure 46: Magnetic Field of Two Adjacent Dipoles with Opposite Polar Orientation...	52
Figure 47: SolidWorks Model of Dual Rotating Unit	54
Figure 48: SolidWorks Model of Spinning Halbach Unit	54
Figure 49: SolidWorks Model of Spinning Halbach Unit with 2 Degrees of Freedom ...	55
Figure 50: SolidWorks Model of Spinning Halbach Unit With 5 Degrees of Freedom...	56
Figure 51: First Iteration.....	57
Figure 52: Second Iteration.....	58
Figure 53: Second Iteration.....	58
Figure 54: Iteration 3	59
Figure 55: Series 3242 Data Sheet [17].....	62
Figure 56: Recommended Operation Area [17].....	63
Figure 57: Main Characteristic Curves [17]	63
Figure 58: Speed vs. Torque [17]	64
Figure 59: Communication Schematic [33].....	66
Figure 60: RM3100 Data Sheet [33].....	67
Figure 61: RM3100 Sensor Schematic [33].....	68
Figure 62: Communication Board Schematic [32]	68
Figure 63: Communication and Evaluation Boards [32].....	69
Figure 64: ASCII Text File	71
Figure 65: RealTerm Serial Capture Program	71
Figure 66: RealTerm Serial Capture Program	72
Figure 67: Data Format.....	72
Figure 68: Motion Controller Schematic [36]	74
Figure 69: Simplified Schematic [36].....	75
Figure 70: 26 Pin D-Sub Connector Wiring Diagram	75
Figure 71: Motor Power Connector Wiring Diagram.....	76
Figure 72: Controller Power Wiring Diagram.....	76
Figure 73: Galil DMC-4123 Controller	77
Figure 74: Initialization Code	78
Figure 75: Gantry Mode Code.....	78
Figure 76: Quadrature Plot [30].....	80
Figure 77: Phase Schematic [30]	81
Figure 78: Representation of 6 Different States [24].....	81
Figure 79: Pulse Width Modulation [24].....	82
Figure 80: IE3-1024 Output Circuit and Signals [29]	83
Figure 81: IE3 Series Encoder Data Sheet [29].....	84
Figure 82: Electronic Gearing Test Close Up.....	85
Figure 83: Labeled Electronic Gearing Test.....	85

Figure 84: Close Up of the Designed Unit.....	86
Figure 85: Unit Attached to Linear Drive in Test Bed	87
Figure 86: All Components of the Final Design.....	87
Figure 87: Size Reference of Unit	88
Figure 88: Speed Equals 4.8 Hz When Galil Set at JG20000.....	90
Figure 89: Speed Equals 12 Hz When Galil Set at JG50000.....	90
Figure 90: Speed Equals 24 Hz When Galil Set at JG100000.....	91
Figure 91: Speed Equals 48 Hz When Galil Set at JG200000.....	91
Figure 92: No Magnets Spinning Motor: X-Axis Data	92
Figure 93: Sandbox Test Bed.....	93
Figure 94: 3 Buried Target Configuration	95
Figure 95: 3 Buried Targets Recorded X-Axis Data	95
Figure 96: Iron Cylinder Location	97
Figure 97: 2.5-Inch - Iron Cylinder Recorded X-Axis Data.....	97
Figure 98: 4-Inch - Iron Cylinder Recorded X-Axis Data.....	98
Figure 99: 5.5-Inch - Iron Cylinder Recorded X-Axis Data.....	99
Figure 100: 7-Inch - Iron Cylinder Recorded X-Axis Data.....	100
Figure 101: Steel Pipe Locations	101
Figure 102: 2.5-Inch - Steel Pipe Recorded X-Axis Data	101
Figure 103: 4-Inch - Steel Pipe Recorded X-Axis Data	102
Figure 104: 5.5-Inch - Steel Pipe Recorded X-Axis Data	103
Figure 105: 7-Inch - Steel Pipe Recorded X-Axis Data	104
Figure 106: Weight Location.....	105
Figure 107: 2.5-Inch - Iron Weight Recorded X-Axis Data	105
Figure 108: 4-Inch - Iron Weight Recorded X-Axis Data	106
Figure 109: 5.5-Inch - Iron Weight Recorded Z-Axis Data	107
Figure 110: 7-Inch - Iron Weight Recorded Z-Axis Data	108
Figure 111: Extension Cord Location.....	109
Figure 112: Plugged in Extension Cord X-Axis Data	110
Figure 113: Extension Cord Recorded X-Axis Data	111
Figure 114: Aluminum Cylinder Location	112
Figure 115: Speed 24 Hz: Aluminum Recorded X-Axis Data	112
Figure 116: Speed 4.8 Hz: Aluminum Recorded X-Axis Data	113
Figure 117: Speed 0 Hz: Aluminum Recorded X-Axis Data	114
Figure 118: 2.5-Inch - Aluminum Recorded X-Axis Data	115
Figure 119: 4-Inch - Aluminum Recorded X-Axis Data	116
Figure 120: 5.5-Inch - Aluminum Recorded X-Axis Data	117
Figure 121: 7-Inch - Aluminum Recorded X-Axis Data	118
Figure 122: Single Martian Simulant Test Setup.....	119
Figure 123: Martian Simulant GPR Data with Simulant.....	120
Figure 124: GPR Data without Simulant.....	120
Figure 125: Martian Simulant - Magnet X-Axis Data.....	121
Figure 126: Two Martian Simulants Test Setup.....	122
Figure 127: 2 Buried Martian Simulants X-Axis Data	122

Figure 128: Air, Water, and Ice Tests Setup.....	124
Figure 129: Martian Simulant with Air Pocket: X-Axis Data	124
Figure 130: Martian Simulant with Water Pocket: X-Axis Data.....	125
Figure 131: Martian Simulant with Ice Pocket: X-Axis Data.....	125
Figure 132: Original 3 Buried Objects X-Axis Data	127
Figure 133: 3 Buried Objects Test X-Axis Data with Motor Field Removed	127
Figure 134: 3 Buried Objects Test X-Axis Data with Background Field Removed	128
Figure 135: 3 Buried Objects Test: Z Axis Data	131
Figure 136: Aluminum X Axis Data.....	133
Figure 137: Initial 3 Buried Object Test.....	148
Figure 138: Initial Martian Soil Test	149
Figure 139: 3 Buried Targets Recorded Y Axis Data	150
Figure 140: 3 Buried Targets Recorded Z Axis Data	150
Figure 141: Iron Cylinder Recorded X Axis Data	151
Figure 142: Iron Cylinder Recorded Y Axis Data	151
Figure 143: Iron Cylinder Recorded X Axis Data	152
Figure 144: Iron Cylinder Recorded Y Axis Data	152
Figure 145: Iron Cylinder Recorded X Axis Data	153
Figure 146: Iron Cylinder Recorded Y Axis Data	153
Figure 147: Steel Pipe Recorded X Axis Data.....	154
Figure 148: Steel Pipe Recorded Y Axis Data.....	154
Figure 149: Steel Pipe Recorded X Axis Data.....	155
Figure 150: Steel Pipe Recorded Y Axis Data.....	155
Figure 151: Steel Pipe Recorded X Axis Data.....	156
Figure 152: Steel Pipe Recorded Y Axis Data.....	156
Figure 153: Iron Weight Recorded X Axis Data	157
Figure 154: Iron Weight Recorded Y Axis Data	157
Figure 155: Iron Weight Recorded X Axis Data	158
Figure 156: Iron Weight Recorded Y Axis Data	158
Figure 157: Iron Weight Recorded X Axis Data	159
Figure 158: Iron Weight Recorded Y Axis Data	159
Figure 159: Extension Cord Recorded Y Axis Data.....	160
Figure 160: Extension Cord Recorded Z Axis Data	160
Figure 161: Extension Cord Recorded Y Axis Data.....	161
Figure 162: Extension Cord Recorded Z Axis Data	161
Figure 163: Aluminum Recorded Y Axis Data	162
Figure 164: Aluminum Recorded Z Axis Data.....	162
Figure 165: Aluminum Recorded Y Axis Data	163
Figure 166: Aluminum Recorded Z Axis Data.....	163
Figure 167: Aluminum Recorded Y Axis Data	164
Figure 168: Aluminum Recorded Z Axis Data.....	164
Figure 169: Aluminum Recorded Y Axis Data	165
Figure 170: Aluminum Recorded Z Axis Data.....	165
Figure 171: Aluminum Recorded Y Axis Data	166

Figure 172: Aluminum Recorded Z Axis Data.....	166
Figure 173: Aluminum Recorded Y Axis Data.....	167
Figure 174: Aluminum Recorded Z Axis Data.....	167
Figure 175: Martian Simulant Y Axis Test 1.....	168
Figure 176: Martian Simulant Z Axis Test 1.....	168
Figure 177: Martian Simulant Y Axis Test 2.....	169
Figure 178: Martian Simulant Z Axis Test 2.....	169
Figure 179: SolidWorks Model of Magnet Holder.....	170
Figure 180: SolidWorks Model of Magnet Holder.....	170
Figure 181: Dimensioned Schematic of Magnet Holder.....	171

CHAPTER 1: Introduction

The main goal of this research is to develop a magnetic sensing device that locates both terrestrial and extraterrestrial subsurface anomalies. The design uses an array of moving permanent magnets creating a shaped oscillating magnetic field that interacts with subsurface features to produce an effect that is measurable with a magnetometer. By spinning a synchronized array of magnets, the induced magnetic field will magnify the magnetic signature of subsurface objects of interest. Even non-magnetic materials can be detected by inducing eddy currents when rotating the magnets at higher speeds. The design has the potential to sense through iron-based soils to find underground infrastructure and unexploded ordinances on Earth and changes in soil densities and water/ice pockets on Mars.

The objectives of the project are to: (1) develop a low cost, lightweight, subsurface sensing unit that utilizes an array of neodymium magnets, and (2) test the sensitivity and viability of a dual rotating magnet unit for both terrestrial and extraterrestrial applications. The objectives are explored through 6 chapters. Chapters 2 and 3 use mathematical models and finite element analysis to quantify how a given array of magnets and their individual fields will interact. Chapter 4 explains the four different iterations of the design and why the components of each design were chosen. Chapter 5 explains the testing results and Chapter 6 looks at conclusions and future work.

1.1 Literature Review

The following literature review covers four major topics: (1) the composition of the Martian surface and subsurface, (2) geophysical sensing equipment presently on Mars

rovers including GPR systems, (3) need for on Earth magnetic sensing devices, and (4) present state of the art magnetometer sensing devices. The motivation resides in the importance to understand the soil composition on Mars to prove the possible successful uses of the dual rotating magnet sensing device. Additionally, knowledge of the present state of the art of magnetic sensing systems is critical to designing and testing an improved and useful magnetometer sensing system. Current magnetic sensing devices use magnetometers and large coils to identify and/or locate subterranean objects. This review of current magnetic devices summarizes the advantages and disadvantages of existing systems, including cost and weight. The research goal is to develop a new magnetometer sensing system that actively induces magnetic fields to sense what lies beneath the surface.

1.1.1 Martian Soil

Space exploration is an ever-growing field. NASA and other agencies are constantly seeking to improve current technologies to further their extraterrestrial knowledge. Mobile wheeled rovers are currently being used to study Mars. Little is known about the Martian soil. Many areas are of interest such as identifying and characterizing soft pockets of sand that cause the rovers to lose traction and pockets of water and ice. Finding ice and water pockets can be very helpful in determining the past and future possibilities of life on Mars [4]. Current Mars rovers are each outfitted with magnetic property tools with the following objectives in mind: “(i) to identify the magnetic minerals in the dust, soil and rocks on Mars, (ii) establish if the material is present in the form of nanosized ($d < 10\text{nm}$) superpara-magnetic crystallites, and (iii) to establish if the magnets are culling a subset of strongly magnetic particles” [4]. The particles collected by the

magnets are then studied using different spectrometers located on an instrument deployment device(IDD) [4]. From numerous tests it is confirmed that Martian soil is composed of iron sulfate, making it a magnetic surface [4].

The composition of Martian soil is critical to the viability of magnetic sensing on Mars. Martian soil contains 13% by weight the element iron [4]. Little is known about the mineralogical composition of the Martian regolith, but by visual spectroscopy the majority of iron is in the oxidation state Fe(III) [4].

The Opportunity rover was outfitted with a miniaturized Mossbauer spectrometer called the MIMOS II that measured the Mossbauer spectra [6]. This provides quantitative information about the distribution of iron in its multiple oxidation states. The Mimos II is mounted on a robotic arm that can rotate back and forth to position the spectrometer over the target [6]. The Mossbauer tests on the Meridian Planum at Eagle crater revealed four mineralogical components: jarosite and hematite rich outcrop, hematite rich soil, olivine bearing basaltic soil and a pyroxene bearing basaltic rock [6]. Jarosite is a hydrous sulfate potassium iron sulfate that is formed by oxidation of iron sulfides, the formation process occurs in ore deposits [7]. Hematite is a mineral form of iron oxide (III)[8], while olivine and pyroxene bearing basaltic soil are created from volcanic lava [6]. Due to the magnetic properties of the Martian regolith, finding abnormalities on the Martian surface may be possible with an active magnetic sensing system, such as a dual rotating magnet with a magnetometer sensor system.

Iron exhibits a magnetic behavior called ferromagnetism. Ferromagnetic materials contain magnetic dipoles that are orientated parallel to each other, even without an external

field. Unlike other materials, ferromagnetic substances can be magnetized easily up to the saturation limit. At saturation the magnetic field can no longer be increased. Iron tends to stay magnetized after being subjected to an external magnetic field through a process called hysteresis [5]. The theoretical model of magnetization is seen in the Figure 1. The initial magnetization curve starts at the origin and moves upward. The upper and lower curves model the main loop that occurs after saturation. Where h_c and m_{rs} are the coercivity ability of material, (to withstand demagnetization when exposed to an external magnetic field) and saturation remanence (magnetization remaining in zero field), respectively [2].

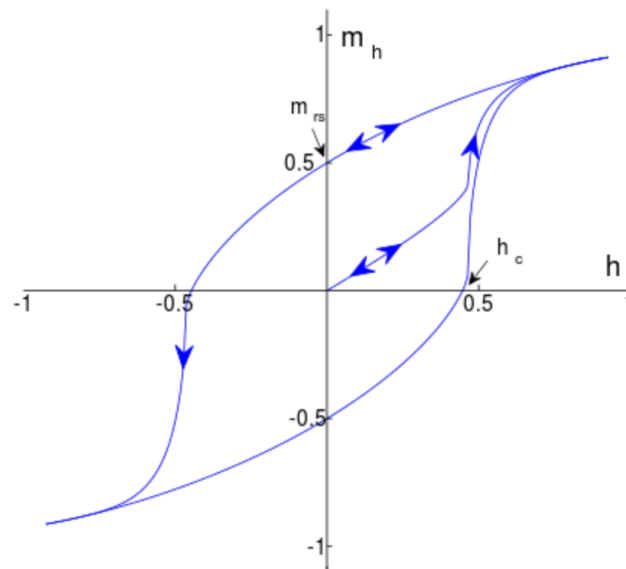


Figure 1: Magnetic Hysteresis Curve Associated with Forced Magnetism [1]

The formation of the iron sulfate rich soil on Mars is largely due to reaction with liquid water [4]. Iron sulfate forms by exposing iron to moisture for an extended period of time [18]. Figure 2 summarizes the pathways to the formation of ferromagnetic minerals on Mars.

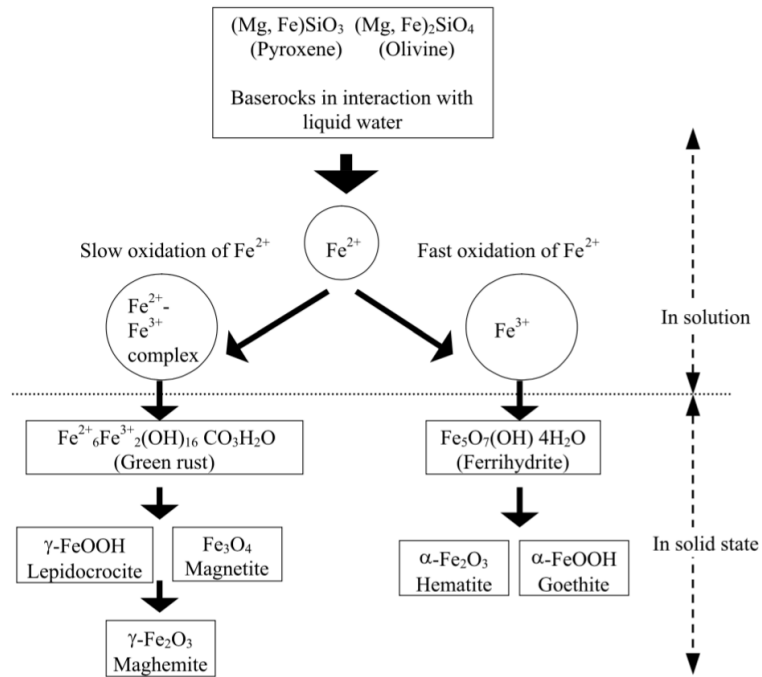


Figure 2: Pathways for the Formation of Ferromagnetic Materials [4]

The formation process of iron sulfate makes it likely that the soil surrounding a water pocket on Mars will most likely have a higher concentration of iron sulfate due to heightened moisture levels. This phenomenon indicates that a magnetic sensing unit will be useful for locating subsurface water pockets.

1.1.2 Martian Rovers

There are currently three rovers on Mars: The Spirit, Opportunity and Curiosity. The Opportunity and Curiosity are active, and the Spirit is unresponsive [2]. Both active rovers are outfitted with state of the art equipment that record Martian information. The Opportunity has seven different tools: cameras, rock abrasion tool (RAT), microscopic imager, alpha-particle x-ray spectrometer, Mossbauer spectrometer, mini-thermal emission spectrometer and magnet arrays [10]. The objective for each rover is similar: to search for

and characterize a wide range of rocks and soils that hold clues to past water activity on Mars [10].

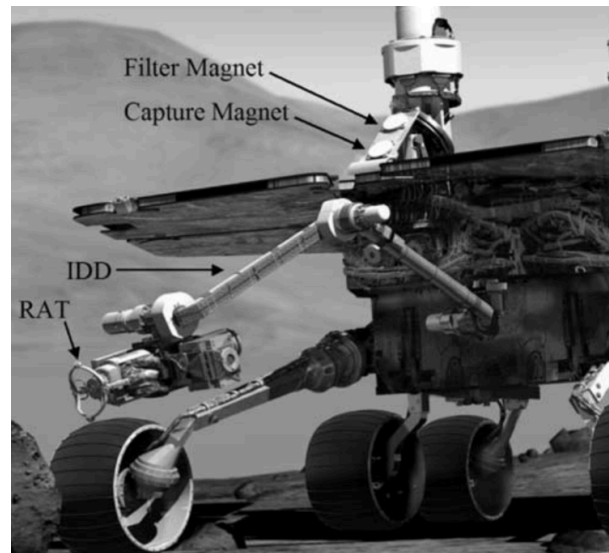


Figure 3: Depiction of Martian Rover

NASA plans to launch a rover in July or August of 2020 that is similar to the Opportunity. NASA has four scientific goals for the 2020 mission: (1) determine whether life ever arose on Mars, (2) characterize the climate of Mars, (3) characterize the geology of Mars, and (4) prepare for human exploration [9]. Four objectives support these scientific goals: (1) identify past environments capable of supporting microbial life, (2) seek signs of possible past microbial life in those habitable environments, particularly in special rocks known to preserve signs of life over time, (3) collect core rock and “soil” samples and store them on the Martian surface, and (4) test oxygen production from the Martian atmosphere in preparation for humans [9]. The 2020 rover will have similar equipment as the Opportunity, with the addition of a drill for coring rocks and soil. Collected cores will be

stored in a tube on the Martian surface in hope for future missions to collect the stored samples and return them to Earth for further analysis [9].

A radar imager for Mars' subsurface experiments (RIMFAX) is another technology that may get added to the 2020 rover. Developed by Norwegian Svein-Erik Hamran, the RIMFAX's primary purpose is to locate geological features under the surface with ground penetrating radar (GPR) [9]. The GPR unit operates at a frequency range of 150 to 1200 megahertz and depending on the soil material penetration depths greater than 30 feet can be reached [9]. Due to the iron rich surface on Mars, these depths are ambitious. High content iron sulfate soil will change the dielectric properties of the soil and change how well the GPR signal can be sent and received [11]. Depending on the amount of iron in the soil it will attenuate the electromagnetic signal, clouding and distorting the sensing of subsurface structures on Mars [11]. A magnetic sensing unit may be more appropriate for Martian applications.

1.1.3 Magnetometers

Magnetometers appear in numerous sensing applications, such as locating subterranean objects. A magnetometer can measure and record a magnetic field, and therefore can be used to conduct geophysical surveys to detect magnetic anomalies [14]. Vector magnetometers measure the flux density in a specific direction within a three-dimensional space and scalar magnetometers measure the magnitude of the vector field

[12]. Different types of vector magnetometers include Hall effect, flux gate, SQUID, and atomic [12].

Hall effect sensors are the most commonly used. They work by producing a voltage that is proportional to the applied magnetic field. The sensor consists of a semiconductor crystal made of an indium compound that is mounted on an aluminum plate [38]. When the sensor is exposed to a magnetic field, a current passes through the crystal and a voltage is formed across it. This phenomenon is known as the Hall effect voltage [38]. Hall sensors are also able to sense the polarity of the field and work best in applications with large magnetic field strength [38]. Flux gate magnetometers consist of a small core that is wrapped in two coils of wire. The core is composed of magnetically susceptible material and as an alternating electrical current is passed through the core it is driven through an alternating cycle of magnetic saturation [12]. The changing field induces an electric current in the second coil and the output current is measured through the detector. When a background field is present, the core is more easily saturated when the alternating field is in alignment with the background field and not as easily saturated when the fields are opposite [38]. The strength and phase of the signal depends directly on the external magnetic field's magnitude and polarity. Superconducting quantum interface devices (SQUID) are able to measure very small changes in a magnetic field. There are either RF or DC SQUIDs.

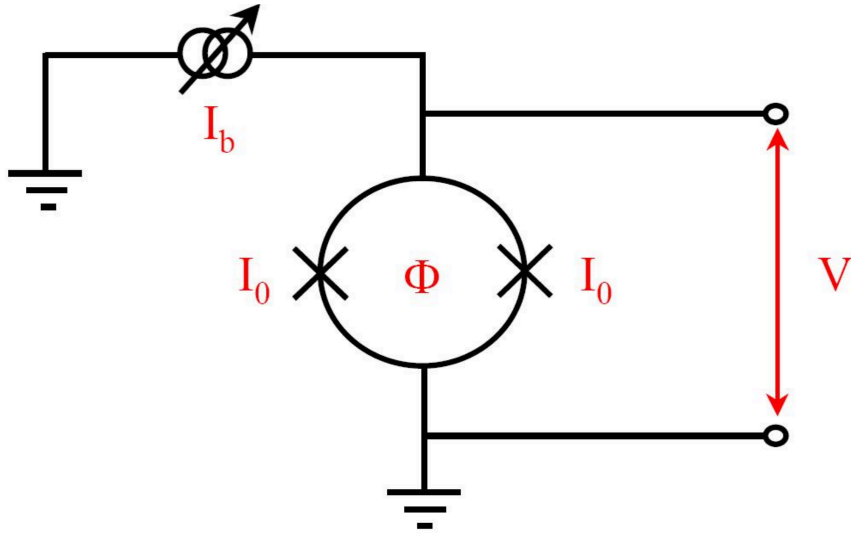


Figure 4: DC SQUID Circuit [38]

DC SQUIDS work by an input current that splits at a junction into two branches equally, as seen in Figure 4. When an external magnetic field is applied, the current begins circling in the loop and when the current exceeds the critical current, a voltage is formed across the junction [38]. The most common superconducting materials used are niobium, lead alloy with 10 percent gold, or indium. The high sensitivity is due to low noise levels [38]. In order to maintain super conductivity, the device needs to be liquid cooled using helium or nitrogen which makes their use difficult in most applications. Due to the cooling requirements SQUIDS are used mostly in laboratory and biology applications [12]. The last type of vector magnetometer is a spin-exchange relaxation free (SERF) atomic magnetometer. They use lasers to detect the interaction between alkali metals and a magnetic field. SERF magnetometers contain potassium, cesium or rubidium vapor and have a sensitivity of $1 \text{ fT Hz}^{-1/2}$ [38]. A SERF magnetometer is highly sensitive because it measures the dense alkali metal vapor that is in a near zero magnetic field [38]. The

SERF magnetometer is different from other atomic magnetometers because it eliminates the atomic spin decoherence that occurs in spin exchange collisions [12]. Spin exchange collisions between atoms do not change the angular momentum of either atom, but the hyperfine state of the atoms does change [12]. The sensitivity is determined by the number of atoms in the circuit and their spin coherence. Due to the sensitivity of the unit, these magnetometers can only operate in low magnetic fields that are less than $0.5 \mu T$ [38]. The technology, when used in large volumes, can achieve greater sensitivity per unit volume than the SQUID magnetometers.

The performance of any magnetometer is dependent on the bandwidth, resolution, thermal stability, noise, and sampling rate [12]. Bandwidth determines if a magnetometer can track rapid changes, and the smallest magnetic field change the magnetometer can accurately record determines the resolution [38]. Measurements are dependent on the temperature due to thermal stability [12]. Noise is a major function of the performance of the unit, it is generated by the sensor or electronics [12]. The sensitivity of a magnetometer is the larger value of the noise or resolution and the sampling rate corresponds to the number of readings per second, which is the inverse of the cycle time [12].

1.1.4 Electromagnetic Induction

Lenz's law states that "induced electric current flows in a direction such that the current opposes the change that induced it" [15]. Depending on the sensitivity of the magnetometer, a variety of underground objects can be located. In order to increase sensitivity, electromagnetic induction units were introduced. Electromagnetic induction (EMI) sensing units, also known as search coil magnetometers, were introduced in the late

1970's to increase subterranean detection abilities [13]. EMI units consist of a large coil of tightly wound wire and a magnetometer. Electromagnetic induction is created by an induced electromotive force in a circuit by a varying magnetic flux, which is explained by Faraday's law [13]. Faraday's law of induction states how an electromotive force is produced when a magnetic field interacts with an electric current [16]. Faraday used the following equation to relate the rate of change of a magnetic field flux to the induced voltage [23].

$$e = N \frac{d\phi}{dt}$$

Where e=instantaneous voltage, N=number of turns in wire coil, Φ =magnetic flux and t=time.

Initially EMI was used to test soil salinity and now has expanded into soil detection, compaction, organic matter content, and pH content [12]. Additionally, EMI is used for underground location of UXOs (unexploded ordinance) and other objects of interest. Electromagnetic induction sensors transmit a primary electromagnetic field that induces an electrical current into the soil. A secondary field is created by the currents in the soil and then recorded by a magnetometer [12]. An area where an object of interest such as an UXO is located will transmit a different electrical current than the rest of the surrounding soil. These units are effective but have inherent disadvantages.

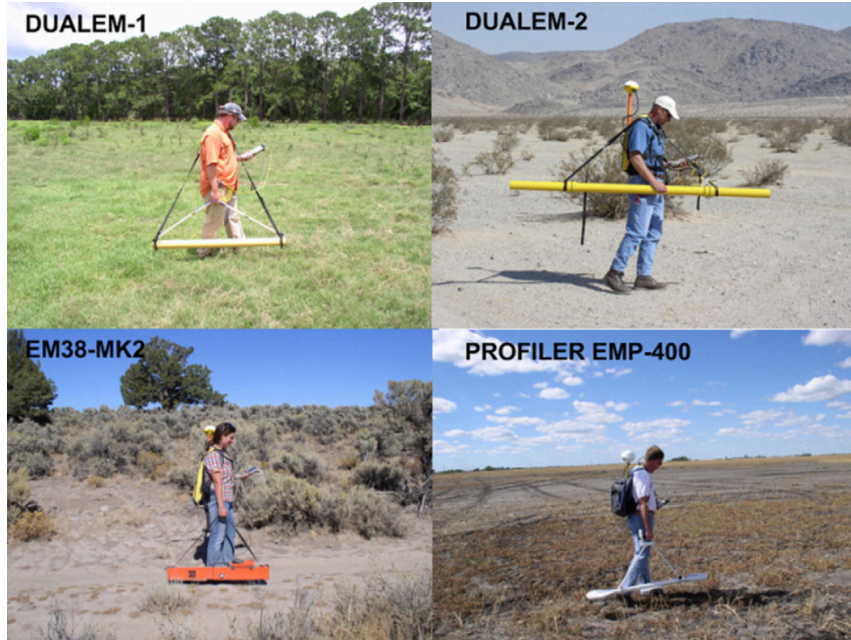


Figure 5: EMI Units [13]

EMI units are large and bulky as seen in Figure 4, making it difficult to use in tight spaces. An average EMI unit weighs 73.9 pounds with an overall length of 49.9 inches [3]. For weight and size sensitive applications, such as on a Mars rover, these EMI systems are oversized.

1.1.5 Eddy Currents

Eddy currents (see Figure 6), are loops of electrical currents that are created by a changing magnetic field in the conductor [21]. A magnetometer with suitable sensitivity and frequency range can detect eddy currents.

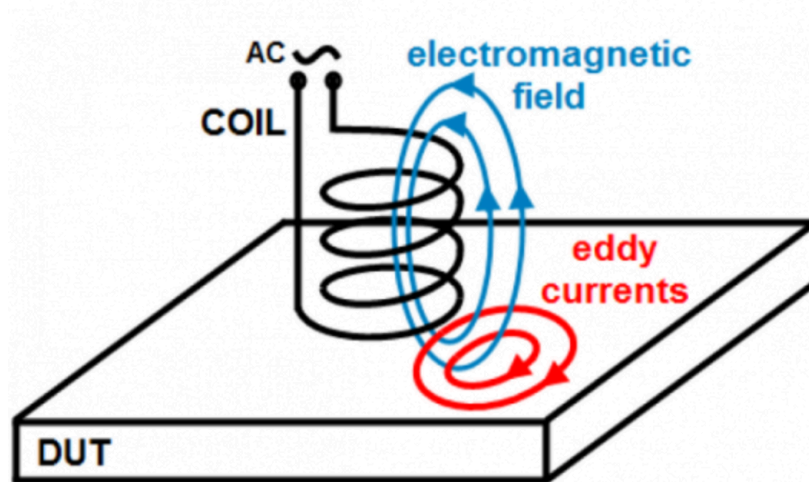


Figure 6: Eddy Currents [39]

A magnetometer with capabilities of sampling at a rate of over 50 Hz will detect eddy currents within an object [22]. By spinning two magnets with opposing fields at a high rotation rate, detection of nonferrous materials such as aluminum and copper is possible. Spinning the magnets at 6,000 rpm or higher will induce eddy currents in materials that are otherwise undetectable by a magnetometer [22]. Being able to induce and detect eddy currents is crucial for the viability of a magnetic sensing unit to find and map underground infrastructure, as many features of interest often contain ferromagnetic and non-ferromagnetic metallic conductors.

CHAPTER 2: Quasi-Static Multi-Dipole Model of Rotating Magnet Arrays

Due to the complexity of the magnetic field for a given array of magnets (i.e. Halbach array), a theory was derived to better understand the interaction.

2.1 Multiple Dipole Local to Global Coordinate Theory

To understand the magnetic field produced by the dual rotating magnet unit, the magnetic field produced by a set of dipole magnets must be calculated in three dimensions. Using a mathematical model for a multi-dipole magnetic field, the magnetic field can be calculated in any arbitrary position and orientation in 3-D space [37]. It is assumed that the magnets act as dipoles and can rotate individually about a fixed axis, but the rotation speed is slow enough for static field calculations. An additional assumption is that the magnetic fields form in a non-magnetic medium, such as a vacuum or air, that acts linearly. For example, individual magnets each produce a field that superpose and add at points in space.

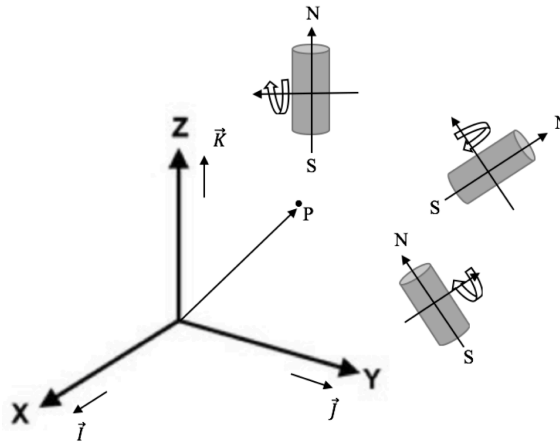


Figure 7: Magnets in Space

For a given point in space \vec{P} , the magnetic field \vec{B}_P is the sum of the fields from each individual magnet.

$$\vec{B}_P = \vec{B}_{P1} + \vec{B}_{P2} + \dots + \vec{B}_{PN} \quad (1)$$

Where \vec{B}_{PN} is the individual magnetic field. To calculate the individual magnetic field of a single magnet the field is first considered in local coordinates.

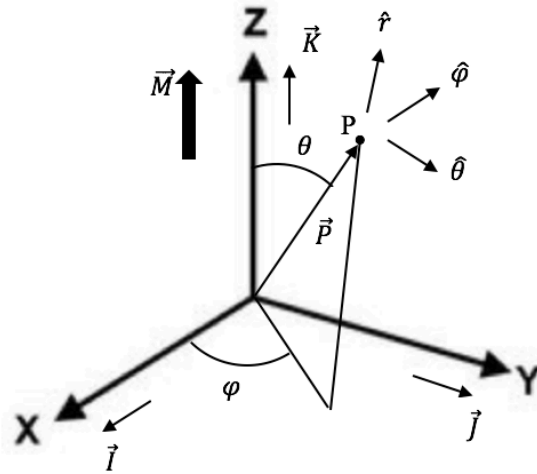


Figure 8: Angle Depiction

As seen in Figure 8, assume the magnetic dipole (M) points North in the positive Z direction so the magnetic dipole vector has the following characteristics.

$$\vec{M} = |\vec{M}|\vec{k} = M\vec{k} \quad (2)$$

\vec{r} = Position vector of P in local coordinates

\vec{i}, \vec{j} and \vec{k} = Unit vectors for cartesian coordinate system

$\hat{\theta}, \hat{\phi}$ and \hat{r} = Unit vectors for spherical coordinate system

Using the equation for a static magnetic field potential in spherical coordinates.

$$\vec{B}(\vec{r}) = \nabla \times \vec{A} \quad (3)$$

Where \vec{A} is the potential field for a magnetic dipole:

$$\vec{A} = \frac{\mu_0 \vec{m} \times \vec{r}}{4\pi r^3} \quad (4)$$

Inserting \vec{A} into $\vec{B}(\vec{r})$:

$$\vec{B}(\vec{r}) = \nabla \times \left[\frac{\mu_0 \vec{m} \times \vec{r}}{4\pi r^3} \right] \quad (5)$$

For this specific case:

$$\vec{m} \times \vec{r} = \frac{\mu_0 |\vec{m}| |\vec{r}|}{4\pi r^3} \sin \theta \hat{\phi} = \frac{\mu_0 m}{4\pi r^3} \sin \theta \hat{\phi} \quad (6)$$

The following steps are taken to solve for the magnetic field of one dipole.

$$\begin{aligned} \vec{B}(\vec{r}) = \nabla \times \vec{A} &= \frac{1}{r \sin \theta} \left[\frac{\partial}{\partial \theta} (A_\theta \sin \theta) - \frac{\partial A_\phi}{\partial \varphi} \right] \hat{r} + \\ &\frac{1}{r} \left[\frac{1}{\sin \theta} \frac{\partial A_r}{\partial \varphi} - \frac{\partial}{\partial r} (r A_\phi) \right] \hat{\theta} + \frac{1}{r} \left[\frac{\partial}{\partial r} (r A_\theta) - \frac{\partial A_r}{\partial \theta} \right] \hat{\phi} \end{aligned} \quad (7)$$

Where $A_\theta = A_r = 0$. And therefore, simplifying to:

$$\vec{B}(\vec{r}) = \nabla \times \vec{A} = \frac{1}{r \sin \theta} \left[\frac{\partial}{\partial \theta} (A_\phi \sin \theta) \right] \hat{r} + \frac{1}{r} \left[-\frac{\partial}{\partial r} (r A_\phi) \right] \hat{\theta} \quad (8)$$

Continuing to solve for \vec{B} .

$$A_\phi = \frac{\mu_0 m \sin \theta}{4\pi r^2} \quad (9)$$

Let $C = \frac{\mu_0 m}{4\pi}$, and first solve for $\frac{\partial}{\partial \theta} (A_\phi \sin \theta)$

$$\frac{\partial}{\partial \theta} (A_\phi \sin \theta) = \frac{\partial}{\partial \theta} \left[C \frac{\sin \theta}{r^2} \sin \theta \right] \quad (10)$$

$$\frac{\partial}{\partial \theta} (A_\varphi \sin \theta) = \frac{\partial}{\partial \theta} \left[\frac{C}{r^2} \sin^2 \theta \right] \quad (11)$$

$$\frac{\partial}{\partial \theta} (A_\varphi \sin \theta) = \frac{C}{r^2} 2 \sin \theta \cos \theta \quad (12)$$

Next solving for rA_φ .

$$\frac{\partial}{\partial \theta} (rA_\varphi) = \frac{\partial}{\partial r} \left(rC \frac{\sin \theta}{r^2} \right) \quad (13)$$

$$\frac{\partial}{\partial \theta} (rA_\varphi) = \frac{\partial}{\partial r} \left(C \frac{\sin \theta}{r} \right) \quad (14)$$

$$\frac{\partial}{\partial \theta} (rA_\varphi) = -C \frac{\sin \theta}{r^2} \quad (15)$$

Inserting $\frac{\partial}{\partial \theta} (A_\varphi \sin \theta)$ and $\frac{\partial}{\partial r} (rA_\varphi)$ into Equation 3.

$$\vec{B}(\vec{r}) = \nabla \times \vec{A} = \frac{1}{r \sin \theta} \left[\frac{C}{r^2} 2 \sin \theta \cos \theta \right] \hat{r} + \frac{1}{r} \left[C \frac{\sin \theta}{r^2} \right] \hat{\theta} \quad (16)$$

Simplifying to:

$$\vec{B} = \nabla \times \vec{A} = \frac{C}{r^3} 2 \cos \theta \hat{r} + C \frac{\sin \theta}{r^3} \hat{\theta} = \frac{C}{r^3} [2 \cos \theta \hat{r} + \sin \theta \hat{\theta}] \quad (17)$$

Convert the magnetic field from local spherical to local Cartesian coordinates.

Knowing \hat{r} and $\hat{\theta}$.

$$\hat{r} = \sin \theta \cos \varphi \vec{i} + \sin \theta \sin \varphi \vec{j} + \cos \theta \vec{k} \quad (18)$$

$$\hat{\theta} = \cos \theta \cos \varphi \vec{i} + \sin \theta \sin \varphi \vec{j} - \sin \theta \vec{k} \quad (19)$$

Then \vec{B} becomes:

$$\vec{B} = \frac{C}{r^3} \left[\begin{array}{l} 2 \cos \theta [\sin \theta \cos \varphi \vec{i} + \sin \theta \sin \varphi \vec{j} + \cos \theta \vec{k}] + \\ \sin \theta [\sin \theta \cos \varphi \vec{i} + \sin \theta \sin \varphi \vec{j} - \sin \theta \vec{k}] \end{array} \right] \quad (20)$$

$$\vec{B} = \frac{C}{r^3} \left[(2 \cos \theta \sin \theta \cos \varphi + \sin \theta \cos \varphi \cos \theta) \vec{i} + 2 \cos \theta \sin \theta \sin \varphi \vec{j} + (2 \cos \theta \cos \theta - \sin \theta \sin \theta) \vec{k} \right] \quad (21)$$

$$\vec{B} = \frac{C}{r^3} [3 \cos \theta \sin \theta \cos \varphi \vec{i} + 3 \cos \theta \sin \theta \sin \varphi \vec{j} + (2 \cos^2 \theta - \sin^2 \theta) \vec{k}] \quad (22)$$

Now the total local magnetic field is equal to $\vec{B} = B_x^L \vec{i} + B_y^L \vec{j} + B_k^L \vec{k}$.

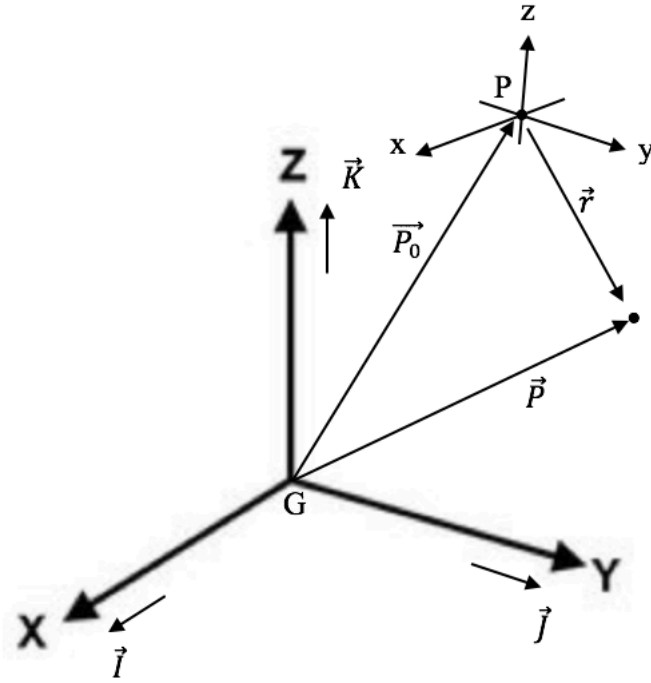


Figure 9: Point in Space

Where \vec{P} = Position of point P in global coordinates, \vec{r} = Position of point P in local coordinates, and \vec{P}_0 = Position of origin of local coordinate system relative to origin of global coordinates.

And:

$$\vec{P} = \vec{P}_0 + \vec{r} \quad (23)$$

Therefore:

$$\vec{r} = \vec{P} - \vec{P}_0 \quad \text{or} \quad \vec{r}^G = \vec{P}^G - \vec{P}_0^G \quad (24)$$

Multiplication with a dyadic of direction cosines converts the components of \vec{r}^G into \vec{r}^L with:

$$\{r^L\} = [R]\{r^G\} \quad (25)$$

$$\begin{bmatrix} r_x^L \\ r_y^L \\ r_z^L \end{bmatrix} = [R] \begin{bmatrix} r_x^G \\ r_y^G \\ r_z^G \end{bmatrix} \quad (26)$$

$$\begin{bmatrix} r_x^L \\ r_y^L \\ r_z^L \end{bmatrix} = \begin{bmatrix} R_{11} & R_{12} & R_{13} \\ R_{21} & R_{22} & R_{23} \\ R_{31} & R_{32} & R_{33} \end{bmatrix} \begin{bmatrix} r_x^G \\ r_y^G \\ r_z^G \end{bmatrix} \quad (27)$$

To enable calculating the \vec{B} in Cartesian coordinate system the following steps must be taken.

$$B_x = \frac{C}{r^3} 3 \cos \theta \sin \theta \cos \varphi \quad (28)$$

$$B_y = \frac{C}{r^3} 3 \cos \theta \sin \theta \sin \varphi \quad (29)$$

$$B_z = \frac{C}{r^3} (2 \cos^2 \theta - \sin^2 \theta) \quad (30)$$

$$r^2 = \vec{r}^L \cdot \vec{r}^L = \vec{r}^G \cdot \vec{r}^G \quad (31)$$

$$r = \left\{ r_x^{G^2} + r_y^{G^2} + r_z^{G^2} \right\}^{\frac{1}{2}} = \left\{ r_x^{L^2} + r_y^{L^2} + r_z^{L^2} \right\}^{\frac{1}{2}} \quad (32)$$

Where:

$$\sin \theta = \frac{1}{r} (r_x^{L^2} + r_y^{L^2})^{\frac{1}{2}} \quad (33)$$

$$\cos \theta = \frac{1}{r} r_3^2 \quad (34)$$

$$\sin \varphi = \frac{r_y^L}{(r_x^{L2} + r_y^{L2})^{\frac{1}{2}}} \quad (35)$$

$$\cos \varphi = \frac{r_x^L}{(r_x^{L2} + r_y^{L2})^{\frac{1}{2}}} \quad (36)$$

Knowing Equations 33 through 36 \vec{B}_{total}^L in local Cartesian coordinates can now be calculated.

$$\vec{B}^L = B_x^L \vec{i} + B_y^L \vec{j} + B_z^L \vec{k} \quad (37)$$

To calculate the total magnetic field for an array of magnets, one first must calculate the magnetic field for each dipole in global coordinates, using the inverse (transpose) of the orthogonal rotation matrix.

$$\{B^G\} = [R]^T \{B^L\} \quad (38)$$

$$\begin{bmatrix} B_x^G \\ B_y^G \\ B_z^G \end{bmatrix} = [R]^T \begin{bmatrix} B_x^L \\ B_y^L \\ B_z^L \end{bmatrix} \quad (39)$$

$$\begin{bmatrix} B_x^G \\ B_y^G \\ B_z^G \end{bmatrix} = \begin{bmatrix} R_{11} & R_{12} & R_{13} \\ R_{21} & R_{22} & R_{23} \\ R_{31} & R_{32} & R_{33} \end{bmatrix}^T \begin{bmatrix} B_x^L \\ B_y^L \\ B_z^L \end{bmatrix} \quad (40)$$

Or:

$$\begin{bmatrix} B_x^G \\ B_y^G \\ B_z^G \end{bmatrix} = \begin{bmatrix} R_{11} & R_{21} & R_{31} \\ R_{12} & R_{22} & R_{32} \\ R_{13} & R_{23} & R_{33} \end{bmatrix} \begin{bmatrix} B_x^L \\ B_y^L \\ B_z^L \end{bmatrix} \quad (41)$$

$$\vec{B}^G = B_x^G \vec{i} + B_y^G \vec{j} + B_z^G \vec{k} \quad (42)$$

Once each dipole is solved in global coordinates the total magnetic field for an array of magnets can be calculated.

$$\vec{B}^G_{total}(x, y, z) = B_1^G + B_2^G + \dots B_N^G \quad (43)$$

Where B_N^G is the magnetic field for nth magnet in global coordinates.

In order to solve for \vec{B}^G_{total} the rotation matrix $[R]$ must be solved. By solving for the global magnetic field, the magnets can be modeled in rotation, the coordinate system must therefore be transformed from local to global coordinates. By choosing an arbitrary global coordinate system, all magnets in an array will have different R vectors to a given point in space. The sequence of rotations is first about the z-axis to get x' , y' , and z' . The second rotation is about y' to get x'' , y'' , and z'' so that x'' aligns with the spin axis of the magnets and then rotates about x'' to spin the magnets. The angles θ , φ , and ψ determine where in space a R vector is pointing in 3-dimensional space. By using global coordinates, the total magnetic field for a given array in 3-D can be calculated at any point as the magnets rotate.

The rotation in Figure 8 depicts the three angles θ , φ , and ψ . Each rotation angle has its own corresponding rotation matrix.

Rotation 1 (R_1) is the rotation φ about the z-axis in the $x - y$ plane.

$$R_1 = \begin{bmatrix} \cos\varphi & \sin\varphi & 0 \\ -\sin\varphi & \cos\varphi & 0 \\ 0 & 0 & 1 \end{bmatrix} \quad (44)$$

Rotation 2 (R_2) is the rotation θ about the y' -axis in the $y' - z'$ plane.

$$R_2 = \begin{bmatrix} 1 & 0 & 0 \\ 0 & \cos\theta & \sin\theta \\ 0 & -\sin\theta & \cos\theta \end{bmatrix} \quad (45)$$

Rotation 3 (R_3) is the rotation ψ about the x'' - axis in the $x' - y'$ plane.

$$R_3 = \begin{bmatrix} \cos\psi & \sin\psi & 0 \\ -\sin\psi & \cos\psi & 0 \\ 0 & 0 & 1 \end{bmatrix} \quad (46)$$

The total rotation matrix can be solved using:

$$R_{total} = R_1 \times R_2 \times R_3 \quad (47)$$

Where:

$$R_{total} = \begin{bmatrix} \cos\varphi\cos\theta\cos\psi - \sin\varphi\sin\psi & -\cos\varphi\cos\theta\sin\psi - \sin\varphi\cos\psi & \cos\phi\sin\theta \\ \sin\varphi\cos\theta\cos\psi + \cos\phi\sin\psi & -\sin\varphi\cos\theta\sin\psi + \cos\phi\cos\psi & \sin\psi\sin\theta \\ -\sin\theta\cos\psi & \sin\theta\sin\psi & \cos\theta \end{bmatrix} \quad (48)$$

Inserting matrix from Equation 48 into Equation 47 the global magnetic field is solved:

$$\begin{bmatrix} B_x^G \\ B_y^G \\ B_z^G \end{bmatrix} = \begin{bmatrix} \cos\varphi\cos\theta\cos\psi - \sin\varphi\sin\psi & -\cos\varphi\cos\theta\sin\psi - \sin\varphi\cos\psi & \cos\phi\sin\theta \\ \sin\varphi\cos\theta\cos\psi + \cos\phi\sin\psi & -\sin\varphi\cos\theta\sin\psi + \cos\phi\cos\psi & \sin\psi\sin\theta \\ -\sin\theta\cos\psi & \sin\theta\sin\psi & \cos\theta \end{bmatrix}^{-1} \begin{bmatrix} B_x^L \\ B_y^L \\ B_z^L \end{bmatrix} \quad (49)$$

Knowing that $R^{-1} = R^T$ Equation 49 becomes:

$$\begin{bmatrix} B_x^G \\ B_y^G \\ B_z^G \end{bmatrix} = \begin{bmatrix} \cos\varphi\cos\theta\cos\psi - \sin\varphi\sin\psi & \sin\varphi\cos\theta\cos\psi + \cos\phi\sin\psi & -\sin\theta\cos\psi \\ -\cos\varphi\cos\theta\sin\psi - \sin\varphi\cos\psi & -\sin\varphi\cos\theta\sin\psi + \cos\phi\cos\psi & \sin\theta\sin\psi \\ \cos\phi\sin\theta & \sin\psi\sin\theta & \cos\theta \end{bmatrix} \begin{bmatrix} B_x^L \\ B_y^L \\ B_z^L \end{bmatrix} \quad (50)$$

Equation 50 solves for the total magnetic field in global coordinates. Knowing Equations 43 and 50, the total magnetic field can be solved for any array of magnets.

CHAPTER 3: Mathematical Analysis

First a 2-D analysis was solved in local coordinates to understand the magnetic field directly under the magnet array of the dual rotating unit. A Halbach array was then solved to determine the magnetic field to validate the theory outlined in Section 2.1. After validating the local to global theory from Section 2.1 the dual rotating unit was analyzed in 3-D while in rotation.

3.1. Local 2-D Mathematical Analysis

The two magnets are spaced 3 inches apart on a horizontal plane, reading subterranean objects that are at least 6 inches below the unit. The total magnetic field measurement is solved for 6 inches below the middle point between the two magnets, seen in Figure 10. This is the point of interest because 6 inches below the two magnets is the sensing region and understanding the field interaction in this region is crucial to the viability and sensitivity of the unit.

The two magnets are spaced 3 inches apart, measured from the center of each magnet. This corresponds to $a = 1.5in$. First r_1 and r_2 are solved using the Pythagorean theorem.

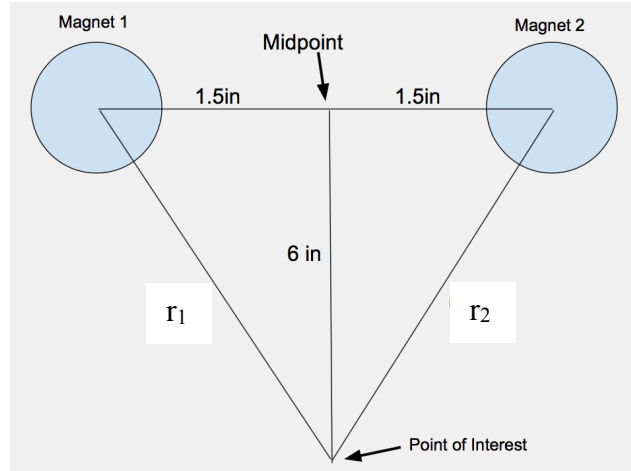


Figure 10: Point of Interest Geometrical Relationship

Where $r = r_1 = r_2$ is the distance from the center of the magnet to the point of interest.

$$a^2 + b^2 = r^2 \quad (51)$$

Where $a = 1.5in = 0.0381 m$, $b = -6.0in = -0.1524 m$, solving we get $r = 6.185in = 0.157 m$.

In order to determine the angle θ_1 the geometric relation seen in Figure 11 was constructed. Where θ_1 is the angle from the vector pointing north to \hat{r}_1 . It was determined that $\theta_1 = 165.96^\circ$ or 284.05° .

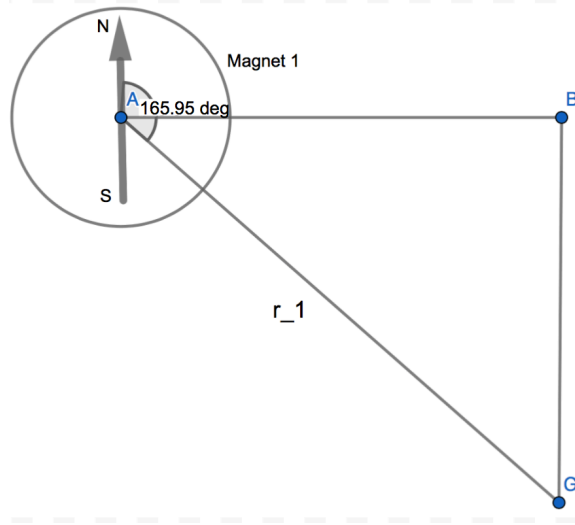


Figure 11: Magnet 1 Geometrical Relationship

The same process was used to determine θ_2 from Figure 12. Where θ_2 is the angle from vector pointing north to \hat{r}_2 . It was determined that $\theta_2 = 324.95^\circ$ or 75.95° .

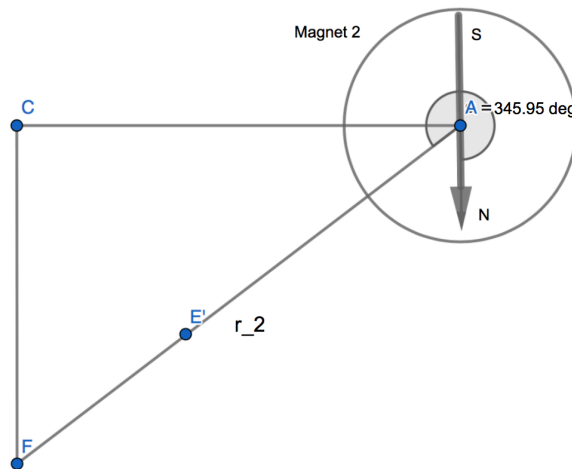


Figure 12: Magnet 2 Geometrical Relationship

Since both are the same NdFeB N52 magnet, the properties are nominally identical.

Let $k = \frac{2\pi}{\lambda} \approx 40.0 \text{ m}^{-1}$, $\epsilon_0 = 8.854 \times 10^{-12} \frac{\text{F}}{\text{m}}$, $c = 299,792,458 \frac{\text{m}}{\text{s}}$, $\mu_0 = 1.32 \times$

$10^{-6} \frac{H}{m}$, $\hat{r}_1 = \frac{1}{0.1570} [0.0381 \quad -0.1524]$, and $\hat{r}_2 = \frac{1}{0.1570} [-0.0381 \quad -0.1524]$. Use the following equation to solve for m_0 .

$$m_0 = \frac{4\pi a^3}{3\mu_0} = 175.51 \frac{m^4}{H} \quad (52)$$

Where $a = 4.5in = 0.1143 m$, the distance from point A to point C in Figure 12.

Now taking Equation 17 and inserting the known variables:

$$\mathbf{B} \approx - \frac{(40.02 m^{-1})^2 \left(175.51 \frac{m^4}{H} \right)}{(6.28)4\pi \left(8.854 \times 10^{-12} \frac{F}{m} \right) \left(299,792,458 \frac{m}{s} \right)^2} \left\{ \frac{1}{0.1570} \cos(165.95) [0.0381 \quad -0.1524] + \frac{1}{0.1570} \cos(345.95) [-0.0381 \quad -0.1524] \right\} \quad (53)$$

The y components of \hat{r} cancel out, leaving:

$$\mathbf{B} \approx [0.002 \quad 0.000] T \quad (54)$$

And the total magnitude of \mathbf{B} :

$$|\mathbf{B}| \approx 0.002 T \quad (55)$$

3.2. Halbach Array Analysis

3.2.1 Mathematical Confirmation

The magnetic field of a simple 5 cube Halbach array is solved in the following mathematical analysis to confirm the global to local theory described in Section 2.1. Unlike the analysis in Section 3.1 the Halbach analysis must be solved in global coordinates to account for the distance and magnetic field orientation changes between magnets. A

Halbach array should have a canceled field on one side of the array and augmented field on the other, as seen in Figure 13.

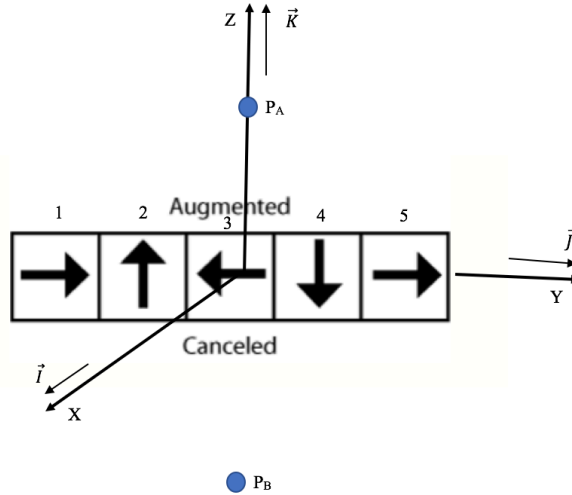


Figure 13: Halbach Array

To calculate the magnetic field at points P_A and P_B the following steps are taken. Let point P_A be a point in the augmented field at position $(0,0,2)$ and point P_B be a point in the canceled field at position $(0, 0, -2)$. As described in Section 2.2 the magnetic field must first be calculated in global coordinates for each magnet. Let each magnet have a length of 1. The process for solving the magnetic field for the first magnet is explained below.

Magnet 1:

Magnet 1 is at position $(0, -2, 0)$.

$$\vec{P}_{01} = -2\vec{j} \quad (56)$$

$$\vec{r}_{A1}^G = \vec{P}_A - \vec{P}_{01} = 2\vec{j} + 2\vec{k} \quad (57)$$

$$\vec{r}_{C1}^G = \vec{P}_C - \vec{P}_{01} = 2\vec{j} - 2\vec{k} \quad (58)$$

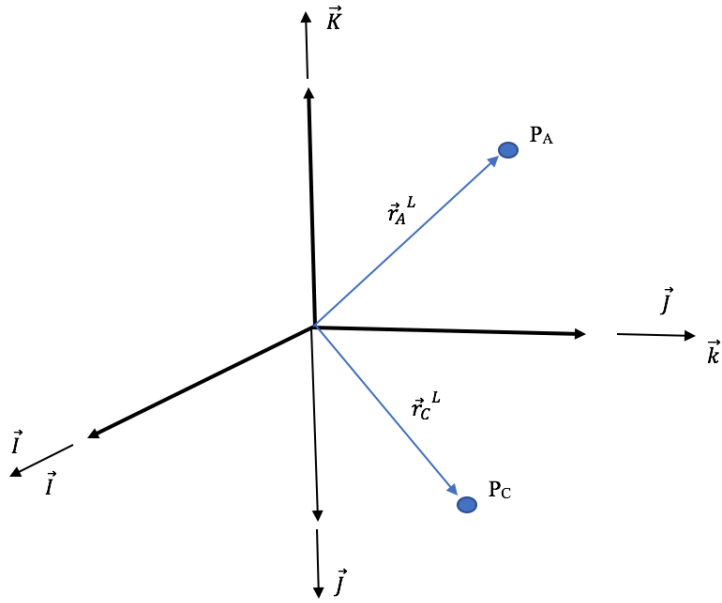


Figure 14: Rotation Coordinates

By inspection of the magnetic field vector in Figure 13 of magnet 1 and the coordinate system in Figure 14 the rotation matrix has the form:

$$R_1 = \begin{bmatrix} 1 & 0 & 0 \\ 0 & 0 & -1 \\ 0 & 1 & 0 \end{bmatrix} \quad (59)$$

Using the rotation matrix to solve for \vec{r}_A^L and \vec{r}_C^L :

$$\vec{r}_A^L = \begin{bmatrix} 0 \\ -2 \\ 2 \end{bmatrix} = \begin{bmatrix} 1 & 0 & 0 \\ 0 & 0 & -1 \\ 0 & 1 & 0 \end{bmatrix} \begin{bmatrix} 0 \\ 2 \\ 2 \end{bmatrix} \quad (60)$$

$$\vec{r}_C^L = \begin{bmatrix} 0 \\ 2 \\ 2 \end{bmatrix} = \begin{bmatrix} 1 & 0 & 0 \\ 0 & 0 & -1 \\ 0 & 1 & 0 \end{bmatrix} \begin{bmatrix} 0 \\ 2 \\ -2 \end{bmatrix} \quad (61)$$

By inspection the angles θ and φ shown in Figure 8 for both points A and C are:

$$\theta_{A1} = \theta_{C1} = \frac{\pi}{4} \quad (62)$$

$$\varphi_{A1} = \frac{3\pi}{2} \quad (63)$$

$$\varphi_{C1} = \frac{\pi}{2} \quad (64)$$

Letting $C = \frac{\mu}{4\pi} = 1$ and using the angles θ and φ and Equations 62 through 64 the

X, Y and Z components of the magnetic field are solved in local coordinates at points A

and C.

$$B_{AX1}^L = \frac{\sqrt{2}}{32} \cdot 3 \cdot \frac{\sqrt{2}}{2} \cdot \frac{\sqrt{2}}{2} \cdot 0 = 0 \quad (65)$$

$$B_{AY1}^L = \frac{\sqrt{2}}{32} \cdot 3 \cdot \frac{\sqrt{2}}{2} \cdot \frac{\sqrt{2}}{2} \cdot -1 = -\frac{3\sqrt{2}}{64} \quad (66)$$

$$B_{AZ1}^L = \frac{\sqrt{2}}{32} \left[2 \cdot \left(\frac{\sqrt{2}}{2} \right)^2 - \left(\frac{\sqrt{2}}{2} \right)^2 \right] = \frac{\sqrt{2}}{64} \quad (67)$$

$$B_{CX1}^L = \frac{\sqrt{2}}{32} \cdot 3 \cdot \frac{\sqrt{2}}{2} \cdot \frac{\sqrt{2}}{2} \cdot 0 = 0 \quad (68)$$

$$B_{CY1}^L = \frac{\sqrt{2}}{32} \cdot 3 \cdot \frac{\sqrt{2}}{2} \cdot \frac{\sqrt{2}}{2} \cdot -1 = -\frac{3\sqrt{2}}{64} \quad (69)$$

$$B_{CZ1}^L = \frac{\sqrt{2}}{32} \left[2 \cdot \left(\frac{\sqrt{2}}{2} \right)^2 - \left(\frac{\sqrt{2}}{2} \right)^2 \right] = \frac{\sqrt{2}}{64} \quad (70)$$

Now converting back to global coordinates using Equation 39.

$$\begin{bmatrix} B_x^G \\ B_y^G \\ B_z^G \end{bmatrix} = \begin{bmatrix} 1 & 0 & 0 \\ 0 & 0 & -1 \\ 0 & 1 & 0 \end{bmatrix}^T \begin{bmatrix} B_x^L \\ B_y^L \\ B_z^L \end{bmatrix} \quad (71)$$

$$\vec{B}_{A1}^G = \begin{bmatrix} 0 \\ \frac{\sqrt{2}}{64} \\ \frac{3\sqrt{2}}{64} \\ \frac{\sqrt{2}}{64} \end{bmatrix} = \begin{bmatrix} 1 & 0 & 0 \\ 0 & 0 & 1 \\ 0 & -1 & 0 \end{bmatrix} \begin{bmatrix} 0 \\ -\frac{3\sqrt{2}}{64} \\ \frac{\sqrt{2}}{64} \end{bmatrix} \quad (72)$$

$$\vec{B}_{C1}^G = \begin{bmatrix} 0 \\ \frac{\sqrt{2}}{64} \\ -\frac{3\sqrt{2}}{64} \\ \frac{\sqrt{2}}{64} \end{bmatrix} = \begin{bmatrix} 1 & 0 & 0 \\ 0 & 0 & 1 \\ 0 & -1 & 0 \end{bmatrix} \begin{bmatrix} 0 \\ \frac{3\sqrt{2}}{64} \\ \frac{\sqrt{2}}{64} \end{bmatrix} \quad (73)$$

Magnets 2-5:

Carrying out the same process for magnets 2 through 5 the following magnetic fields are found in global coordinates. Note that the local field of magnet 2 aligns with the global coordinate system, so the global and local magnetic fields are identical. Additionally, magnet 4 is the same as magnet 2 with inverted symmetry and magnet 5 is the same as magnet 1 with reflected symmetry.

$$\vec{B}_{A2}^G = \begin{bmatrix} 0 \\ \frac{6\sqrt{5}}{125} \\ \frac{7\sqrt{5}}{125} \\ \frac{\sqrt{5}}{125} \end{bmatrix} \quad \vec{B}_{C2}^G = \begin{bmatrix} 0 \\ -\frac{6\sqrt{5}}{125} \\ \frac{7\sqrt{5}}{125} \\ \frac{\sqrt{5}}{125} \end{bmatrix} \quad (74)$$

$$\vec{B}_{A3}^G = \begin{bmatrix} 0 \\ 1 \\ 8 \\ 0 \end{bmatrix} \quad \vec{B}_{C3}^G = \begin{bmatrix} 0 \\ 1 \\ 8 \\ 0 \end{bmatrix} \quad (75)$$

$$\vec{B}_{A4}^G = \begin{bmatrix} 0 \\ \frac{6\sqrt{5}}{125} \\ -\frac{7\sqrt{5}}{125} \\ \frac{7\sqrt{5}}{125} \end{bmatrix} \quad \vec{B}_{C4}^G = \begin{bmatrix} 0 \\ \frac{-6\sqrt{5}}{125} \\ \frac{-7\sqrt{5}}{125} \\ \frac{7\sqrt{5}}{125} \end{bmatrix} \quad (76)$$

$$\vec{B}_{A5}^G = \begin{bmatrix} 0 \\ \frac{3\sqrt{2}}{64} \\ \frac{\sqrt{2}}{64} \\ \frac{\sqrt{2}}{64} \end{bmatrix} \quad \vec{B}_{C5}^G = \begin{bmatrix} 0 \\ \frac{-3\sqrt{2}}{64} \\ \frac{\sqrt{2}}{64} \\ \frac{\sqrt{2}}{64} \end{bmatrix} \quad (77)$$

Adding all the magnetic fields up for point A (augmented) and Point C (canceled).

$$\begin{aligned} \vec{B}_{A_{total}}^G &= \vec{B}_{A1}^G + \vec{B}_{A2}^G + \vec{B}_{A3}^G + \vec{B}_{A4}^G + \vec{B}_{A5}^G = \begin{bmatrix} 0 \\ \frac{\sqrt{2}}{64} \\ \frac{3\sqrt{2}}{64} \\ \frac{3\sqrt{2}}{64} \end{bmatrix} + \begin{bmatrix} 0 \\ \frac{6\sqrt{5}}{125} \\ \frac{7\sqrt{5}}{125} \\ \frac{7\sqrt{5}}{125} \end{bmatrix} + \\ &\begin{bmatrix} 0 \\ 1 \\ 8 \\ 0 \end{bmatrix} + \begin{bmatrix} 0 \\ \frac{6\sqrt{5}}{125} \\ \frac{-7\sqrt{5}}{125} \\ \frac{7\sqrt{5}}{125} \end{bmatrix} + \begin{bmatrix} 0 \\ \frac{3\sqrt{2}}{64} \\ \frac{\sqrt{2}}{64} \\ \frac{\sqrt{2}}{64} \end{bmatrix} = \begin{bmatrix} 0 \\ 0.643 \\ 0 \end{bmatrix} \end{aligned} \quad (78)$$

$$\begin{aligned} \vec{B}_{C_{total}}^G &= \vec{B}_{C1}^G + \vec{B}_{C2}^G + \vec{B}_{C3}^G + \vec{B}_{C4}^G + \vec{B}_{C5}^G = \begin{bmatrix} 0 \\ \frac{\sqrt{2}}{64} \\ \frac{3\sqrt{2}}{64} \\ \frac{3\sqrt{2}}{64} \end{bmatrix} + \begin{bmatrix} 0 \\ \frac{-6\sqrt{5}}{125} \\ \frac{7\sqrt{5}}{125} \\ \frac{7\sqrt{5}}{125} \end{bmatrix} + \\ &\begin{bmatrix} 0 \\ 1 \\ 8 \\ 0 \end{bmatrix} + \begin{bmatrix} 0 \\ \frac{-6\sqrt{5}}{125} \\ \frac{-7\sqrt{5}}{125} \\ \frac{7\sqrt{5}}{125} \end{bmatrix} + \begin{bmatrix} 0 \\ \frac{-3\sqrt{2}}{64} \\ \frac{\sqrt{2}}{64} \\ \frac{\sqrt{2}}{64} \end{bmatrix} = \begin{bmatrix} 0 \\ -0.045 \\ 0 \end{bmatrix} \end{aligned} \quad (79)$$

The mathematical analysis confirms the theory in Section 2.2 is correct because it shows that for one side of the Halbach array the field is augmented and the other side of the field is canceled.

3.2.2 Analysis of Halbach Array

To take the analysis one step further a Matlab code was written (see Appendix A) to plot the vector field of a Halbach array. The vector field was plotted using the multipole theory explained above and each magnet has the same polar orientation as in Figure 13. Each vector is solved in global coordinates by adding all 5 magnetic fields together. The results are shown in the following plot.

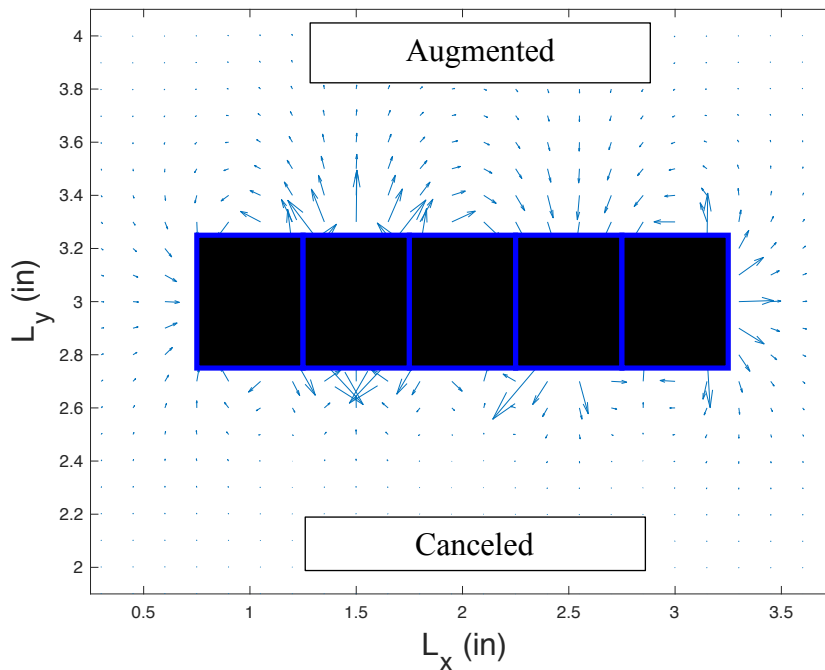


Figure 15: Vector Plot of Halbach Array

In Figure 15 on the bottom side of the 5 magnets (black outlined in blue) it is shown that the vectors disappear quickly as they move in the negative y direction, reflecting the canceled side of the array. On the top side of the 5 magnets it is shown that the vectors appear longer when compared to the bottom side of the array, reflecting the augmented side of the array.

3.3 Rotating Dual Magnet Analysis

By validating the theory explained in Section 2.1 by solving the Halbach array, a spinning analysis was then carried out on two diametrically polarized cylinder magnets (see code Appendix A). The goal is to have a better understanding of what the magnetic fields look like during the rotation of the two magnets. From Section 3.3.4 a polar opposite orientation is determined to be effective for detecting subsurface objects, that orientation was used for the spinning analysis. The vector fields were solved at 15-degree increments. The 12 different orientations are outlined in the table below.

Table 1: 12 Different Orientations

Orientation	Magnet 1	Magnet 2
1	0	180
2	15	195
3	30	210
4	45	225
5	60	240
6	75	255
7	90	270
8	105	285
9	120	300
10	135	315
11	150	330
12	165	345

The other half of the rotation from 180° to 360° for magnet 1 and 360° to 180° for magnet 2 is the same as the 12 polar orientations above, except that the magnet orientation is flipped, resulting in the same field as the first half of the rotation. Below are vector plots of the 12 orientations listed in the above table. The vectors have been normalized to get a better understanding of how the fields interact.

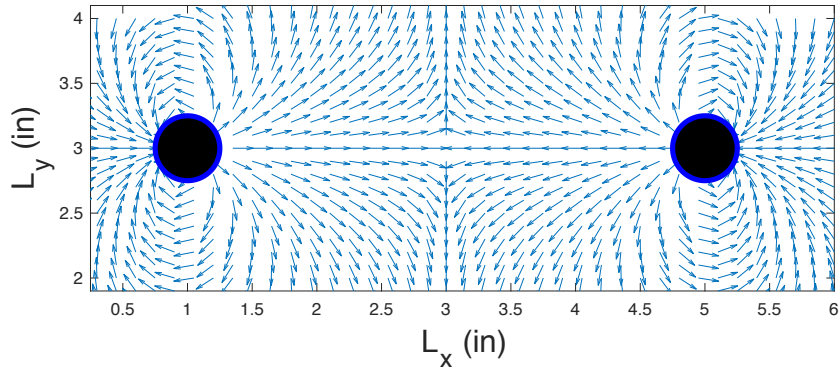


Figure 16: Polar Alignment of Magnet 1: 0° and Magnet 2: 180°

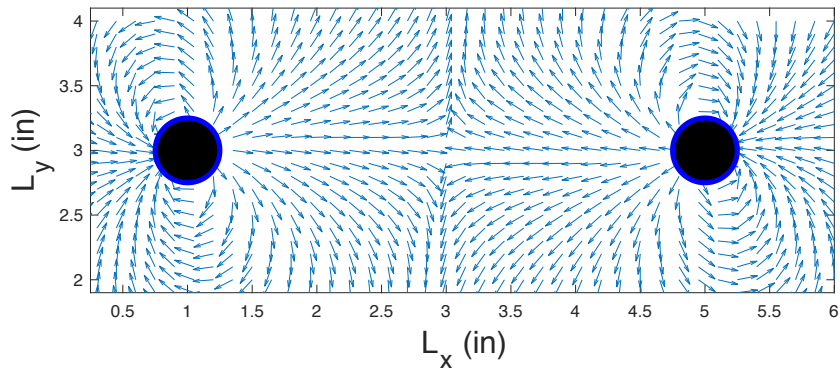


Figure 17: Polar Alignment of Magnet 1: 15° and Magnet 2: 195°

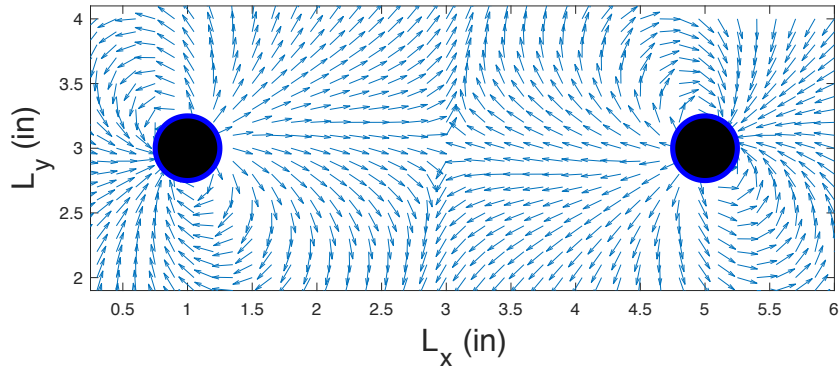


Figure 18: Polar Alignment of Magnet 1: 30° and Magnet 2: 210°

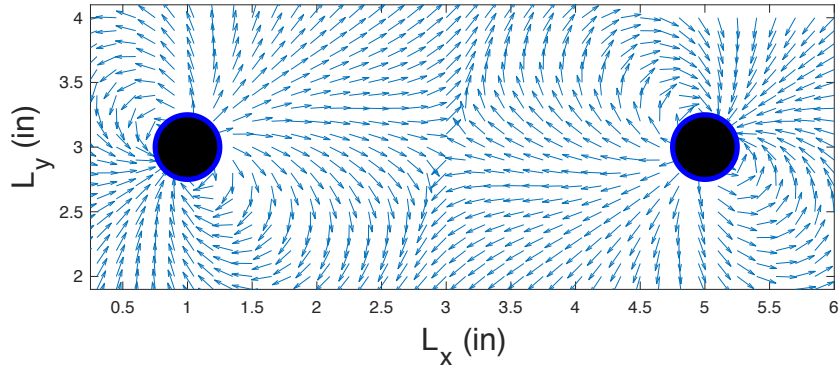


Figure 19: Polar Alignment of Magnet 1: 45° and Magnet 2: 225°

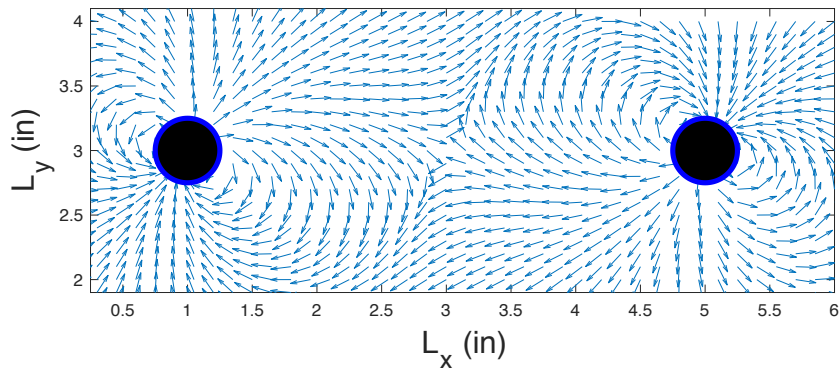


Figure 20: Polar Alignment of Magnet 1: 60° and Magnet 2: 240°

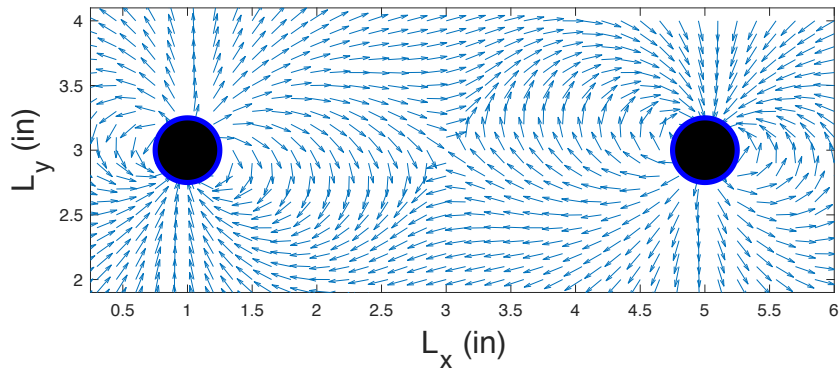


Figure 21: Polar Alignment of Magnet 1: 75° and Magnet 2: 255°

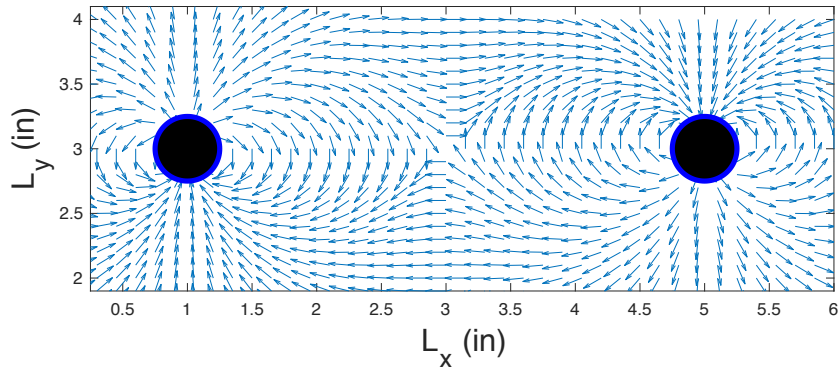


Figure 22: Polar Alignment of Magnet 1: 90° and Magnet 2: 270°

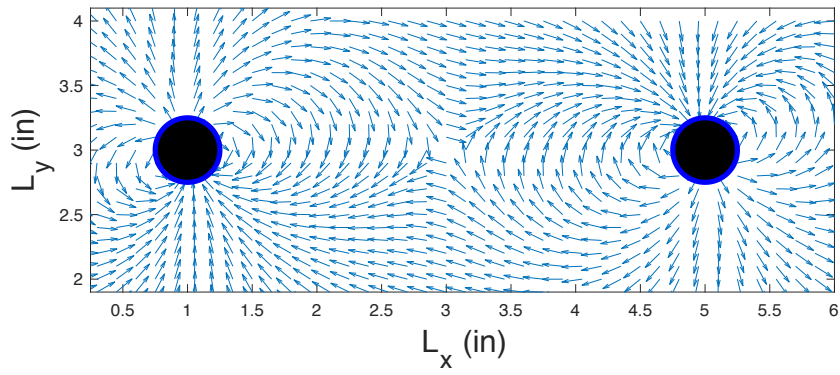


Figure 23: Polar Alignment of Magnet 1: 105° and Magnet 2: 285°

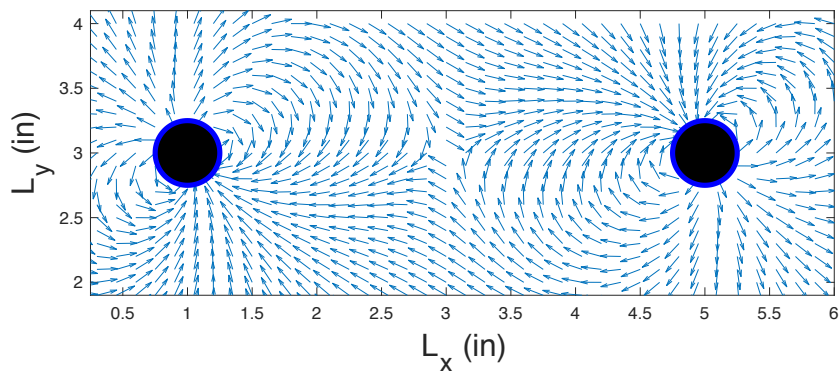


Figure 24: Polar Alignment of Magnet 1: 120° and Magnet 2: 300°

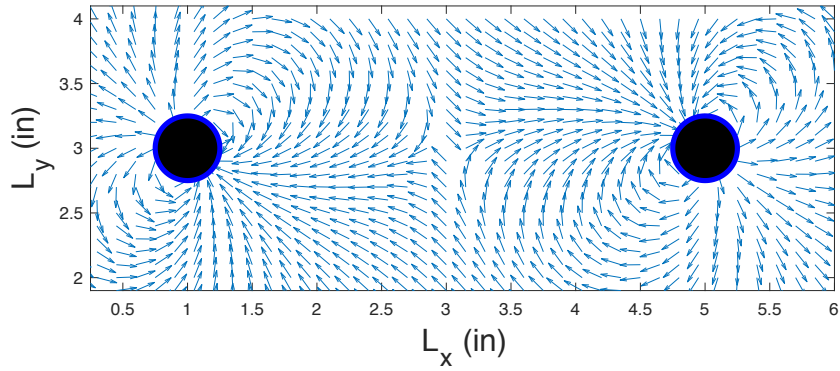


Figure 25: Polar Alignment of Magnet 1: 135° and Magnet 2: 315°

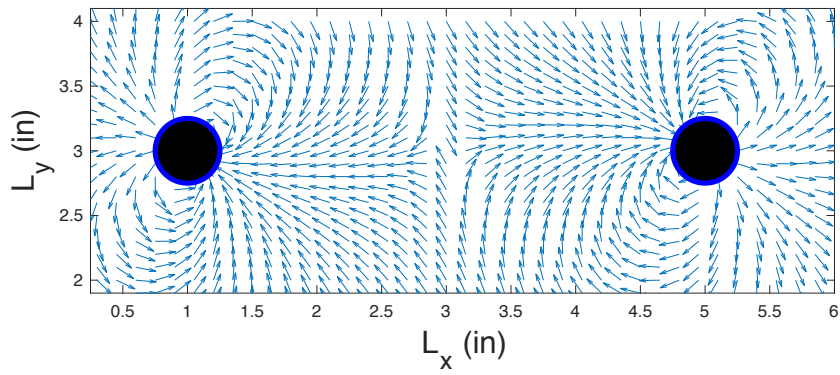


Figure 26: Polar Alignment of Magnet 1: 150° and Magnet 2: 330°

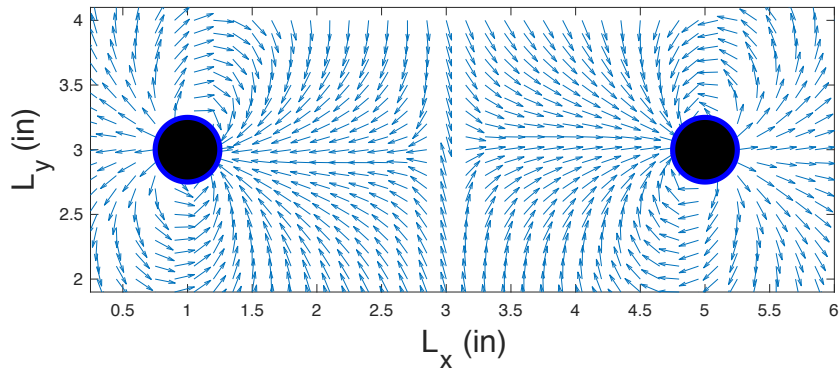


Figure 27: Polar Alignment of Magnet 1: 165° and Magnet 2: 345°

From Figure 16 through Figure 27 it is shown that during a full 360 degree rotation the strongest magnetic field above and below the magnets occurs when magnets 1 and 2 are aligned at either 90° and 270° or 270° and 90° respectively, as seen in Figure 22. This

is apparent because the vector fields perfectly align to combine and increase the field above and below the magnets. As the angle changes, the field vectors do not align completely and therefore add, but do not combine to the same magnitude and direction as the 90° and 270° or 270° and 90° orientations.

3.4. FEA Comparison

Finite Element Method Magnets (FEMM) software was used to run a finite element analysis (FEA) on both the dual magnet array and Halbach array. To validate the results the magnetic flux density ($|B|$) values from the FEA were compared to the results from the mathematical analyses Sections 3.1 and 3.2.

3.4.1 Dual Rotating Magnet Comparison

The setup is the same as in Section 3.1, the magnets are spaced 3 inches apart and the point of interest is 6 inches below the magnets. The following results were recorded from the FEA. First the magnitude of the magnetic flux density was plotted. The flux density variations are represented by the color scale seen in Figure 28.

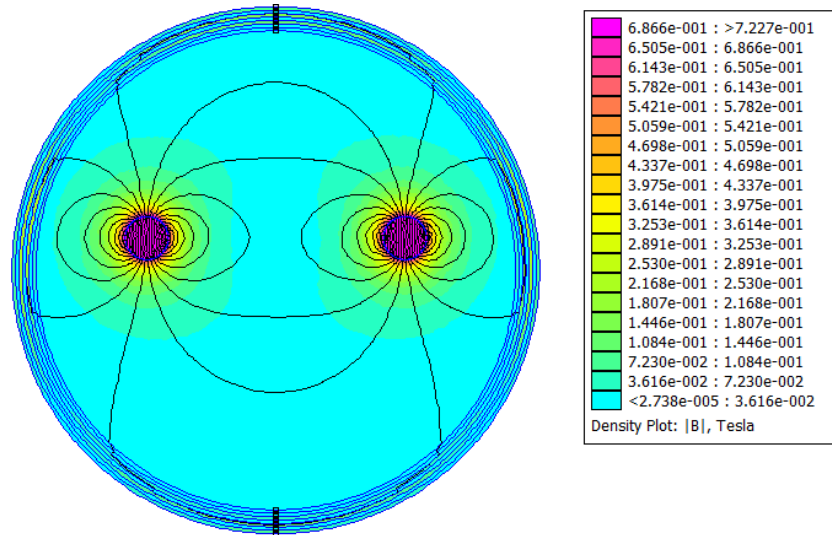


Figure 28: Magnetic Flux Density Plot with 9-inch Spacing Between Magnets

In order to solve for the value of the magnetic flux, density at 6 inches below the unit the following 2-D plot was graphed. The values were recorded from Figure 28 and then plotted in a magnetic flux density vs. time coordinate system.

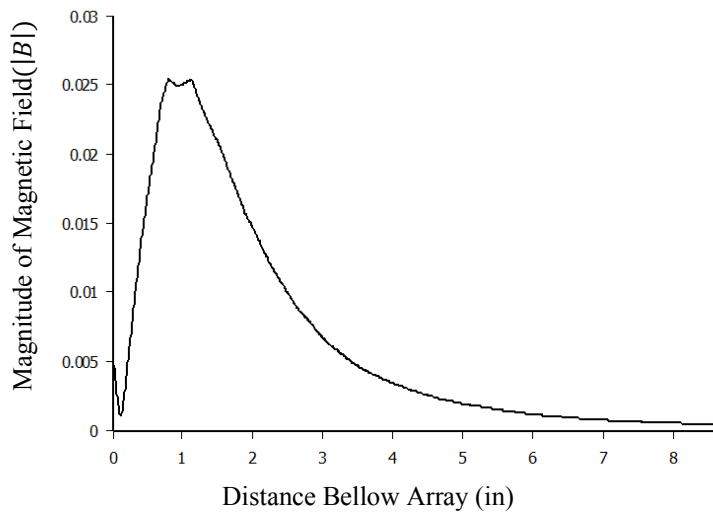


Figure 29: Magnetic Flux Density vs. Distance with 3in Magnet Spacing

The maximum magnetic flux density value occurs around 1 inch and then quickly decreases. At 6 inches below the magnets the magnetic flux density equals ~ 0.002 Tesla (T). When comparing the results from Section 3.1 to 3.4.1, the total magnitude of magnetic field flux density is equal when measured 6 inches below the magnets, validating the 2-D mathematical analysis.

3.4.2 Halbach Array FEA Analysis

Section 3.4.1 proves the accuracy of the FEMM software so a Halbach array FEA analysis was used to solve for the magnetic field at a point 6 inches below the array. The following results were recorded from the FEA simulation.

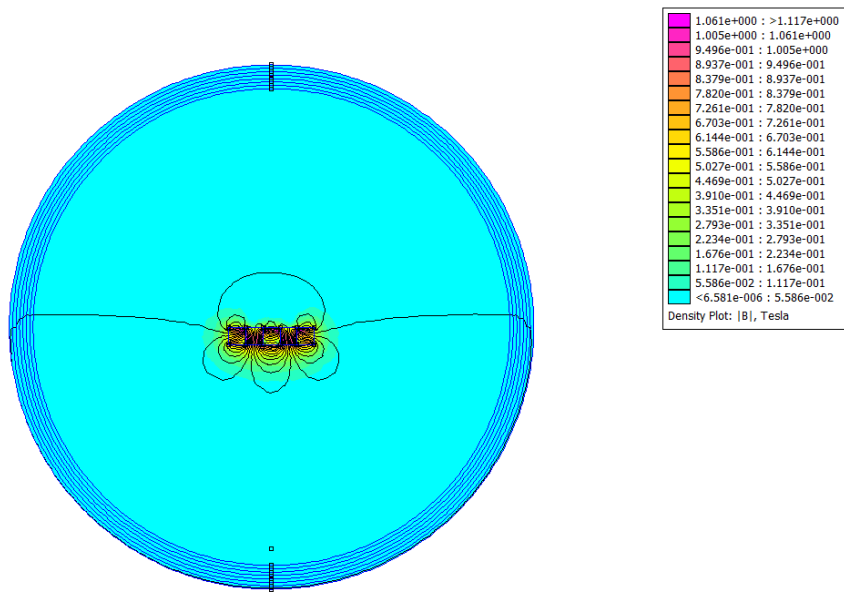


Figure 30: FEA of Halbach Array

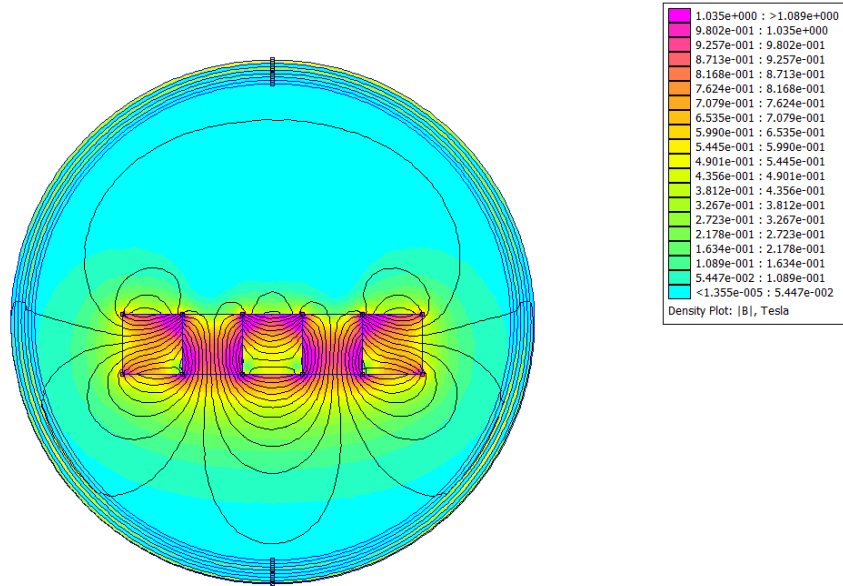


Figure 31: Closeup FEA of Halbach Array

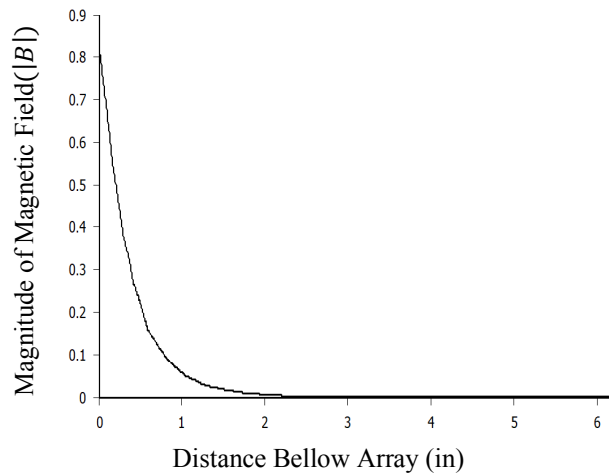


Figure 32: Magnetic Flux Density vs. Distance Plot of Halbach Array

Analyzing Figure 32 the maximum magnetic flux density value occurs at the array, and as the distance increases the $|B|$ values drop rapidly to zero. At the point 6 inches below the array $|B| \sim 0.0$ T.

3.5 FEA Perturbation Analysis

The viability of the magnetic sensing device depends on how well the magnetic field created by the spinning magnets can interact with a subsurface object of interest. When the magnetometer is reading the induced magnetic field from the magnets and a ferrous subsurface object is underneath the sensing unit, the magnetometer reading ($|B|$) varies depending on the subsurface objects level of magnetic saturation. The maximum sensitivity of the sensing unit corresponds to when the ferrous object reaches complete saturation. To achieve this the spinning magnets must create the maximum magnetic field below the magnets in order to saturate the object. A series of FEA simulations will determine the best polar orientation for each magnet of the dual magnet unit and the viability of the Halbach array.

3.5.1 Dual Magnet FEA

For the FEA simulation of the dual magnet array, each magnet is rotated in increments of 90 degrees and all 10 possible combinations for the magnets are simulated. There is an iron bar inserted 6 inches below the magnets to simulate a subsurface object of interest, as seen in Figure 33. A total field magnitude of magnetic flux density plot and magnetic flux vs. distance plot was constructed for each magnet orientation.

Table 2: 10 Possible Magnet Orientations

Orientation Number	Magnet 1 Orientation (Degrees)	Magnet 2 Orientation (Degrees)
1	0	0
2	0	90
3	0	180
4	0	270
5	90	90
6	90	180
7	90	270
8	180	180
9	180	270
10	270	270

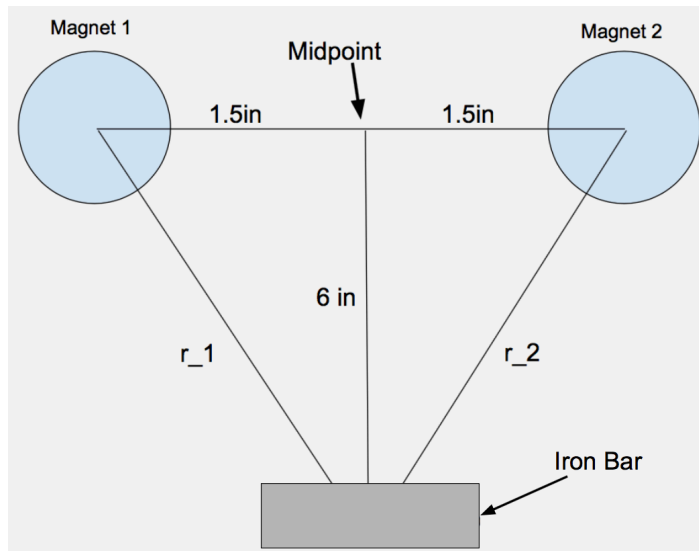


Figure 33: Iron Bar Geometrical Relationship

Orientation 1:

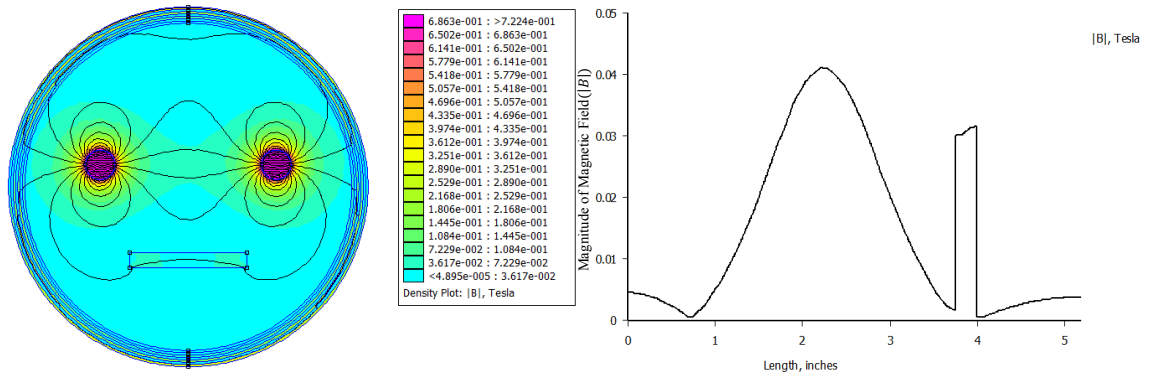


Figure 34: Magnet 1: 0° Magnet 2: 0°

Observing Figure 34 the maximum magnitude of magnetic flux density value ($|B|$) is equal to 0.042 Tesla directly between the two magnets and 0.03 Tesla in the iron bar.

Orientation 2:

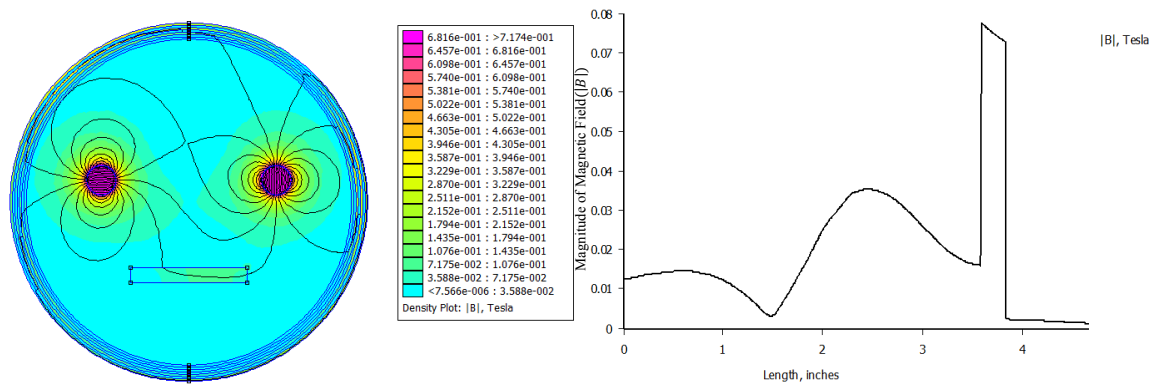


Figure 35: Magnet 1: 0° Magnet 2: 90°

Observing Figure 35 the maximum value of $|B|$ is equal to 0.03 Tesla in the iron bar.

Orientation 3:

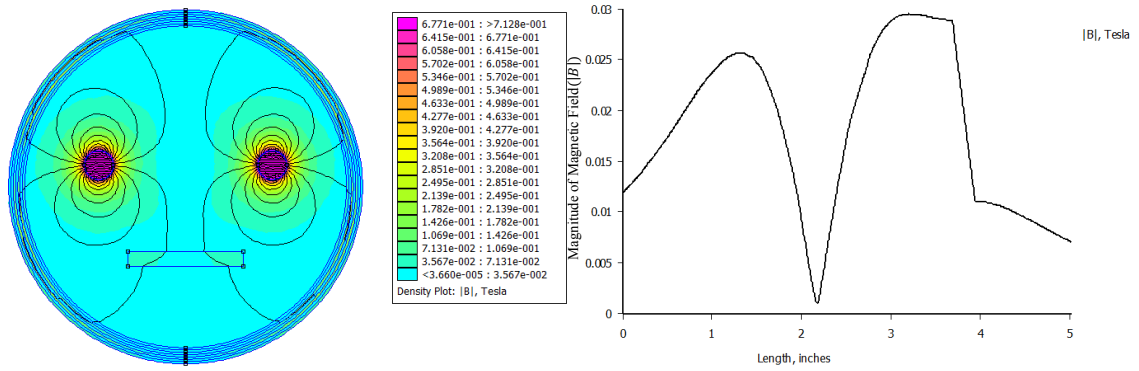


Figure 36: Magnet 1: 0° Magnet 2: 180°

Observing Figure 36 the maximum $|B|$ value is equal to 0.03 Tesla in the iron bar.

Orientation 4:

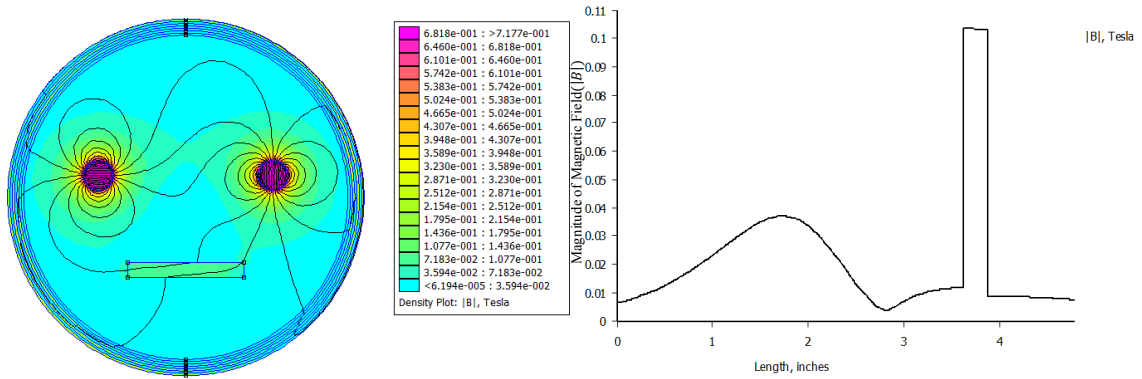


Figure 37: Magnet 1: 0° Magnet 2: 270°

Observing Figure 37 the maximum $|B|$ value is equal to 0.105 Tesla in the iron bar.

Orientation 5:

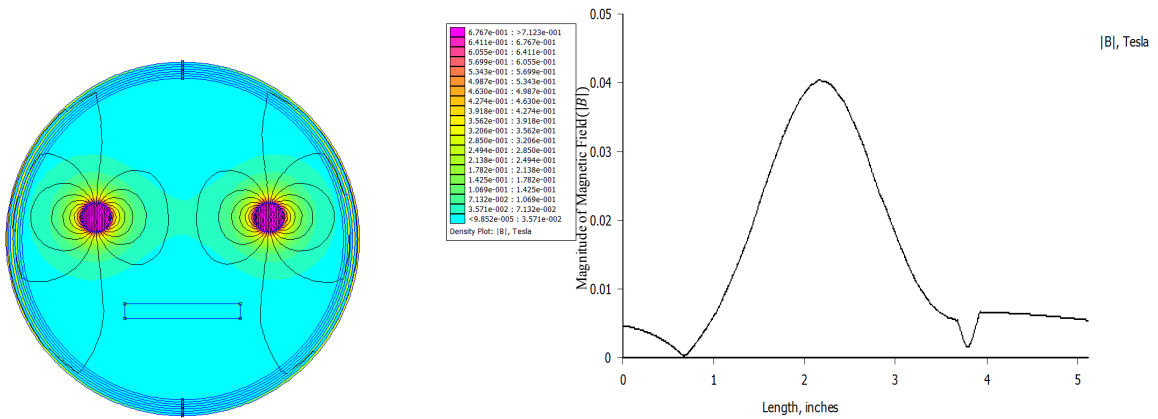


Figure 38: Magnet 1: 90° Magnet 2: 90°

Observing Figure 38 the maximum $|B|$ value is equal to 0.04 Tesla between the two magnets and 0.009 Tesla in the iron bar.

Orientation 6:

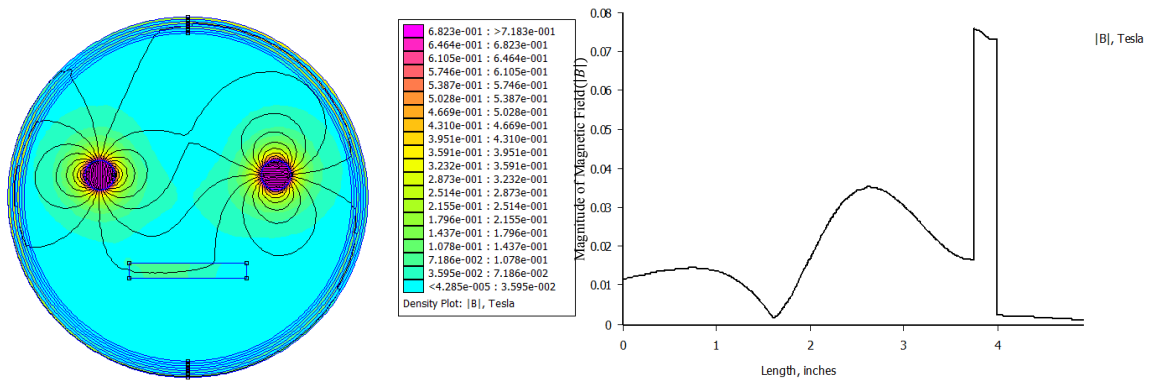


Figure 39: Magnet 1: 90° Magnet 2: 180°

Observing Figure 39 the maximum $|B|$ value is equal to 0.078 Tesla in the iron bar.

Orientation 7:

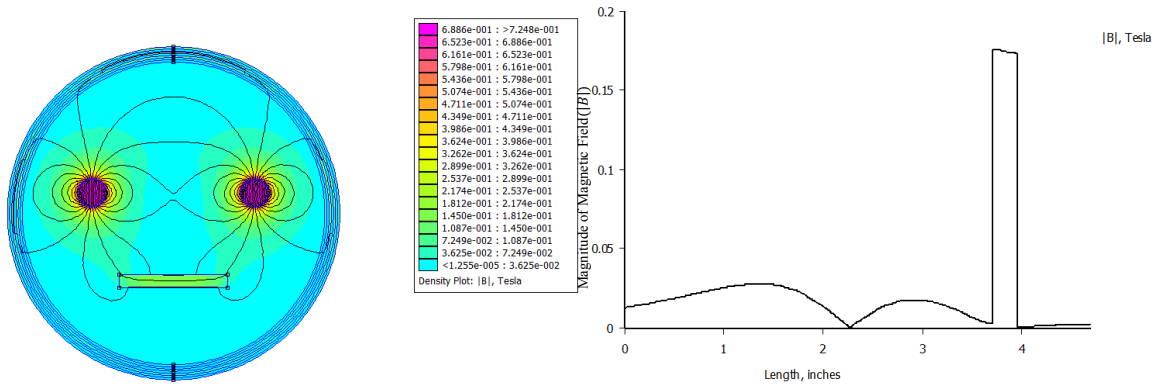


Figure 40: Magnet 1: 90° Magnet 2: 270°

Observing Figure 40 the maximum $|B|$ value is equal to 0.18 Tesla in the iron bar.

Orientation 8:

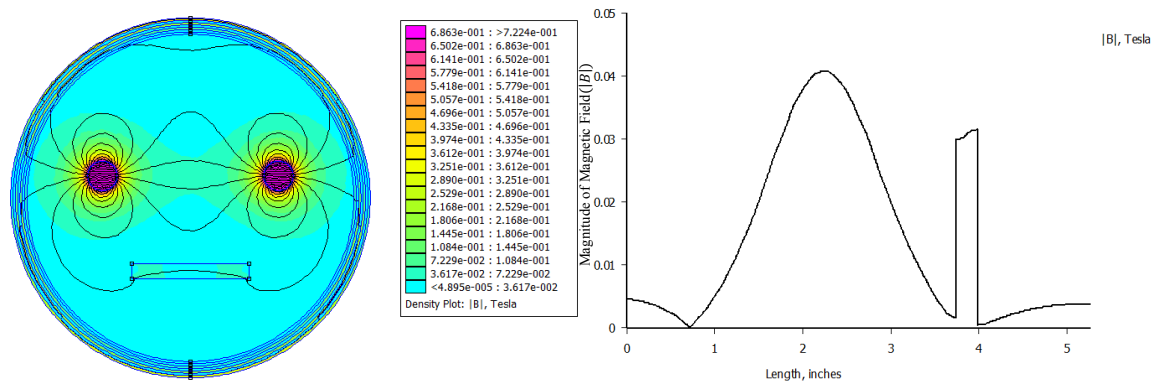


Figure 41: Magnet 1: 180° Magnet 2: 180°

Observing Figure 41 the maximum $|B|$ value is equal to 0.042 Tesla between the two magnets and 0.033 Tesla in the iron bar.

Orientation 9:

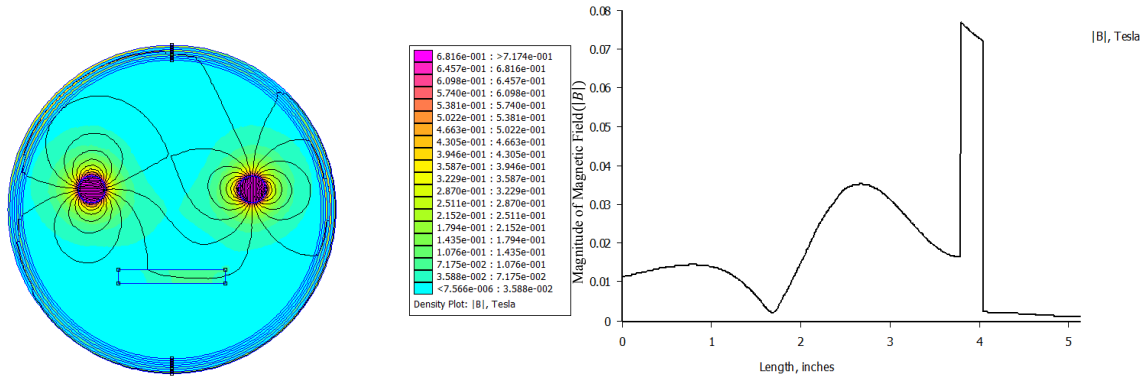


Figure 42: Magnet 1: 180° Magnet 2: 270°

Observing Figure 42 the maximum $|B|$ value is equal to 0.078 Tesla in the iron bar.

Orientation 10:

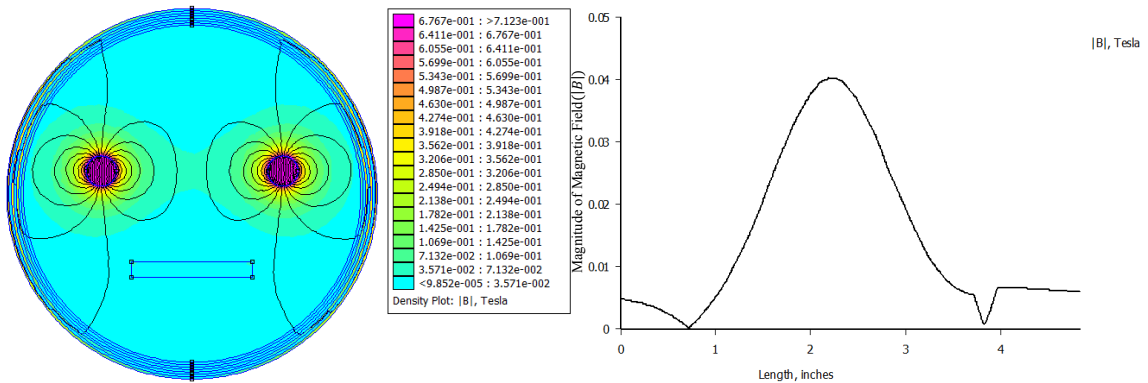


Figure 43: Magnet 1: 270° Magnet 2: 270°

Observing Figure 43 the maximum $|B|$ value is equal to 0.04 Tesla between the two magnets and 0.009 Tesla in the iron bar.

After analyzing each FEA simulation for the 10 different possible orientations, it is apparent that Orientation 7 has the largest change in flux density of approximately 0.18 Tesla in the iron bar. The polar orientation (north end of the magnet) of magnet 1 is at 90° from 0° and magnet 2 is 270° from 0°. This orientation will allow for a maximum sensing range and accuracy for detecting subsurface ferromagnetic objects.

3.5.2 Halbach Array FEA

The Halbach array is orientated such that the strong field side is aligned with the added perturbation. As in Section 3.5.1 the perturbation is a pure iron bar located 6 inches below the array. A total field magnitude of magnetic flux density plot and magnetic flux vs. distance plot was constructed.

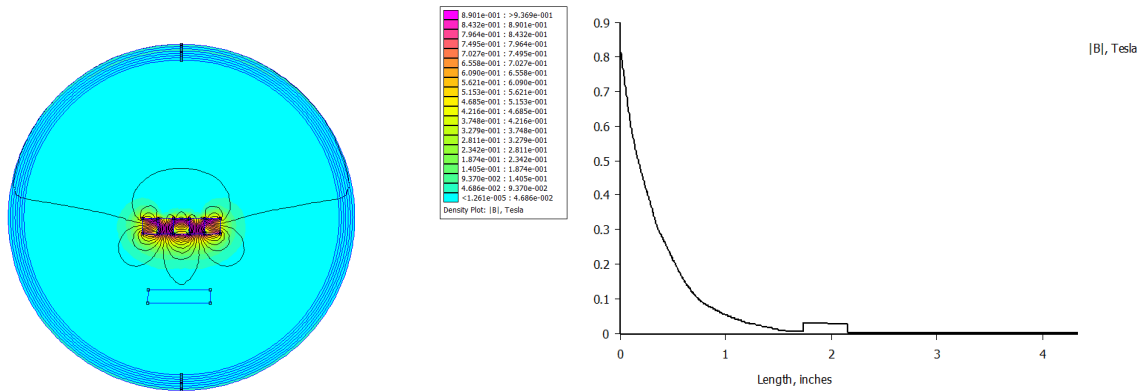


Figure 44: Halbach Array Flux Density Plots

Analyzing the plots in Figure 44, the maximum $|B|$ value is approximately equal to 0.05 Tesla. The change in flux density reading is approximately 0.04 T, which is 0.13 T less than the maximum change seen with the dual magnet array.

3.5.3 Discussion

The mathematical analysis in Sections 3.1 and 3.2 and the FEA comparison simulations in Section 3.3 quantify the magnetic field of the dual rotating magnet and Halbach array. The results verify the accuracy of both analyses. It is proven in Section 3.5.1 that the polar opposite orientation for the dual magnet unit is the optimal alignment. Comparing the FEA results from Sections 3.4.4 and 3.4.5, the dual magnet unit is far more effective in locating subterranean ferromagnetic objects.

The results in Section 3.5 counter initial theories on how the two magnetic fields interact. Originally, using the image in Figure 45, the vector lines appear to add together between the two magnets. With further analysis the lines that splay farther away from the dipole are counteracting each other, leaving the magnetic field zero above and below the two magnets.

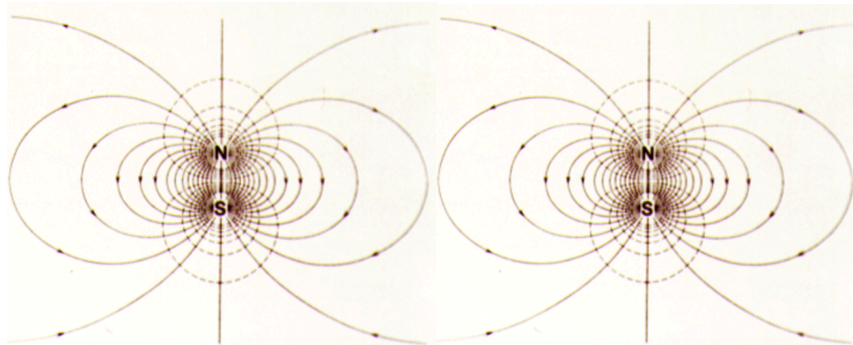


Figure 45: Magnetic Field of Two Adjacent Dipoles with Same Polar Orientation [28]

After changing the orientation of magnet 2 by 180 degrees, the field is canceled between the two magnets and added above and below the two magnets, as seen in Figure 46.

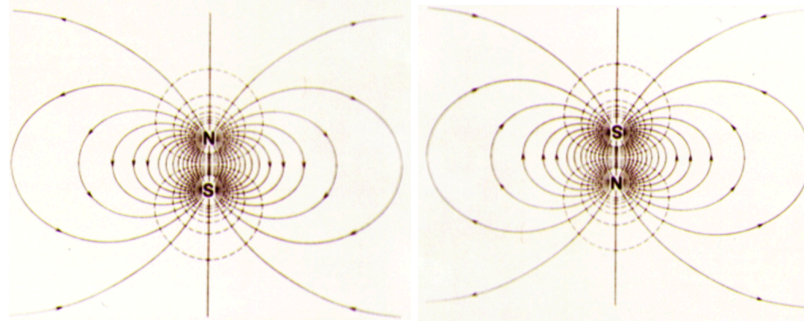


Figure 46: Magnetic Field of Two Adjacent Dipoles with Opposite Polar Orientation [28]

This analysis confirms that the orientation where magnet 1 is at 90° from 0° and magnet 2 is at 270° from 0° will work best for detecting ferrous objects. Further testing will be required to determine the optimal orientation to induce eddy currents. In order to induce eddy currents the rotation speed of the magnets must be increased to speeds above 1,000 rpm. Additionally, initial testing proved that 9-inch spacing was optimal for sensing subsurface ferrous objects with an aligned polar orientation. The FEA simulations determined 3-inch spacing is optimal for the polar opposite alignment.

Chapter 4: Equipment Design

Chapter 4 explains the different proposed and prototyped designs tested for the magnetic sensing device. Numerous designs were taken into consideration, and four designs were built and tested. The final design requirements and the chosen components are explained in detail.

4.1 Proposed Designs

4.1.1 Dual Rotating Magnet Unit

The SolidWorks model presented in Figure 47 is the proposed design for rotating two diametrically magnetized magnets in synchronization. Each motor labeled in Figure 47 has a diametrically magnetized 1” by 0.5” diameter rare earth magnet attached to the shaft. A Galil motion controller uses shaft rotation angle information from an encoder with multi-axis feedback control to ensure the two magnets rotate in perfect synchronization. There are two magnetometers in the design, both labeled in Figure 47. The lower magnetometer reads the magnetic field without an induced field from the two spinning magnets. The upper magnetometer reads the magnetic field induced by the spinning magnets. The two magnetic field readings from the magnetometers will allow them to be subtracted from one another to possibly enhance the sensitivity of the unit.

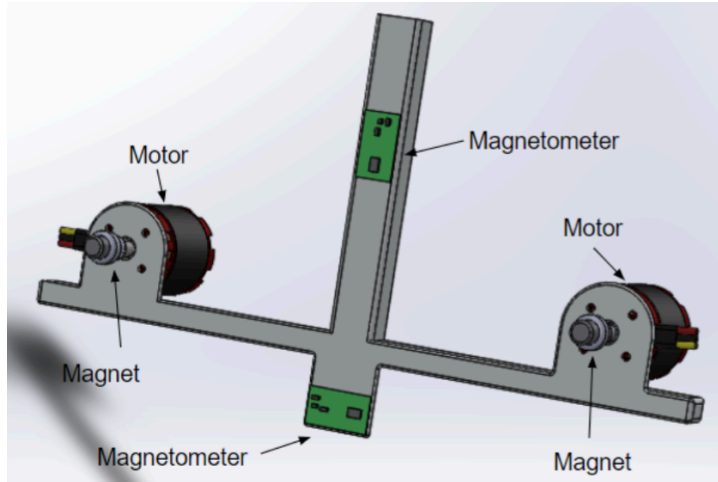


Figure 47: SolidWorks Model of Dual Rotating Unit

4.1.2. Spinning Halbach Array Unit

The SolidWorks model presented in Figure 48 is the proposed design for rotating a complete Halbach array. The magnet holder (labeled) has five 0.5” by 0.5” in rare earth cube magnets inside, in a specific polar orientation, to create a Halbach array.

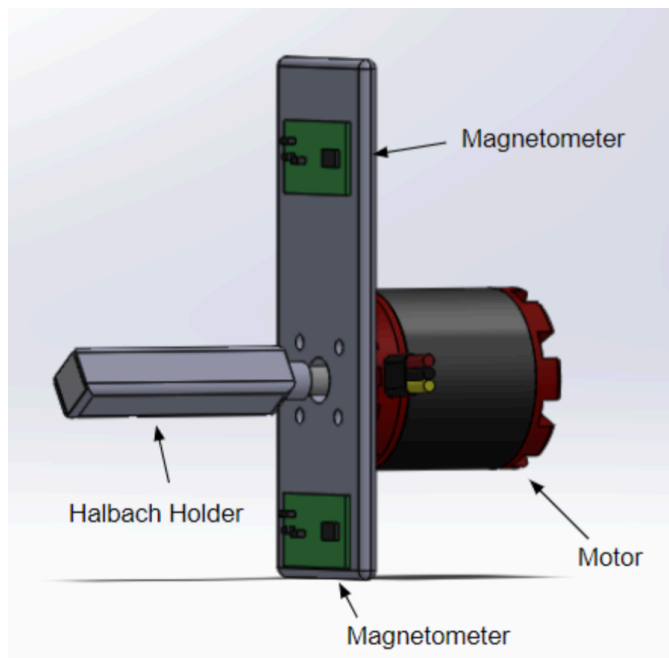


Figure 48: SolidWorks Model of Spinning Halbach Unit

There are two magnetometers in the design, which are both labeled in Figure 48. The lower magnetometer will read the magnetic field without an induced field from the Halbach array. The upper magnetometer will read the magnetic field induced by the Halbach array. The two magnetic field readings from the magnetometers will allow them to be subtracted from one another to possibly enhance the sensitivity of the unit.

4.1.3 Spinning Halbach Array with Two Degrees of Freedom

The SolidWorks model presented in Figure 49 is the proposed design for rotating two out of five magnets in a Halbach array. The gears spin magnets 2 and 4 (labeled in Figure 49) in opposite directions, creating an oscillating magnetic field. The augmented and canceled side of the Halbach array rotate each time the magnets spin 180 degrees, which forms a rotating oscillating magnetic field.

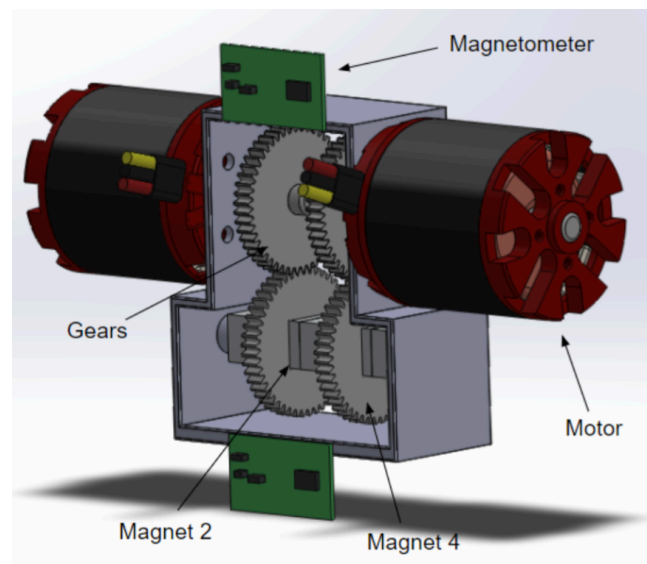


Figure 49: SolidWorks Model of Spinning Halbach Unit with 2 Degrees of Freedom

There are two magnetometers in the design, which are both labeled in Figure 48. The lower magnetometer will read the magnetic field without an induced field from the

Halbach array. The upper magnetometer will read the magnetic field induced by the Halbach array. The two magnetic field readings from the magnetometers will then be subtracted from one another to enhance the sensitivity of the unit.

4.1.4 Spinning Halbach Array with Five Degrees of Freedom

The SolidWorks model presented in Figure 50 is the proposed design for rotating all five magnets in a Halbach array. Each magnet in the array is spun by an individual motor. By spinning all five magnets in a synchronized manner, an oscillating magnetic field will be created. Each time the magnets spin 180 degrees, a Halbach array will create opposite polarization forming an oscillating magnetic field.

There are two magnetometers in the design, the lower magnetometer reads the magnetic field without an induced field from the Halbach array. The upper magnetometer reads the magnetic field induced by the Halbach array.

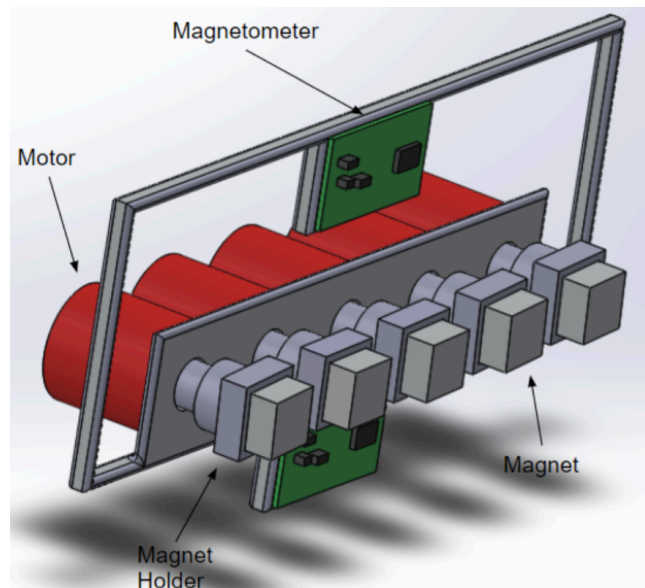


Figure 50: SolidWorks Model of Spinning Halbach Unit With 5 Degrees of Freedom

4.2 Preliminary Designs

Multiple iterations of the dual magnet system have been constructed. Iterations 1 and 2 used gearing to mechanically couple the two magnets.

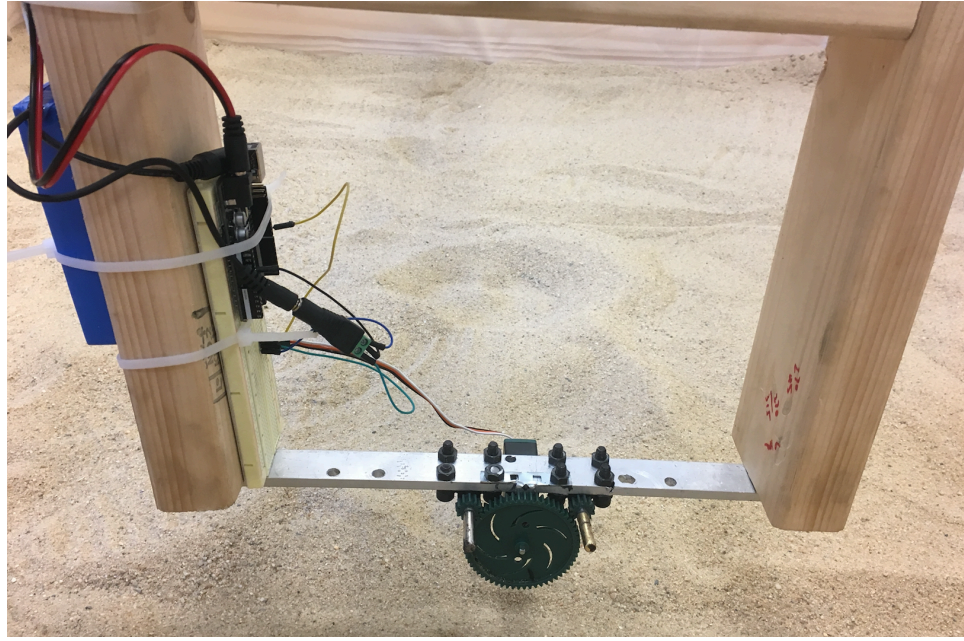


Figure 51: First Iteration

The first iteration used $\frac{1}{4}$ "D x 1"L diametrically polarized magnets, a Vex servo motor and Vex gearing, and motor speed was controlled by an Arduino Uno. A main 60 tooth drive gear is attached to the motor shaft which spins two 12 tooth gears. The smaller pinion gears are attached to the shafts that spin the magnets. The gear ratio is 5:1, meaning the small gear turns 5 times per one revolution of the larger gear. This design, although functional, had inherent disadvantages. The first limitation was the speed of the motor. The Vex servo motor can only spin at maximum speed of 1.67 Hz, according to the data sheet, but the actual speed was closer to 1 Hz. With the 5:1 gear ratio the magnets were

only spinning at 5 Hz, which is not fast enough to induce eddy currents. An additional limitation was that the magnets did not spin smoothly due to the poor alignment of the gears and lack of bearings in the pillow blocks.

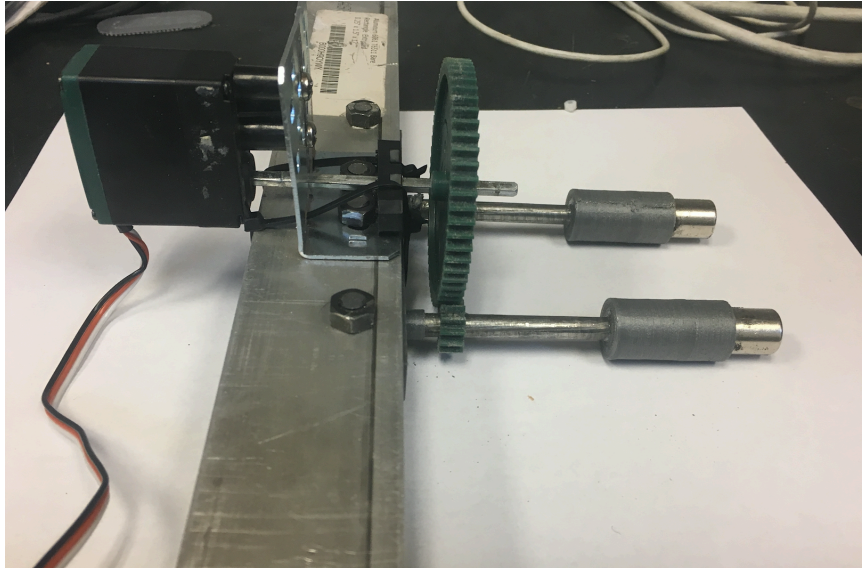


Figure 52: Second Iteration

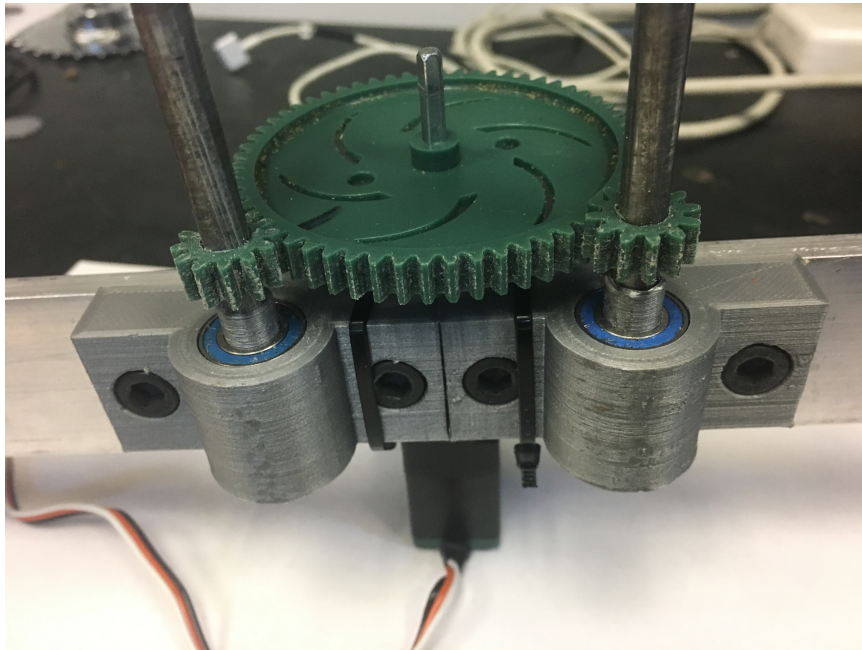


Figure 53: Second Iteration

The second iteration was built to solve the alignment issue of the first design. The design used a Vex servo motor and stronger $\frac{1}{2}$ "D x 1"L diametrically polarized magnets. Pillow blocks were printed using a ANet A8 3D printer and then bearings were pressed into the pillow blocks. Longer shafts extended the magnets in front of the motor and gear assembly. The design change solved the alignment issue, but other issues arose. The stronger magnets only being separated by 2 inches made the field interaction over powering and were unable to successfully sense subsurface objects. Additionally, the motor speed was still not adequate for sensing non-ferromagnetic objects.

Electronic gearing is necessary in order to achieve higher speeds. Spinning two electronically coupled motors at the same speed will allow speeds to exceed 10,000 rpm. Initial steps were taken to electronically gear two 180 degree Hi-Tec servo motors. The design was successful; a photograph is included in Figure 54.

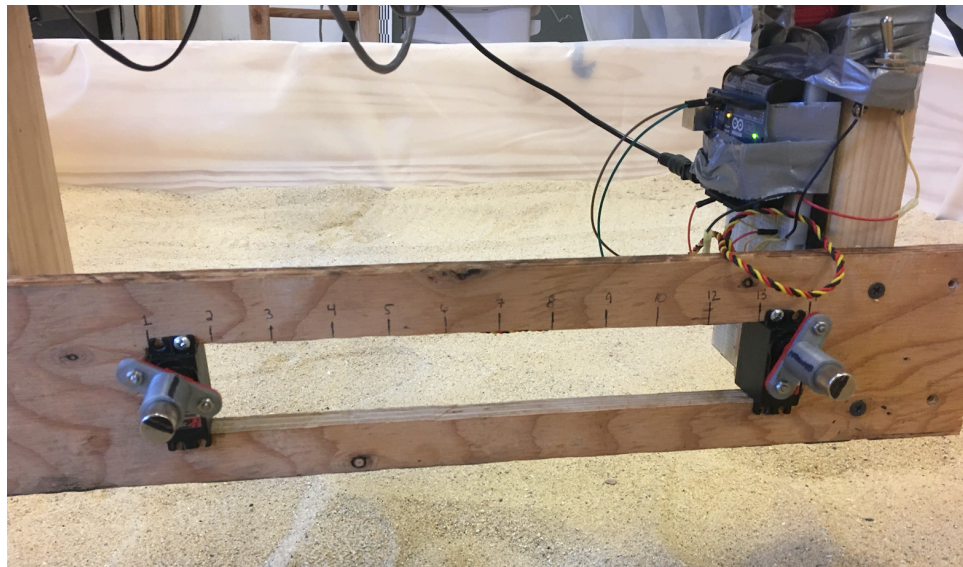


Figure 54: Iteration 3

The Hi-Tec servo motors have an incremental encoder built into the motor that relays shaft position back to the Arduino. Accurate updates about shaft position allows the Arduino to regulate the voltage, which controls the speed and maintains synchronization between the motors. The mounting of the motor was such that the distance between the motors could be adjusted to determine the optimal spacing for maximum sensing sensitivity. A disadvantage of the unit were the motors were limited to spinning at 180 degrees. Steps were taken to modify the motors to allow the motor shaft to spin 360 degrees. When this happened, they were unable to maintain synchronization, because the encoder was not set up for complete rotation. An additional limitation was the speed of the motor, the Hi-Tec motor maximum speed is approximately 1 Hz.

4.3 Final Design

Using advantages and disadvantages of the first three designs, the final design had to meet the following requirements.

- 1) Maintain synchronization of motors through electronic gearing
- 2) Motors must be capable of spinning at speeds of 10,000 rpm or 166.67 Hz
- 3) Entire unit must be stable at high speeds

In order to ensure the design would meet requirements before purchasing the parts, steps were taken to determine the correct motor size, magnetometer sampling rate, and motion controller for electronic gearing. The next section gives a detailed explanation of why each of the components are chosen.

4.3.1 Motor Sizing

The Faulhaber brushless DC servo motors offered a compact affordable solution. The following steps were taken to determine the correct Faulhaber motor for the dual magnet application. This is a low torque application. The motor specifications exceeded the necessary torque rating, which the following calculation confirmed.

According to Micromo, the Faulhaber distributor, the largest torque load occurs when the motors initially begin to rotate [17]. At that moment the torque from the magnet is equal to:

$$T_{magnet} = \frac{F_B D}{2} \quad (79)$$

Where F_B = Force when the shaft begins to rotate and D = Diameter.

Solving the torque equation:

$$F_B = 0.030kg * 9.81 \frac{m}{s^2} = 0.2943 N \quad D = 0.0127 m \quad (80)$$

$$T_{magnet} = \frac{(0.2943 N)(0.0127m)}{2} = 0.0019 N \cdot m = 1.9 mNm \quad (90)$$

$$T_{TOT} = T_{magnet} + T_{friction} = 1.9 mNm + 1.3 mNm = \mathbf{3.2 mNm} \quad (91)$$

Series 3242 ... BX4								
Values at 22°C and nominal voltage	3242 G	012 BX4	018 BX4	024 BX4	036 BX4	042 BX4	048 BX4	
1 Nominal voltage	U_N	12	18	24	36	42	48	V
2 Terminal resistance, phase-phase	R	0,92	2,01	3,67	8,96	11,7	15,1	Ω
3 Efficiency, max.	η_{max}	78	78	78	77	78	78	%
4 No-load speed	n_0	5 600	5 500	5 600	5 500	5 500	5 500	min ⁻¹
5 No-load current, typ. (with shaft \varnothing 5 mm)	I_0	0,179	0,117	0,089	0,059	0,05	0,044	A
6 Stall torque	M_H	268,7	280	269,4	251	262	265	mNm
7 Friction torque, static	C_0	1,3	1,3	1,3	1,3	1,3	1,3	mNm
8 Friction torque, dynamic	C_V	4,1·10 ⁻⁴	4,1·10 ⁻⁴	4,1·10 ⁻⁴	4,1·10 ⁻⁴	4,1·10 ⁻⁴	4,1·10 ⁻⁴	mNm/min ⁻¹
9 Speed constant	k_n	461	304	231	152	130	114	min ⁻¹ /V
10 Back-EMF constant	k_E	2,168	3,285	4,335	6,571	7,666	8,762	mV/min ⁻¹
11 Torque constant	k_M	20,7	31,4	41,4	62,8	73,1	83,7	mNm/A
12 Current constant	k_I	0,048	0,032	0,024	0,016	0,014	0,012	A/mNm
13 Slope of n-M curve	$\Delta n / \Delta M$	20,5	19,5	20,4	21,7	20,8	20,6	min ⁻¹ /mNm
14 Terminal inductance, phase-phase	L	60	132	240	529	719	940	μ H
15 Mechanical time constant	τ_m	6,4	6,1	6,4	6,8	6,5	6,5	ms
16 Rotor inertia	J	30	30	30	30	30	30	gcm ²
17 Angular acceleration	α_{max}	90	93,2	90	83,6	87,2	88,3	·10 ³ rad/s ²
18 Thermal resistance	R_{th1} / R_{th2}	2,3 / 11,6						K/W
19 Thermal time constant	τ_{w1} / τ_{w2}	13 / 880						s
20 Operating temperature range:								
- motor		-40 ... +100						°C
- winding, max. permissible		+125						°C
21 Shaft bearings		ball bearings, preloaded						
22 Shaft load max.:								
- with shaft diameter		5						mm
- radial at 3 000 min ⁻¹ (5 mm from mounting flange)		50						N
- axial at 3 000 min ⁻¹ (push / pull)		5						N
- axial at standstill (push / pull)		50						N
23 Shaft play:								
- radial	\leq	0,015						mm
- axial	$=$	0						mm
24 Housing material		stainless steel						
25 Mass		179						g
26 Direction of rotation		electronically reversible						
27 Speed up to	n_{max}	17 000						min ⁻¹
28 Number of pole pairs		2						
29 Hall sensors		digital						
30 Magnet material		NdFeB						
Rated values for continuous operation								
31 Rated torque	M_N	41,8	43	41,8	40,7	41,6	41,8	mNm
32 Rated current (thermal limit)	I_N	2,43	1,64	1,21	0,78	0,68	0,6	A
33 Rated speed	n_N	4 600	4 580	4 600	4 480	4 520	4 530	min ⁻¹

Figure 55: Series 3242 Data Sheet [17]

Consulting the data sheet for the Faulhaber 3242G BLDC servo motors in Figure 55: Series 3242 Data Sheet, the torque rating is 41.8 mNm for the 024 BX4. The maximum 3.2 mNm torque load in the dual magnet application is well under the torque rating for the motor.

An additional design requirement is the maximum speed requirement. In order to induce eddy currents in non-ferrous subsurface objects, the magnets must spin at speeds above 10,000 rpm or 183.3 Hz. Using Figure 56, Figure 57, and Figure 58 from Micromo,

it is determined that the maximum speed is approximately 13,500 rpm for a low torque application [17].

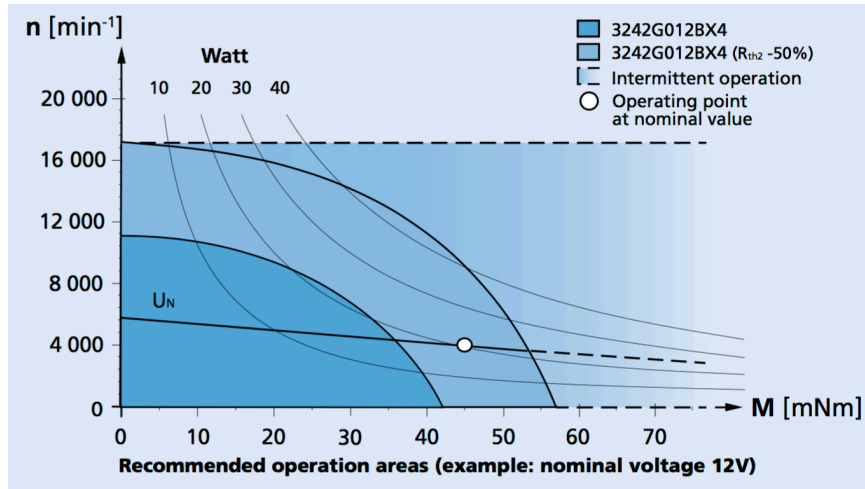


Figure 56: Recommended Operation Area [17]

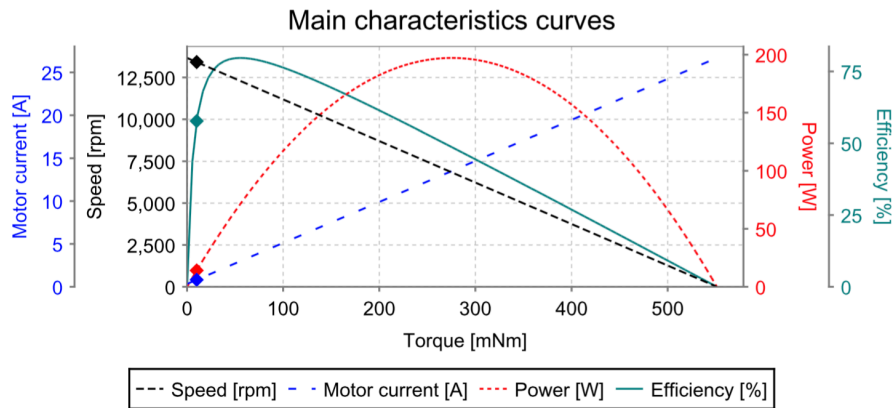


Figure 57: Main Characteristic Curves [17]

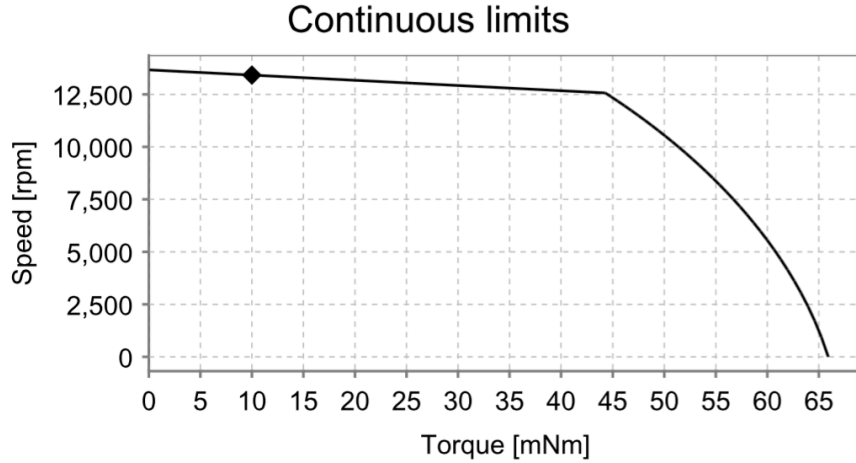


Figure 58: Speed vs. Torque [17]

To find the exact voltage requirement for the dual magnet application, the following equations outlined by Micromo are used [17]. In order to determine if the 3242G motor can spin at required speeds, the first step is to determine the current at the total torque calculated above.

$$I = \frac{T_{TOT}}{k_m} = \frac{3.2 \text{ mNm}}{41.4 \frac{\text{A}}{\text{mNm}}} = \mathbf{0.077 \text{ A}} \quad (92)$$

Where k_m = torque constant.

Next, to solve for the voltage required to spin the motors at speeds of 10,000 rpm:

$$V = I \cdot R + \omega \cdot 0.002168 \frac{\text{V}}{\text{rpm}} \quad (93)$$

Where I = current, R = resistance, ω = angular velocity.

$$V = 0.077 \text{ A} \cdot 3.67\Omega + 10000 \text{ rpm} \cdot 0.0002168 \frac{\text{V}}{\text{rpm}} = \mathbf{21.96 \text{ V}} \quad (94)$$

The 21.96 voltage requirement is well within the capabilities of the 3242G024BX4 motor. Using the following equation determines the maximum speed at 30V.

$$\omega = \frac{V - I \cdot R}{0.002168 \frac{V}{rpm}} = \frac{30V - 0.077 A \cdot 3.67\Omega}{0.002168 \frac{V}{rpm}} = 13707 rpm \quad (95)$$

The maximum speed is solved at 13,707 rpm, confirming that the Faulhaber 3242G BLDC servo motor to be a good choice for the application.

4.3.2 Magnetometer

PNI Sensor Corporation specializes in geomagnetic sensors. The PNI RM3100 sensor meets the sensitivity, sample rate, and size requirements of the magnetic sensing device.

The PNI RM3100 is a highly sensitive, compact, and cost-effective 3 axis geomagnetic sensor. The unit provides high resolution, high sampling rates, low power consumption, large signal noise immunity, and a large dynamic range [33]. The PNI test board communicates with the RM3100 through either a I²C or SPI bus and then using the PNI Communication Board, a USB connection to any PC computer is created. A communication board using open source RealTerm software, provides board control and measurement results.

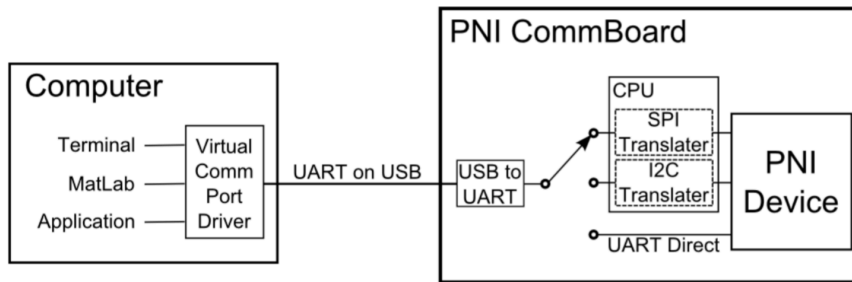


Figure 59: Communication Schematic [33]

The maximum sampling rate is 1,600 Hz with a 50-cycle count setting. For a 3-axis measurement reading, the maximum sampling rate is 533.33 Hz at 50 cycle counts. According to the Nyquist-Shannon sampling theory, the sampling rate needs to be a minimum of twice the signal frequency [31]. This is because a minimum of two samples per wave form are needed to capture the signal, one sample for both the positive and negative frequencies [31]. For the dual rotating magnet application, the required minimum sampling rate is then 333.33 Hz when the motors are spinning at 10,000 rpm.

Parameter	Cycle Counts ²			Units
	50	100	200	
Field Measurement Range ³	-800 to +800			μT
Gain	20	38	75	LSB/μT
Sensitivity	50	26	13	nT
Noise	30	20	15	nT
Noise Density @ Max. Single-Axis Sample Rate	1.2			nT/Hz
Repeatability over ±200 μT	15	8	8	nT
Hysteresis over ±200 μT	15			nT
Linearity over ±200 μT	0.5			%
Maximum Single-Axis Sample Rate (divide by 3 for max. 3-axis sample rate)	1600	850	440	Hz
Single-Axis Average Current @ 24 Hz Sample Rate (equivalent to 3-axis @ 8 Hz)	70	135	260	μA
Bias Resistor, R _b	121			Ω
External Timing Resistor for Clock, R _{EXT}	33			kΩ
Circuit Oscillation Frequency	180			kHz
Operating Temperature	-40 to +85			C

Figure 60: RM3100 Data Sheet [33]

The RM3100 can be set in either single or continuous measurement mode. In continuous measurement mode the board continuously measures the magnetic field in 3-dimensions and records the measurement after every reading.

Each sensor is an inductive element in a LR relaxation oscillation circuit. The magnetic field is proportional to the inductance in the coil that is parallel to the sensor axis and is driven by the MagI²C ASIC. The geomagnetic RM3100 sensor works in the frequency domain and the oscillation frequency of the circuit is measured by the MagI²C's internal clock. Working in the frequency domain allows the resolution and noise to be established cleanly by the number of internal clock counts.

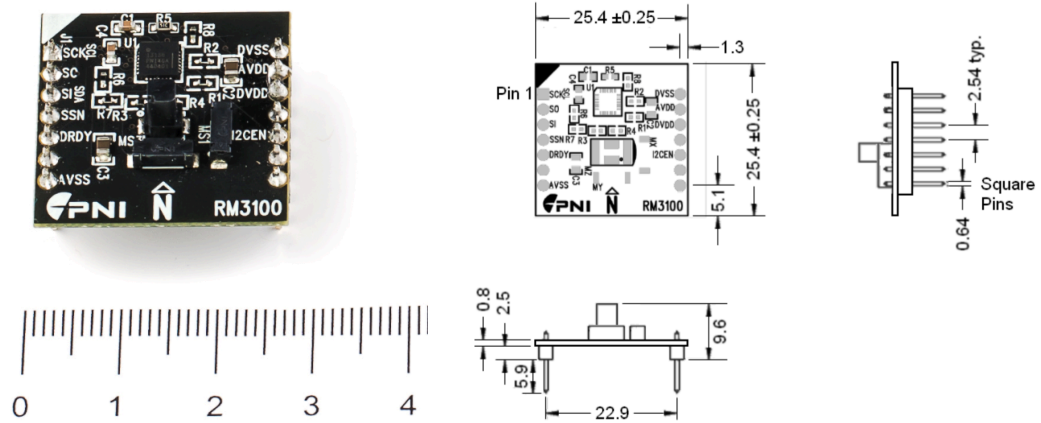


Figure 61: RM3100 Sensor Schematic [33]

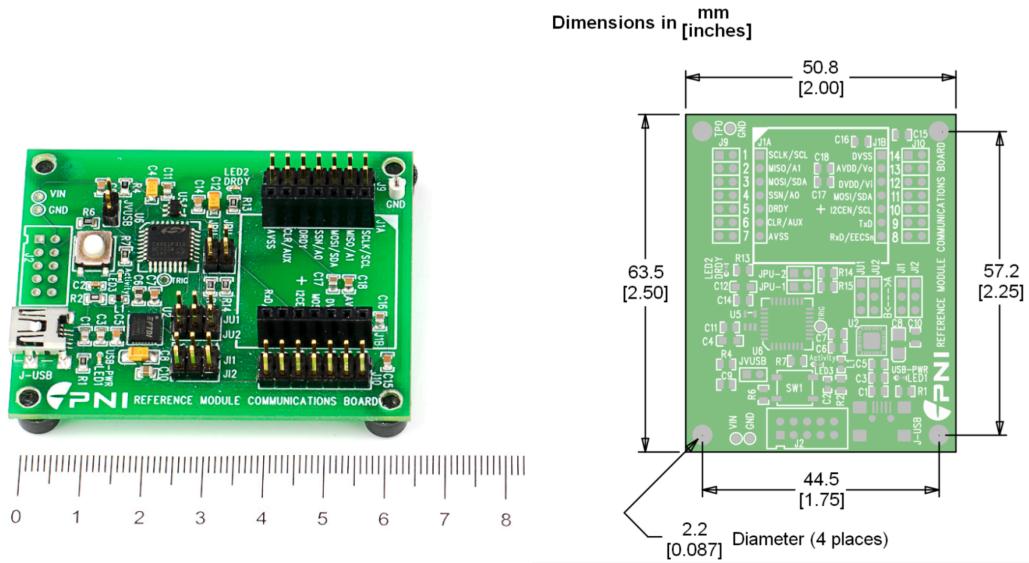


Figure 62: Communication Board Schematic [32]

Using the communication board simplifies the setup. The RM3100 testing board pins right into the board. Depending on the communication bus being used (I²C or SPI) the polarity and jumper orientation will change on the communication board. I²C communication is used in this project using the board setup seen in Figure 63.

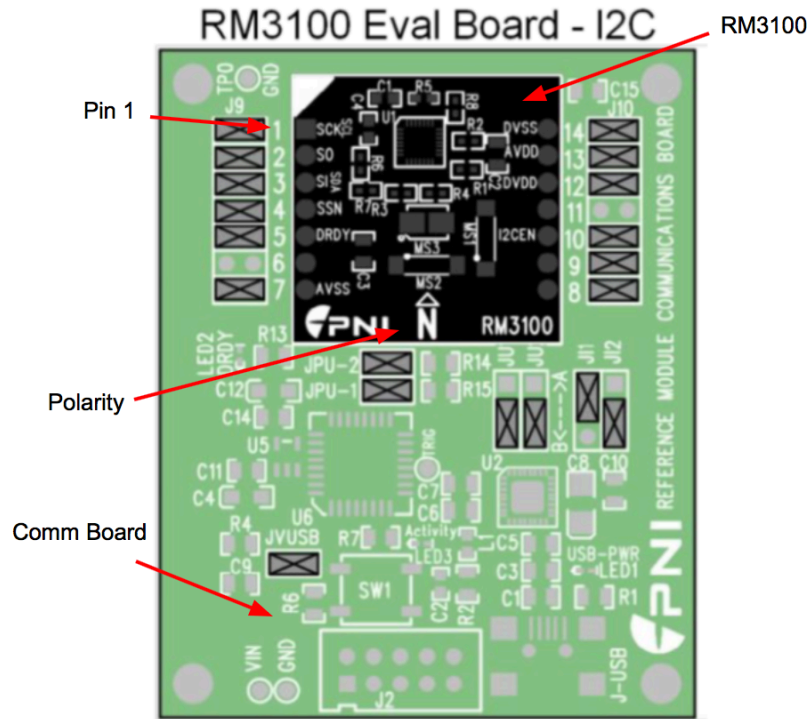


Figure 63: Communication and Evaluation Boards [32]

As seen in Figure 63 the green represents the communication board and the black represents the RM3100 sensor. The polarity of the sensor aligns in the direction of the *N* (labeled in Figure 63). There are 14 pins on the sensor. Pin 1 is labeled in Figure 63. Each pin has the title seen in Table 3.

Table 3: Magnetometer Pin Assignments [32]

Pin Number	Pin Name	Description
1	SCL	Serial Clock Line
2	SA1	Bit 1 of slave address
3	SDA	Serial Data Line
4	SA0	Bit 0 of slave address
5	DRDY	Status line
6	NC	No connection
7	AVSS	Ground pin for analog section of ASIC
8	NC	No connection
9	NC	No connection
10	I2CEN	I ² C enable pin
11	NC	No connection
12	DVDD	Supply voltage for digital section of ASIC
13	AVDD	Supply voltage for analog section of ASIC
14	DVSS	Ground pin for digital section ASIC

Using RealTerm software, the commands are sent to the RM3100 sensors. RealTerm communicates with the board using ASCII. A simple one-line command sets the sensors in continuous measurement mode. The code for continuous measurement is [46 01 71]. To read the measurement another one-line code is sent {46 24 09}. There are two ways to store a measurement result. 1) Every time a measurement is needed, send the {46 24 09} command to the board using the Send ASCII button in Figure 65; and 2) using the dump file to port option, create a text file that has the appropriate commands and upload it to RealTerm.

```
capture - Notepad
File Edit Format View Help
[46 01 71]
{46 24 09}
|
```

Figure 64: ASCII Text File

The repeat option can set the number of times the sensors takes a measurement. RealTerm continuously sends the commands in the text file to the board, allocated by the number of times specified in the repeat tab.

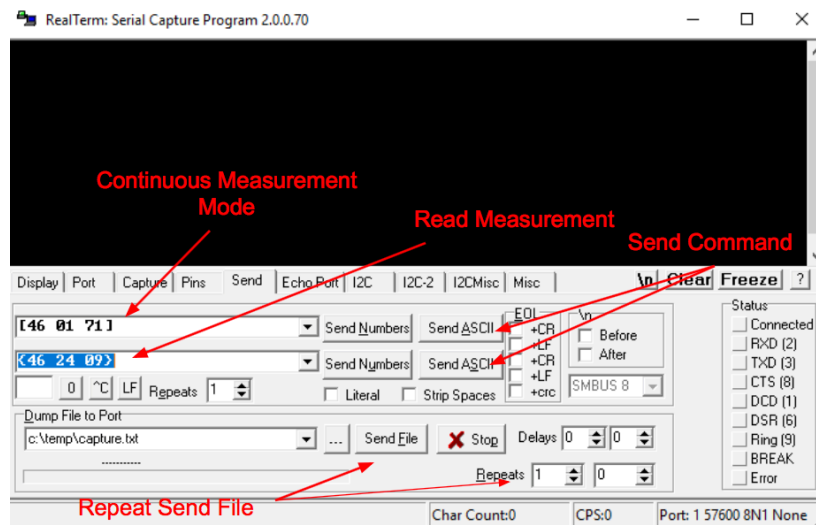


Figure 65: RealTerm Serial Capture Program

Data are saved to a text file using the capture tab. Using the Start Overwrite button, seen in Figure 66, a user can create a new file in a specified folder and save the sensor readings until a Stop Overwrite is initiated.

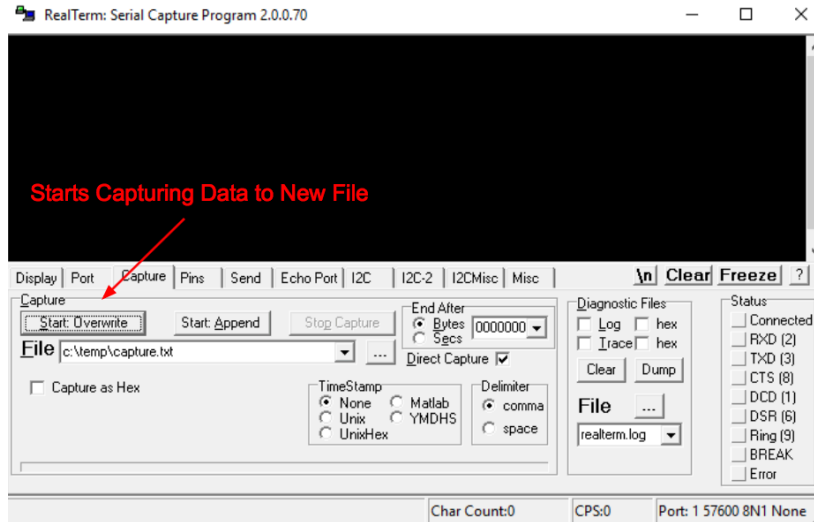


Figure 66: RealTerm Serial Capture Program

Each RM3100 sensor reading has 3 bytes of data and stores it in the form of 2's complement, therefore each 3-axis measurement has a total of 9 bytes of data. The string of data is saved to the text file that has a $L_F C_R$ after each measurement. $L_F C_R$ is interpreted as a new line command when read by an external source. In a text file $L_F C_R$ is not present, but when reading the text file with Excel or Matlab. Figure 67 depicts a typical formatted string of data.

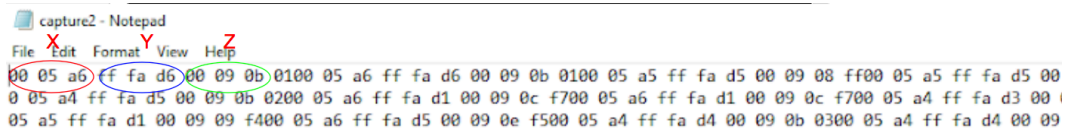


Figure 67: Data Format

Using a Matlab script (see Appendix A) the data are converted from 2's complement to an integer value in a range from -8388608 to 8388607. The integer value is then converted from voltage to micro Tesla's. The 2's complement is a common way to

represent signed integers in binary. The following function converts from hex representation of 2's complement to a decimal number

```
function [x]=nhex2dec(hexstring,n)
% hexstring : hex representation of two's complement of xmydec=
hex2dec(hexstring);
% x : input decimal number
% n : number of bits to perform 2's complements
x = hex2dec(hexstring);
x = x - (x >= 2.^(n-1)).*2.^n;
```

The script below takes the data and reformats it into a 3 x 981 array and then calls the nhex2dec function to convert the sensor data to decimal values. To convert from voltage to micro Teslas, the decimal number is divided by the range (8388607) and then multiplied by 3 volts (average voltage applied).

```
A = table2array(TEST1); %Converts from table to array
X=linspace(0,1141,1141); %Creates x vector
D= nhex2dec(A,24); %Calls function nhex2dec and converts from hex to
dec
F=(D/8388607)*3; %Converts from voltage to micro Tesla's
plot(X,F(:,1)); %Plots x values
plot(X,F(:,2)); %Plots y values
plot(X,F(:,3)); %Plots z values
```

4.3.3 Motion Control and Electronic Gearing

A Galil DMC-4123 motion controller was chosen to operate the Faulhaber motors. The simplistic design and relatively affordable platform made it the correct choice for the spinning magnet application. The Galil controller can control up to four axes independently and can operate in a voltage range from 20-40V [36]. The details on how the Galil controller operates are explained below.

4.3.2.1 Motion Controller

The Galil motion controller has three main functional elements: 1) microcomputer, 2) communication, and 3) motor interface. The microcomputer is the main processing unit of the controller. The microcomputer contains RAM to store variables, array elements, and application programs. Additionally, it contains Flash EEPROM, which provides non-volatile storage of variables and arrays, as well as the firmware for the controller. The communication with Galil Suite occurs through a high speed 100bT Ethernet connection. Using Galil's GL-1800 custom sub-micron gate array, decoding of the quadrature signal from each encoder is possible at speeds up to 15 MHz. The controller generates a 10V analog signal [36].

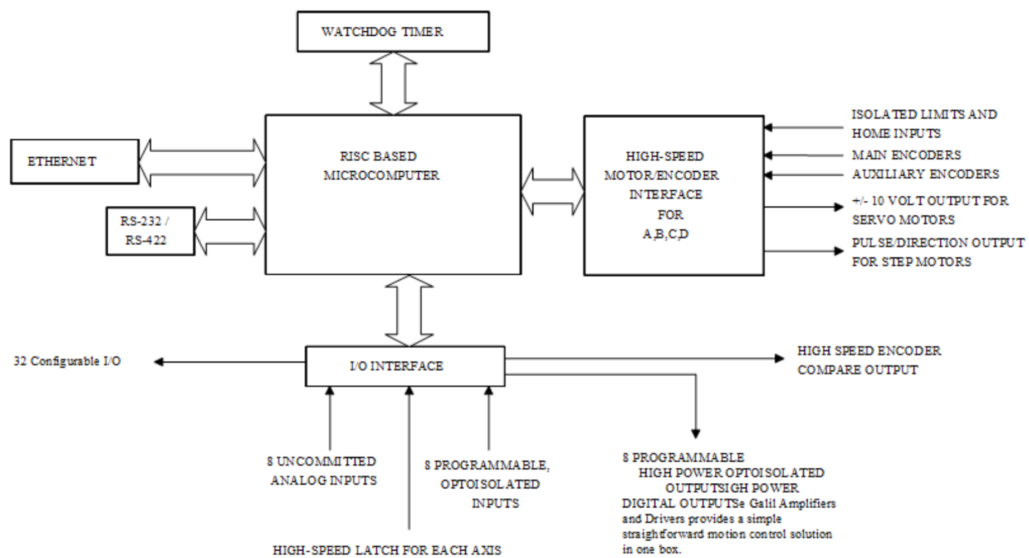


Figure 68: Motion Controller Schematic [36]

The system elements seen in Figure 68 include: 1) motor, 2) amplifier, 3) encoder, and 4) power supply. The motor and encoder were explained above. The amplifier takes

the voltage signal from the controller and converts it into a current to drive the motor. The amplifier size depends on the power requirements of the motor, the DMC 41X3 Galil controller in this application has a D3640 internal amplifier.

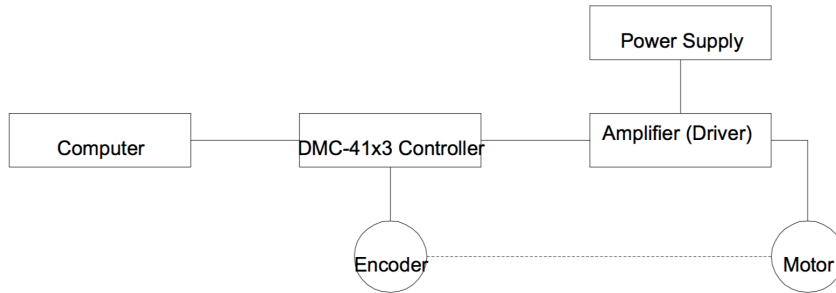


Figure 69: Simplified Schematic [36]

Communication between the controller and the encoder is through a female 26-pin D-sub connector and a four-circuit dual row power connector. The motors are wired into a male D-sub connector and power connector as follows.

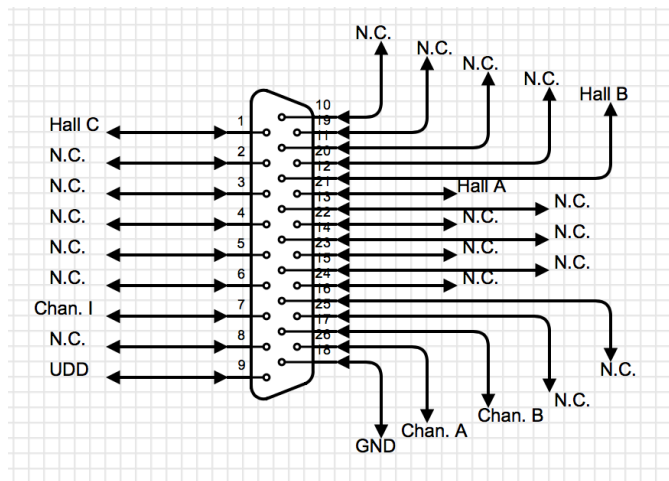


Figure 70: 26 Pin D-Sub Connector Wiring Diagram

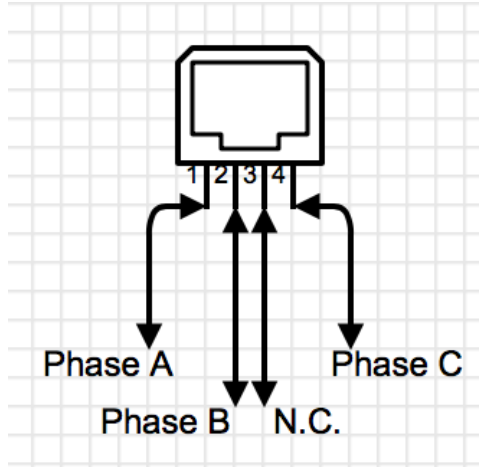


Figure 71: Motor Power Connector Wiring Diagram

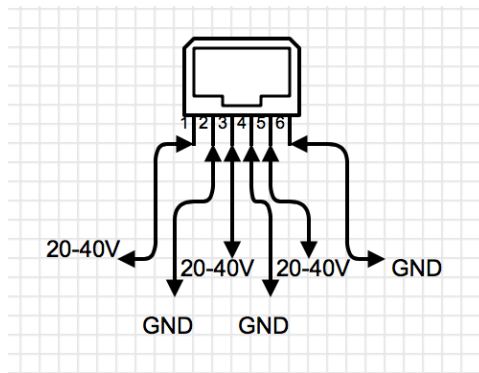


Figure 72: Controller Power Wiring Diagram

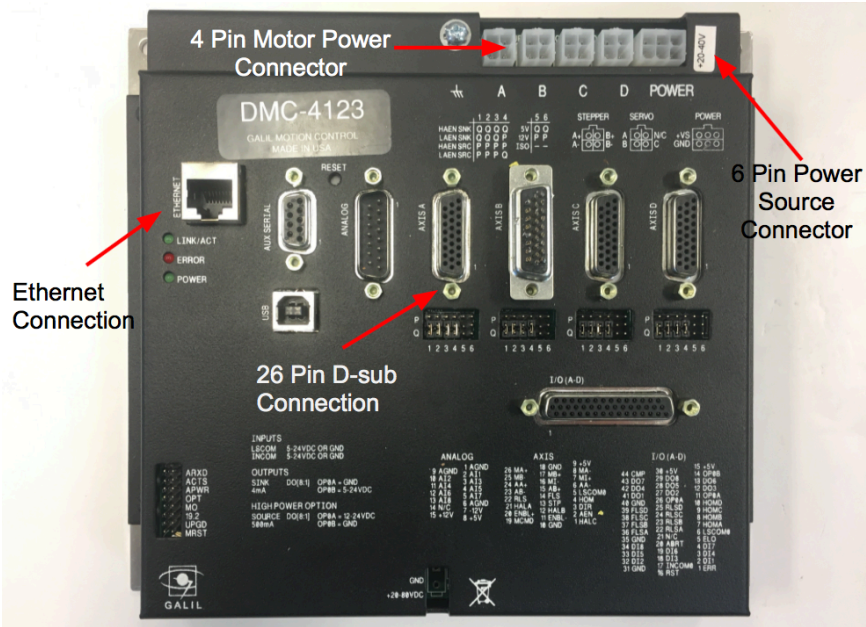


Figure 73: Galil DMC-4123 Controller

An isolated 30V power supply powers the Galil controller. Using Galil’s own graphical user interface called Galil Suite, code can then be sent directly to the controller to initiate the motors and commence electronic gearing movement. First, code is sent to the controller to initialize the motors. The initialization process sets the polarity of the encoders and then moves the motors back and forth to understand the current position and ensure encoder feedback is present. For further details about the code, see the line by line code explained in Figure 74.

```

0 CEA=2;' configure a axis encoder polarity
1 CEB=2;' configure b axis encoder polarity
2 BAA;' brushless a axis
3 BMA=1024;' brushless modulus a axis
4 BZA=3;' brushless zero a axis (initialize)
5 WT250;' wait 250 msec
6 BAB;' brushless b axis
7 BMB=1024;' brushless modulus b axis
8 BZB=3;' brushless zero b axis (initialize)
9 WT250;' wait 250 msec

```

Figure 74: Initialization Code

The second set of code sets the motors in gantry mode(GM), which is a preprogrammed application in Galil Suite that electronically gears the two motors. In gantry mode the axis A motor is set as the master and the axis B motor is set as the slave motor. By setting the gear ratio 1:1 the two motors will spin in unison. Using the jog command (JG) the speed of the two motors can be adjusted. A higher number, corresponds to faster shaft rotation speed. For a more detailed code description, read the in-line comments of the code in Figure 75.

```

0 GA,A;' a axis gearing master, b axis gearing slave
1 GR,1;' b axis gear ratio 1:1
2 GM,1;' gantry mode enabled
3 JG100000;' set speed jog
4 SHAB;' enable both axes
5 BGA;' begin jog

```

Figure 75: Gantry Mode Code

4.3.3.2 Electronic Gearing

The main objective of the motion controller is to enable electronic gearing between the two motors. In order to spin the two motors at speeds above 10,000 rpm, electronic gearing is necessary. The high precision mechanical gearing needed to spin two magnets

at above 10,000 rpm is unattainable for the dual rotating magnet application. Electronic gearing in this application simplifies the design immensely. Electronic gearing uses a motion controller and motor encoder feedback to maintain synchronization between electric motors. This serves applications such as X-Y plotters, gantry systems, and robots [30]. In the simplest form, a slave axis is set to follow a master axis. The slave axis can have a programmatically set gear ratio with respect to the master axis. Each axis can be independently controlled using a graphical user interface (GUI) to communicate with each motor encoder.

There are two kinds of encoders on the market, absolute encoders and incremental encoders. An absolute encoder outputs exact position from the time they are switched on. The encoder wheel has a unique code that is read to determine the position of the shaft [30]. Incremental encoders output a signal each time the shaft rotates a certain amount [30]. The number of increments per 360 -degree rotation of the shaft determines the accuracy of the encoder. An incremental encoder outputs a pulse signal which can either be a single channel (A) that outputs one line of pulses or two channels (A and B) that outputs two lines of pulses. Channel A and B pulses are offset to determine the rotation, the phasing between the two signals is called quadrature. Oscillations that are 90 degrees out of phase of one another are considered in quadrature [30].

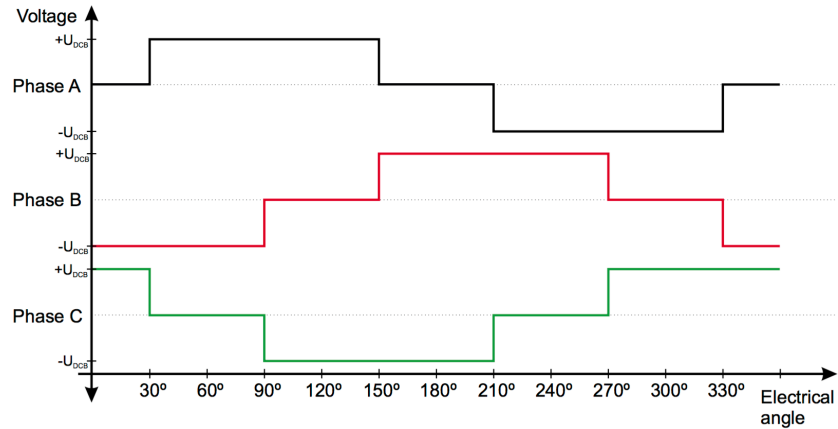


Figure 76: Quadrature Plot [30]

An additional indexing channel is found on some encoders, it is used for homing and pulse count verification on channels A and B, by providing one pulse per revolution. This signal is sent from the encoder to the motion controller, which sends voltage pulses through Hall sensors to the motor based on the encoder feedback [30]. A typical brushless direct current motor (BLDC) is driven by rectangular voltage strokes [30]. There is a rotor flux that is generated by the rotor magnet and interacts with the stator flux to define the speed and torque of the motor. In order to maximize torque of the motor, the angle between the rotor flux and stator flux must be close to 90° [30]. To maintain the 90° flux angle, the voltage strokes have to be accurately applied to two out of three phases of the motor. By energizing two motor phases concurrently there are six possible voltage vectors that are applied to the motor using Pulse Width Modulation (PWM) [30]. PWM works by using switches that open and close rapidly, controlling the voltage between the controller and the motor.

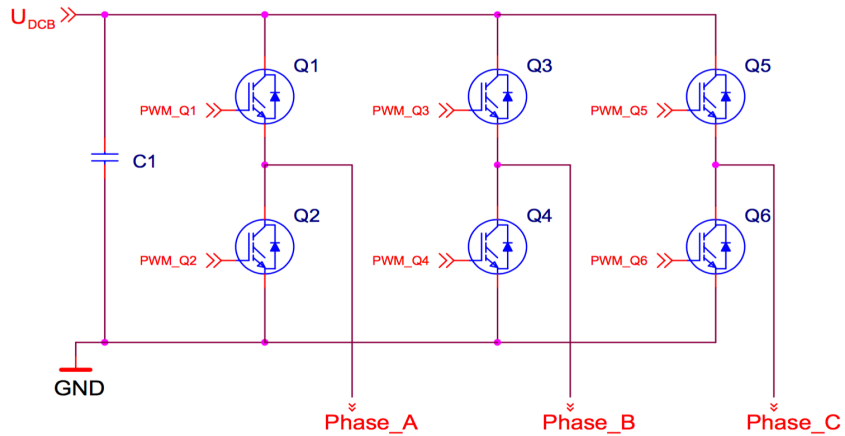


Figure 77: Phase Schematic [30]

Orientation change of the stator flux vector creates rotation. Hall sensors are embedded in the stator to tell the controller the relative position of the stator to the rotor, so it knows when to energize the windings in the motor. Hall sensors sense the rotor position, so the stator flux vector knows when to change. There are three sensors, each corresponds with a certain stator flux vector and generate a total of six states.

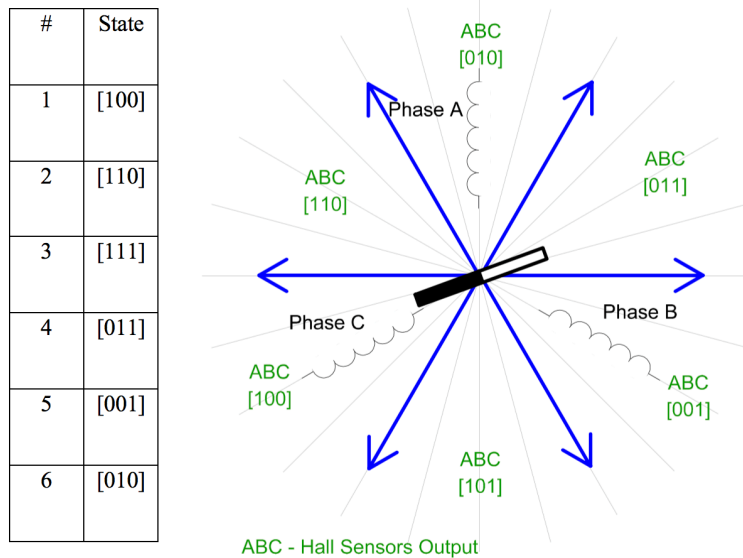


Figure 78: Representation of 6 Different States [24]

In order to continually control the motor speed, the Hall sensors state must change its value, as seen in Figure 78. The motor achieves this by applying a unique voltage pattern at different points in the rotation. This phenomenon allows for continuous high torque motion [30]. The speed of the motor depends on the amplitude of the applied voltage, which can be adjusted using the PWM technique explained earlier. The controller uses Proportional-Integral (PI) control to maintain the PWM pulses and therefore the voltage amplitude is adjusted to maintain the speed of the motor [30].

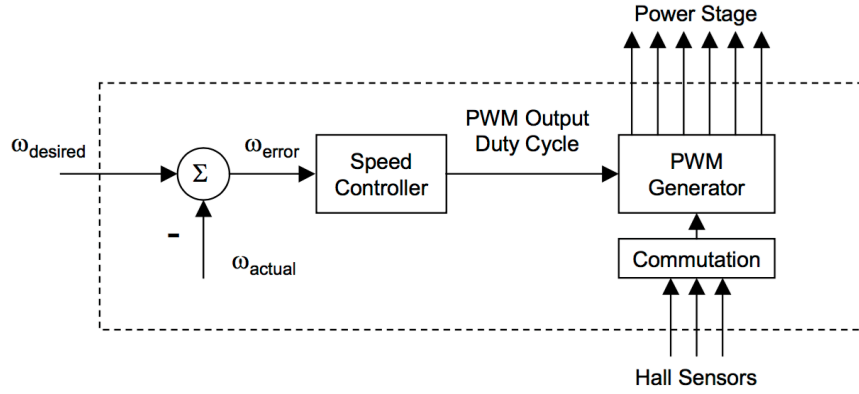


Figure 79: Pulse Width Modulation [24]

The controller calculates the PI algorithm explained in Brejl’s paper on BLDC motor control using the equations below [30]:

$$u(t) = K_c[e(t) + \frac{1}{T} \int_0^t e(\tau)d\tau] \quad (96)$$

Equation 96 is transformed into discrete time domain through an integral approximation. The following approximate equations were solved using the Backward Euler method.

$$u(k) = u_p(k) + u_i(k) \quad (81)$$

$$u_p(k) = K_c \cdot e(k) \quad (82)$$

$$u_I(k) = u_I(k - 1) + K_c \frac{T}{T_I} \cdot e(k) \quad (83)$$

Where $e(k)$ =input error in step k, $w(k)$ =Desired value in step k, $m(k)$ =Measure value in step k, $u(k)$ =Controller output in step k, $u_p(k)$ =Proportional output portion in step k, $u_I(k)$ =Integral output portion in step k, and $u_I(k - 1)$ =Integral output portion in step k-1, and T_I =Integral time constant.

To apply electronic gearing for the dual rotating magnet unit, the Faulhaber 3242G024BX4 BLDC servo motors were paired with an IE3-1024 encoder. The IE3-1024 is an incremental encoder with 1024 lines per revolution. It is a 3-channel encoder (A, B and I), that uses a 5V supply voltage. Channels A and B output a continuous 90° phase shifted square wave signal with 1024 impulses per revolution and channel I outputs one pulse per revolution. It can operate at a frequency range of up to 240 kHz. For additional encoder information see Figure 80 and Figure 81.

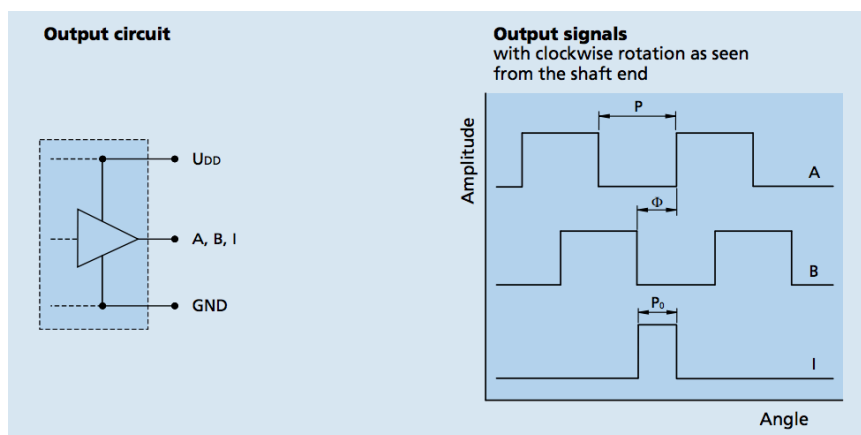


Figure 80: IE3-1024 Output Circuit and Signals [29]

Series IE3-1024		IE3-32	IE3-64	IE3-128	IE3-256	IE3-512	IE3-1024	
Lines per revolution	<i>N</i>	32	64	128	256	512	1 024	
Frequency range, up to ¹⁾	<i>f</i>	15	30	60	120	240	430	kHz
Signal output, square wave		2+1 Index						Channels
Supply voltage ²⁾	<i>U_{DD}</i>	4,5 ... 5,5						V
Current consumption, typical ³⁾	<i>I_{DD}</i>	typ. 20, max. 30						mA
Output current, max. ⁴⁾	<i>I_{OUT}</i>	4						mA
Index Pulse width ⁵⁾	<i>P₀</i>	90 ± 45						°e
Phase shift, channel A to B ⁵⁾	<i>Φ</i>	90 ± 45						°e
Signal rise/fall time, max. (<i>C_{LOAD}</i> = 50 pF)	<i>tr/tf</i>	0,1 / 0,1						µs
Inertia of sensor magnet	<i>J</i>	0,08						gcm ²
Operating temperature range		-40 ... +100						°C
Accuracy, typ.		0,5						°m
Repeatability, typ.		0,1						°m
Hysteresis		0,17						°m
Edge spacing, min.		421						ns
Mass, typ.		13,5						g
¹⁾ Velocity (min ⁻¹) = <i>f</i> (Hz) x 60/ <i>N</i> ²⁾ 3,0 ... 3,6 V optional available on request ³⁾ <i>U_{DD}</i> = 5 V; with unloaded outputs ⁴⁾ <i>U_{DD}</i> = 5 V; low logic level < 0,4 V, high logic level > 4,5 V; CMOS- and TTL compatible ⁵⁾ At 5 000 min ⁻¹								
For combination with Motor								
Dimensional drawing A		<L1 [mm]	Dimensional drawing C		<L1 [mm]	Dimensional drawing E		<L1 [mm]
2237 ... CXR	52,5	2444 ... B - K1838	55,3	3242 ... BX4	60,0			
2264 ... BP4	79,1	3056 ... B - K1838	67,3	3268 ... BX4	86,0			
3274 ... BP4	90,8	3564 ... B - K1838	75,3					
Dimensional drawing B		<L1 [mm]	4490 ... B - K1838	100,3	Dimensional drawing F		<L1 [mm]	
2342 ... CR	60,5	4490 ... B5 - K1838	100,3	3863 ... CR - 2016	82,6			
2642 ... CXR	60,5			3890 ... CR - 2016	108,6			
2642 ... CR	60,5	Dimensional drawing D		<L1 [mm]				
2657 ... CXR	75,5	2232 ... BX4	50,2					
2657 ... CR	75,5	2250 ... BX4	68,2					
2668 ... CR	86,5	2250 ... BX4 S	68,2					
3242 ... CR	60,5							
3257 ... CR	75,5							
3272 ... CR	90,5							

Figure 81: IE3 Series Encoder Data Sheet [29]

4.3.3.3 Electronic Gearing Test

In order to prove the two motors are truly rotating with the identical rate of rotation, an electronic gearing demonstration was conducted. The following equipment was used:

- 1) Newport optical bread board
- 2) Linear stage
- 3) Two Faulhaber 3242G024BX4 BLDC servo motors with IE3-1024 encoders
- 4) Two 50 tooth involute spur gears (3-D Printed)

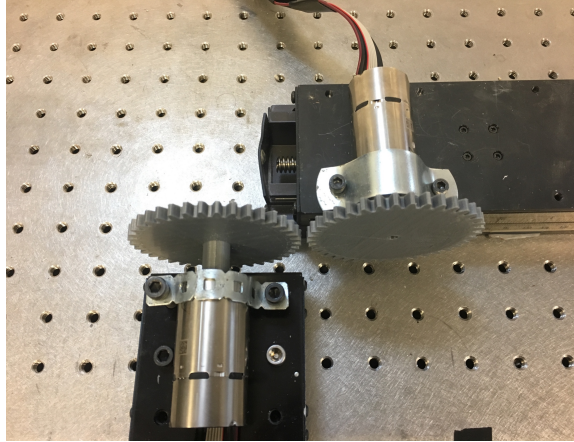


Figure 82: Electronic Gearing Test Close Up

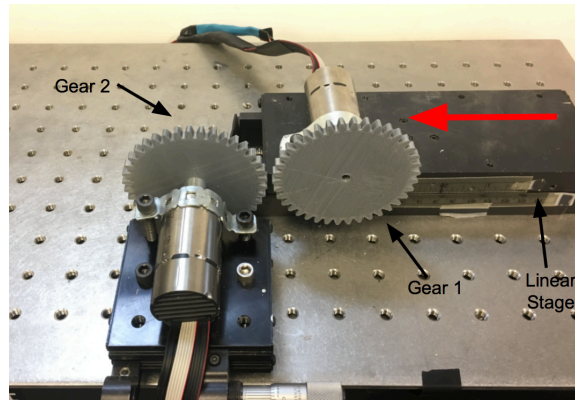


Figure 83: Labeled Electronic Gearing Test

The electronic gearing code was uploaded to the Galil controller and the two motors were set in a starting location where the gears lined up. Both motors were spun at approximately 4,000 rpm in the clockwise direction. Using the linear stage, gear 1 traveled in the direction of the red arrow seen in Figure 83 until the gears were meshed and then returned to the original position. This process was repeated, and the gears continued to stay aligned proving the electronic gearing was working properly.

4.3.4 Final Design

The final design used the following components:

- 1) 2 Faulhaber 3242G024BX4 BLDC Servo Motors
- 2) 2 PNI RM3100 Geomagnetic Sensors
- 3) 2 PNI Communication Boards
- 4) Lexan Shield
- 5) Motor Mount
- 6) Magnet Holder
- 7) Galil DMC-4123 Motion Controller
- 8) PC Computer Running Windows 7
- 9) 30 Volt Power Supply

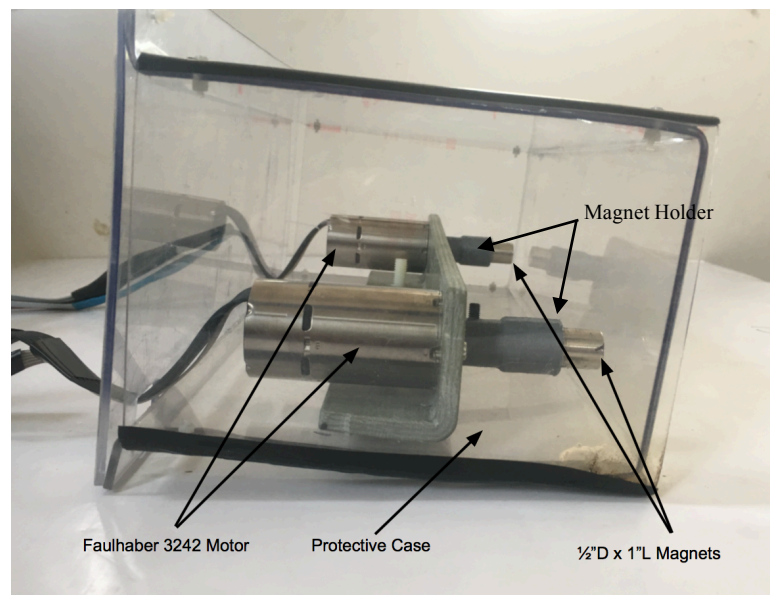


Figure 84: Close Up of the Designed Unit

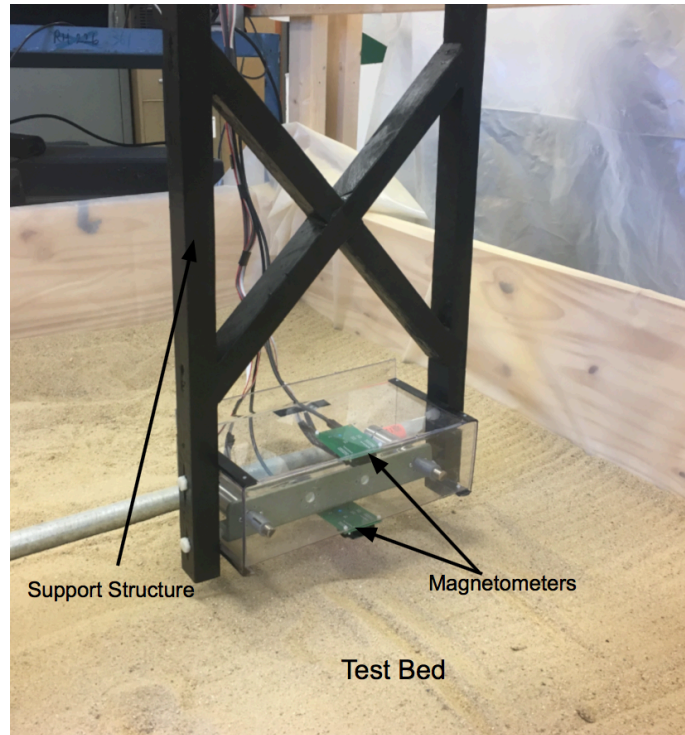


Figure 85: Unit Attached to Linear Drive in Test Bed

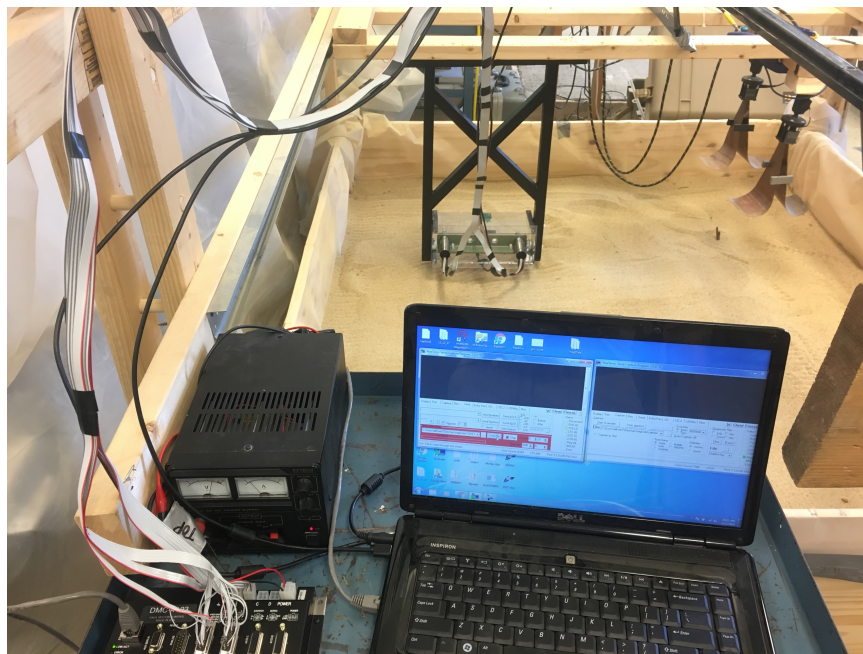


Figure 86: All Components of the Final Design



Figure 87: Size Reference of Unit

The final design pictured in Figure 84 and Figure 85 has a protective case because the motors at speeds over 100 Hz could cause serious damage or injury if something were to fail. The protective case is made out of Lexan and was heat formed into shape. The motor mount is fabricated using Dynaform fiberglass angle stock and was machined to accommodate the motors. The bolts connecting the support structure to the protective case are made of nylon and the support structure is constructed from wood. The magnet holder labeled in Figure 84 is made using an Anet A8 3-D printer and has a set screw to secure the holder to the motor shaft. Everything except for the motors is constructed from materials that will not interfere with the magnetic fields, promoting the strongest signal possible.

Chapter 5: Testing Results

Chapter 5 highlights the testing results for the 4 different categories of tests. These tests included motor speed and motor field tests, ferromagnetic tests, non-ferromagnetic tests, and Martian simulant tests. The goal of the testing was to determine the ability of the unit to test both ferromagnetic and non-ferromagnetic materials and the viability of the unit for extraterrestrial sensing.

5.1 Motor Testing

5.1.1 Rotation Rate Test

Quantifying the exact motor speed is critical for analyzing the sandbox test data. A series of tests were conducted to quantify the speed of the motor. The Galil Suite platform uses a jog command (JG) to tell the motor what speed to spin. A higher jog number corresponds with a faster motor speed. A number of factors decide how fast the motor spins; therefore, the jog number does not have a specified speed with it. The factors include input voltage, motor type, and motor size. A test was run to determine the correlation of the jog number to the motor speed for this application. In testing, the voltage was set at 24 V and the 3242G024BX4 motor was used. To measure the speed of the motor, a Hewlett Packard 35655A spectrum analyzer with an Electro-Metrics field probe collected and recorded frequency domain data. The test was run at 4 different speeds to determine if there is a linear correlation between the jog number and motor speed. The peak frequency is the speed at which the motors are spinning.

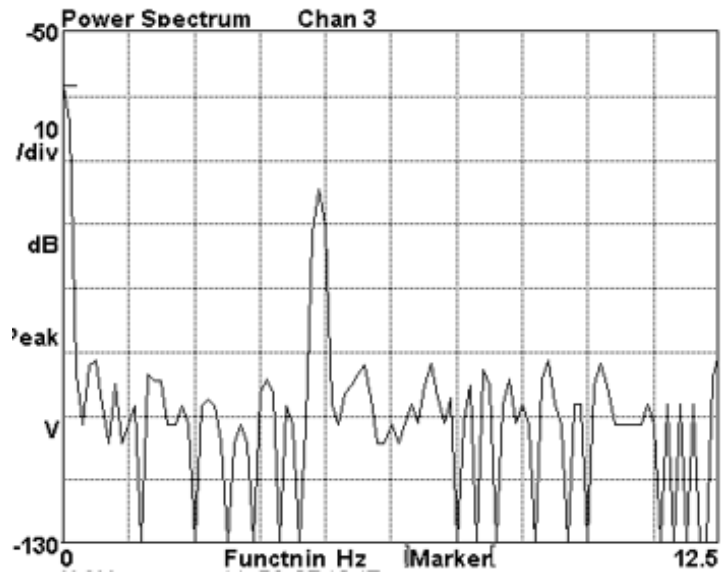


Figure 88: Speed Equals 4.8 Hz When Galil Set at JG20000

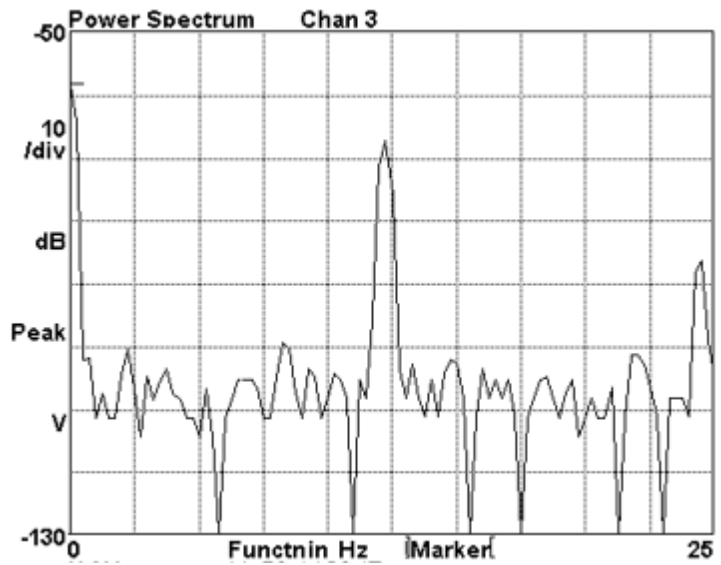


Figure 89: Speed Equals 12 Hz When Galil Set at JG50000

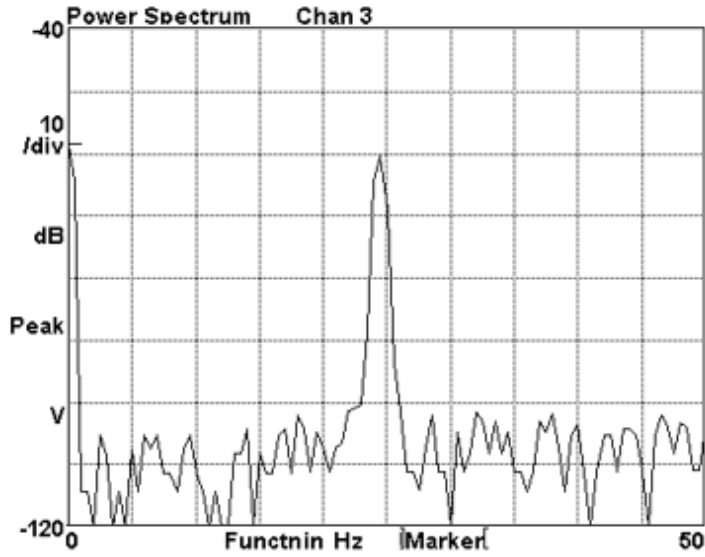


Figure 90: Speed Equals 24 Hz When Galil Set at JG100000

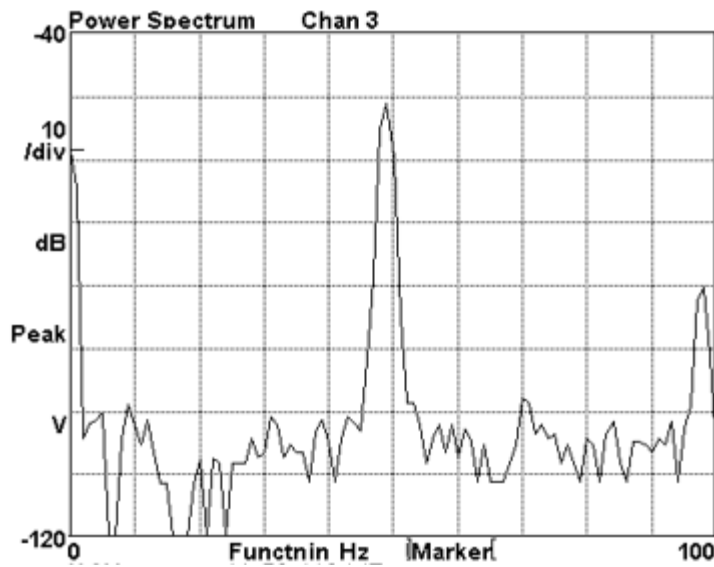


Figure 91: Speed Equals 48 Hz When Galil Set at JG200000

There is a linear correlation between the frequency values and the jog number used in Galil Suite. The correlation is 4166.67 Galil jog numbers per Hertz. Knowing the correlation between the two, the speed of the 3242G024BX4 motor with a 24V input can be determined for any Galil jog number.

5.1.2 Magnetic Field Motor Test

Brushless DC motors have a permanent magnet inside them, so a test was run to understand the effects of the spinning motor on the magnetic field. The results shown in Figure 92 quantify the field.

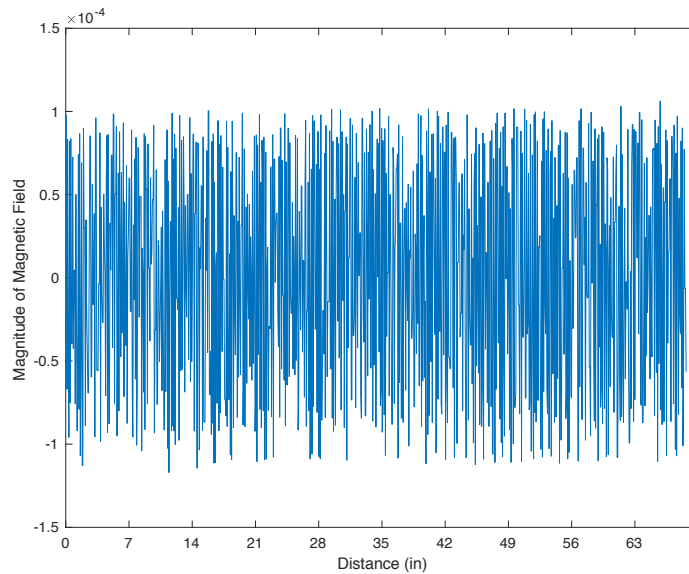


Figure 92: No Magnets Spinning Motor: X-Axis Data

The motors produce an oscillating field with a maximum amplitude of approximately $4.0 \times 10^{-4} \mu T$. This size field when compared to the oscillating field from the magnets is minimal. In Figure 140 the oscillating field from the spinning magnets has a maximum amplitude of approximately $16 \times 10^{-3} \mu T$ without an added perturbation. Comparing amplitude of the magnetic field for the spinning magnets and just the motors the difference between the two amplitudes is $15.7 \times 10^{-3} \mu T$, confirming the magnetic field produced by the motors is negligible.

5.2. Laboratory Testing

The viability of the dual rotating magnet depends on the ability of the unit to detect both ferromagnetic and non-ferromagnetic materials through a range of media. All tests were run in the sandbox test bed in Laboratory 103 in Perkins building on the University of Vermont campus. The test bed measures 72”L x 65”W, as seen in Figure 93: Sandbox Test Bed, and the unit was suspended 2 inches above the test bed surface. The sand is 10 inches deep and has a grain size of .079 inches with a density of 96.76 lb/ft³. One x coordinate plot is included from each test, the y and z coordinate plots are located in Appendix C.

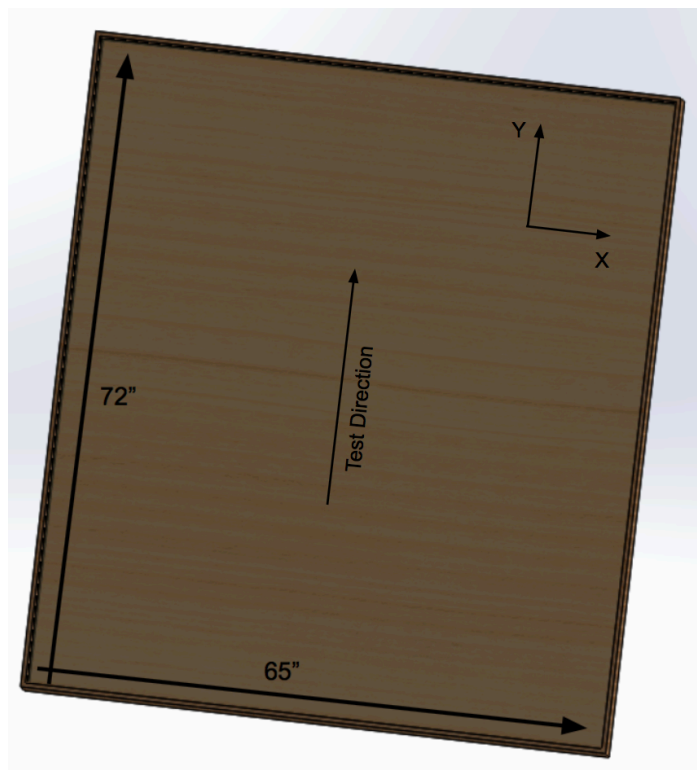


Figure 93: Sandbox Test Bed

Tests were run to examine if the new unit could match initial testing results conducted in November 2017 (see Appendix C for initial test results). Additional testing was conducted to explore the ability of the unit to induce eddy currents in non-ferromagnetic materials and detect those currents. The linear drive was set at a constant speed of 1.5 inches/second and a magnetometer reading was recorded at approximately every 0.08” as the unit moved across the length of the test bed. The data were plotted using Matlab and then a Hilbert transform was performed to plot the signal envelope. The envelope was plotted to better understand the ability of the dual rotating magnet unit to detect subsurface objects of interest. Two vertical red lines mark the start and end point of the region where the magnetometer senses the buried object.

5.2.1 Ferromagnetic Testing

A series of ferromagnetic tests were conducted at slow motor speeds to prove the dual rotating magnet unit can detect ferromagnetic materials. Initial tests were run to determine the viability of the dual rotating magnet system and compare results to the initial testing from November 2017, after improving the unit with the components explained in Section 4.2.

5.2.1.1 3 Buried Targets

The same 3 Buried Object test, as in Appendix C, was performed to prove the new unit’s functionality. The 3 targets were buried in the configuration seen in Figure 94, and each target was buried 4 inches below the surface. The motor speed, controlled through the Galil Suite interface was set to 4.8 Hz.

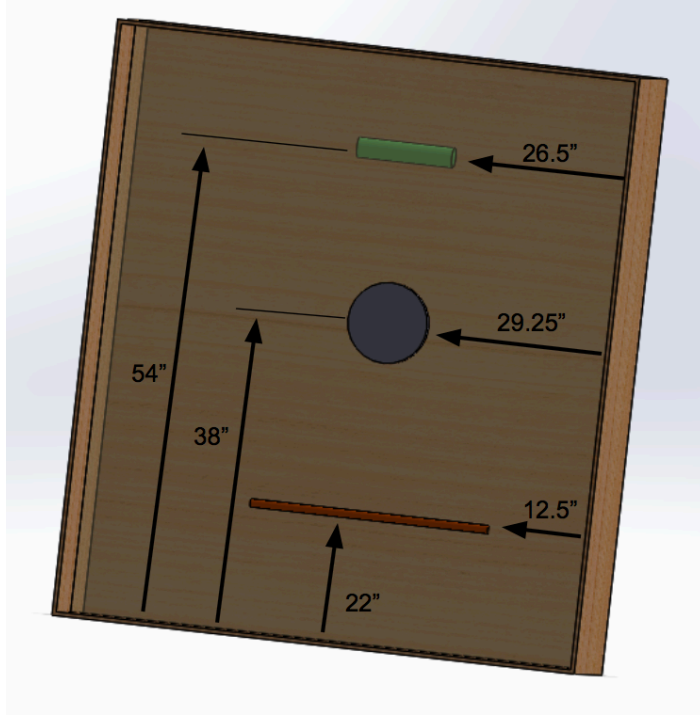


Figure 94: 3 Buried Target Configuration

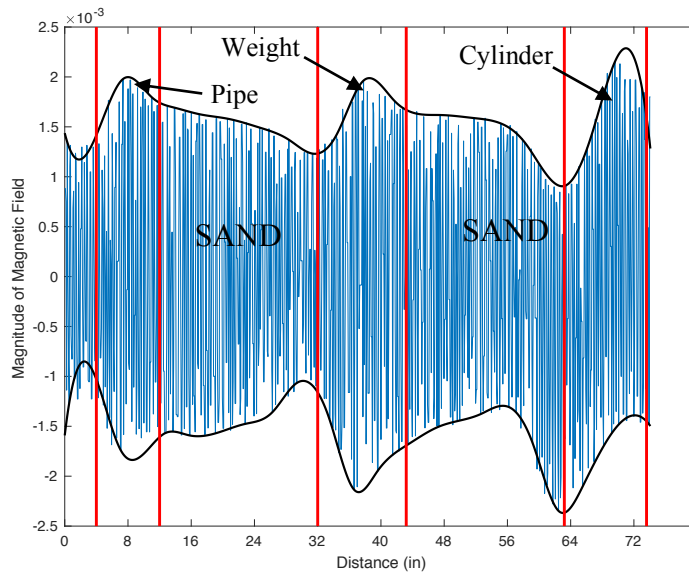


Figure 95: 3 Buried Targets Recorded X-Axis Data

The results show that the fourth iteration of the unit is able to detect the 3 buried targets. The increase in amplitude at three locations, shown by the vertical red lines, confirms the accuracy of the unit. This test leaves the following questions unanswered: 1) can shape of the envelope determine the size of the object, 2) how does the depth of the object affect the amplitude of the signal, and 3) how accurate is the unit at locating subterranean objects? The following isolation tests were conducted to answer these questions.

5.2.2 Depth Isolation Tests

Isolation depth tests were performed to understand how the magnetometer signal changes as the depth of the object increases or decreases. The tests were performed on three different ferromagnetic objects: an iron cylinder, a steel pipe, and an iron weight. The tests were conducted at three depths: 2.5, 4, 5.5 and 7 inches, each measured from the surface of the sand to top of the object.

5.2.2.1. Iron Cylinder Depth Test

The first depth test was conducted with the iron cylinder that measures 3”D x 12”L. The object was placed directly in the middle of the sandbox test bed, 36” from the starting position, as seen in Figure 96.

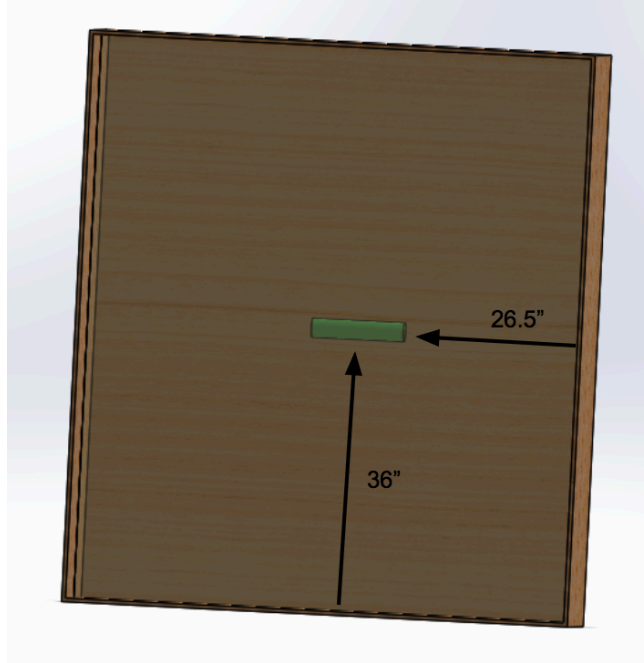


Figure 96: Iron Cylinder Location

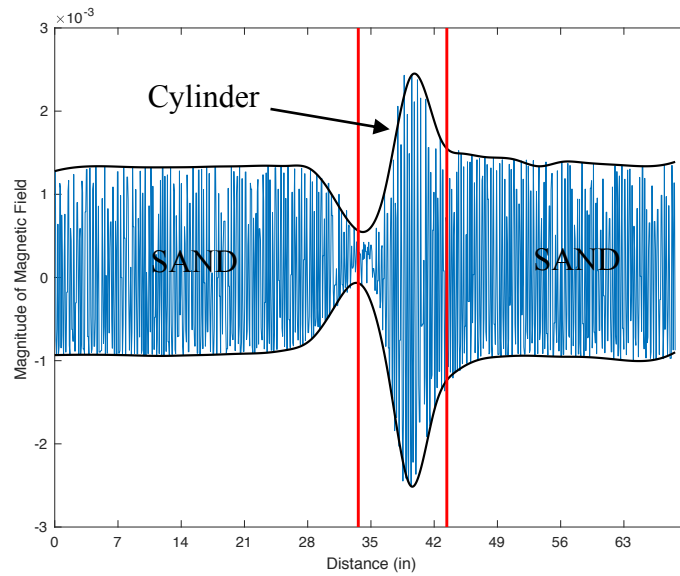


Figure 97: 2.5-Inch - Iron Cylinder Recorded X-Axis Data

When the object is 2.5 inches below the surface the results have an average magnitude change of approximately $\pm .002 \mu T$ in the X-direction, $\pm 0.001 \mu T$ in the Y-

direction and $\pm 0.003 \mu T$ in the Z-direction (see Appendix C for y and z coordinate results). According to the magnetometer data the center of the iron cylinder is located 38.5” into the scan. When compared to the measured location of 36 inches, seen in Figure 97, there is a location accuracy discrepancy of 2.5”.

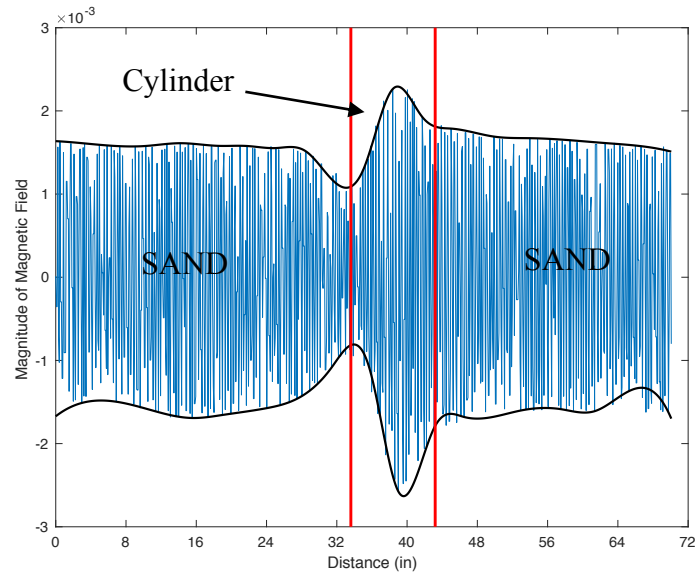


Figure 98: 4-Inch - Iron Cylinder Recorded X-Axis Data

When the cylinder is buried 4 inches below the surface the results show an average magnitude change of approximately $\pm 0.0013 \mu T$ in the X-direction, $\pm 0.001 \mu T$ in the Y-direction and $\pm 0.002 \mu T$ in the Z-direction. According to the magnetometer data the center of the iron cylinder is located 38.5” into the scan. When compared to the measured location of 36 inches seen in Figure 98, there is a location accuracy discrepancy of 2.5”.

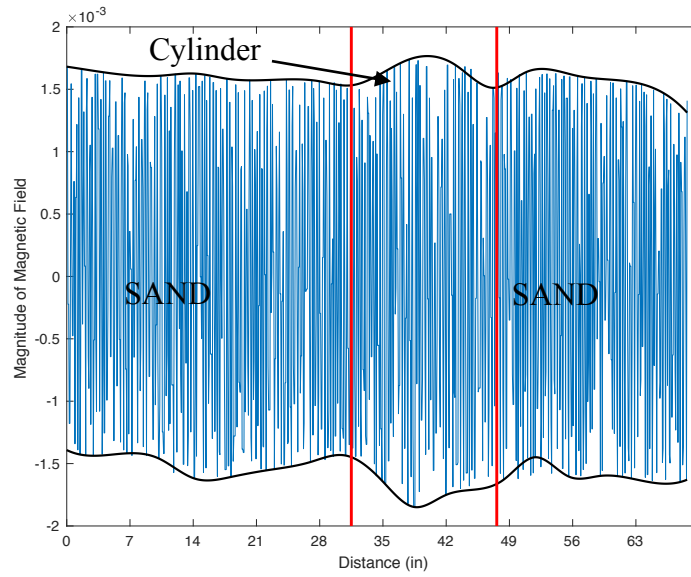


Figure 99: 5.5-Inch - Iron Cylinder Recorded X-Axis Data

When the cylinder is 5.5 inches below the surface, the results show an average magnitude change of approximately $\pm 0.0001 \mu T$ in the X-direction, $\pm 0.0005 \mu T$ in the Y-direction and $\pm 0.0005 \mu T$ in the Z-direction. According to the magnetometer data the center of the iron cylinder is located 37” into the scan. When compared to the measured location of 36” seen in Figure 99, there is a location accuracy discrepancy of 1”.

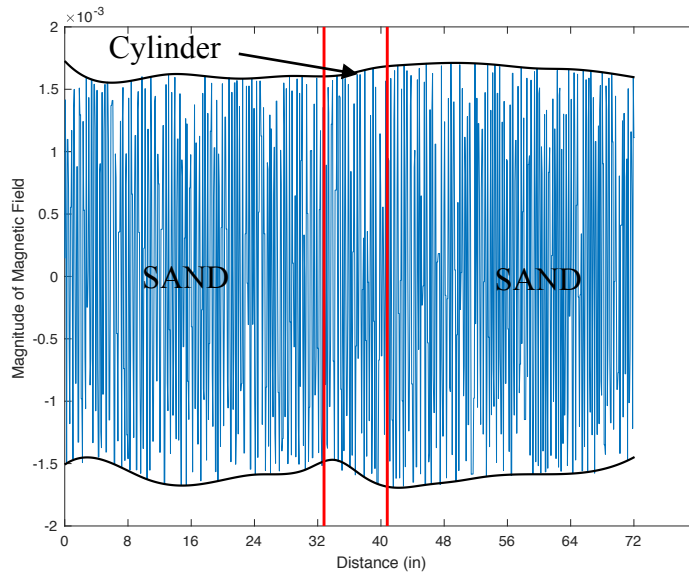


Figure 100: 7-Inch - Iron Cylinder Recorded X-Axis Data

When the object is 7 inches below the surface, the results show an average magnitude change of approximately $\pm 0.0001 \mu T$ in the X-direction, $\pm 0.0 \mu T$ in the Y-direction and $\pm 0.0 \mu T$ in the Z-direction. At a depth of 7 inches there is little signal variation to indicate the location of the iron cylinder.

It is apparent after analyzing the depth data that as the depth of the target increases the amplitude change of the signal over the target decreases. Additionally, as the depth increases, the location accuracy in the iron cylinder test decreases.

5.2.1.2 Pipe Depth Test

Similar to the cylinder test, a steel pipe measuring 1”D x 50.4”L with a wall thickness of 0.065” was buried in the center of the sandbox at depths 2.5, 4, 5.5 and 7 inches measured from the surface of the sand to the top of the pipe. By analyzing the x, y,

and z plots the amplitude change can be measured, which helps determine the sensitivity of the unit.

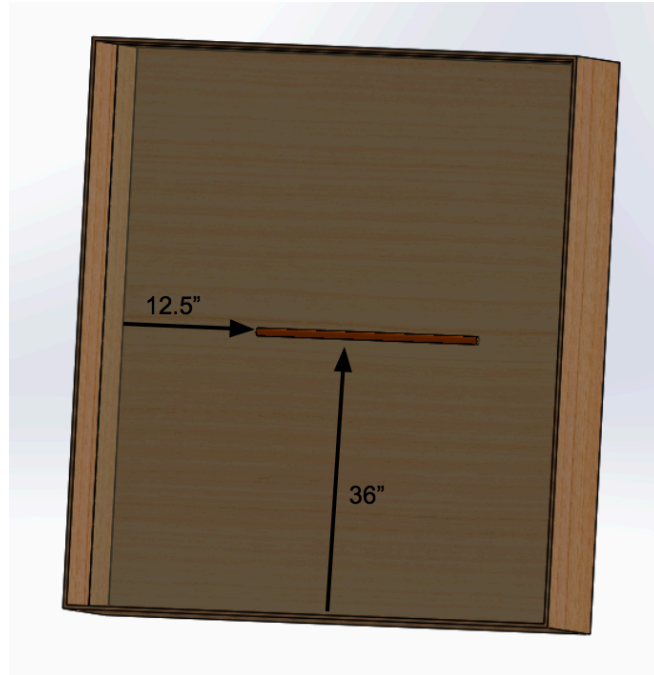


Figure 101: Steel Pipe Location

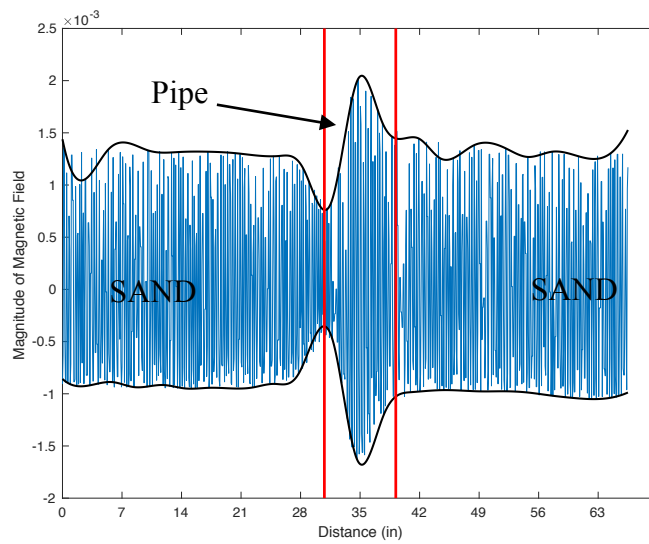


Figure 102: 2.5-Inch - Steel Pipe Recorded X-Axis Data

When the pipe is buried 2.5 inches below the surface, the results show an average magnitude change of approximately $\pm 0.0012 \mu T$ in the X-direction, $\pm 0.0008 \mu T$ in the Y-direction and $\pm 0.0018 \mu T$ in the Z-direction. According to the magnetometer data, the center of the steel pipe is located 35” into the scan. When compared to the measured location of 36” seen in Figure 103, there is a location accuracy discrepancy of 1”.

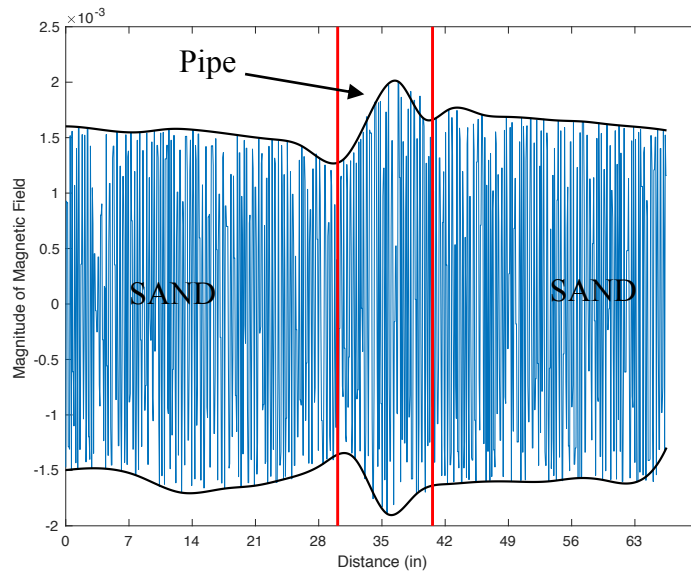


Figure 103: 4-Inch - Steel Pipe Recorded X-Axis Data

When the cylinder is buried 4 inches below the surface the results show an average magnitude change of approximately $\pm 0.0009 \mu T$ in the X-direction, $\pm 0.0005 \mu T$ in the Y-direction and $\pm 0.001 \mu T$ in the Z- direction. According to the magnetometer data the center of the steel pipe is located 35” into the scan. When compared to the measured location of 36” seen in Figure 103, there is a location accuracy discrepancy of 1”.

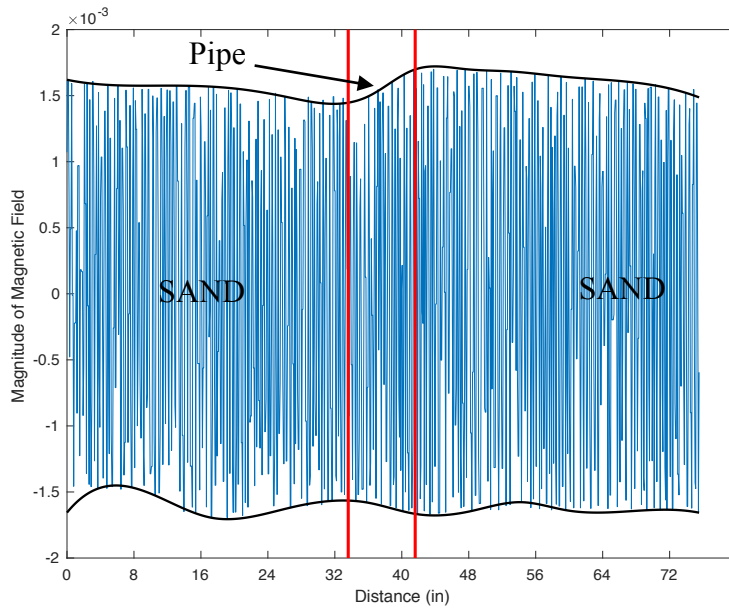


Figure 104: 5.5-Inch - Steel Pipe Recorded X-Axis Data

When the object is 5.5 inches below the surface, the results show an average magnitude change of approximately $\pm 0.0003 \mu T$ in the X-direction, $\pm 0.0 \mu T$ in the Y-direction and $\pm 0.0005 \mu T$ in the Z-direction. According to the magnetometer data, the center of the steel pipe is located 38" into the scan. When compared to the measured location of 36" seen in Figure 104, there is a location accuracy discrepancy of 2".

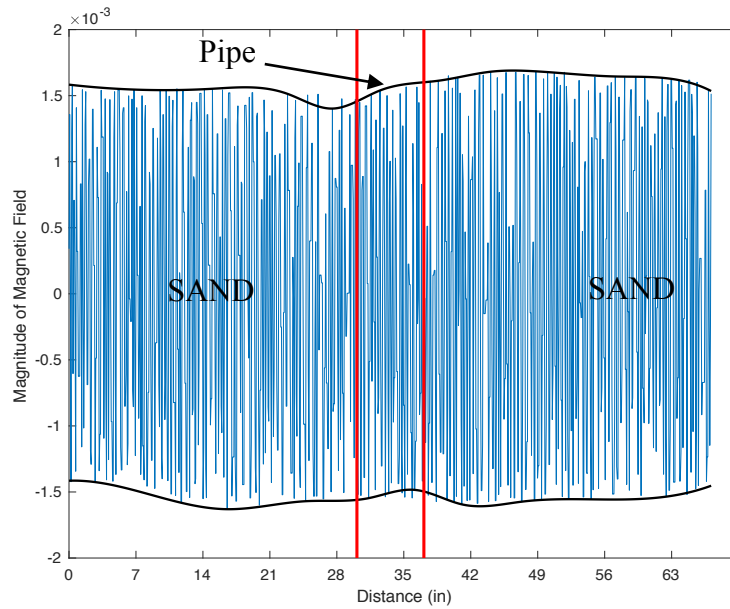


Figure 105: 7-Inch - Steel Pipe Recorded X-Axis Data

When the pipe is 7 inches below the surface, the results show an average magnitude change of approximately $\pm 0.0002 \mu T$ in the X-direction, $\pm 0.001 \mu T$ in the Y-direction and $\pm 0.0001 \mu T$ in the Z-direction. At a depth of 7 inches there is little signal variation to indicate the exact location of the steel pipe.

5.2.1.3 Iron Weight Test

The third depth test was run with a 5 pound iron weight measuring 6.5”D x .625”L buried at depths 2.5, 4, 5.5 and 7 inches. The weight was buried in the center of the sandbox as seen in Figure 106: Weight Location

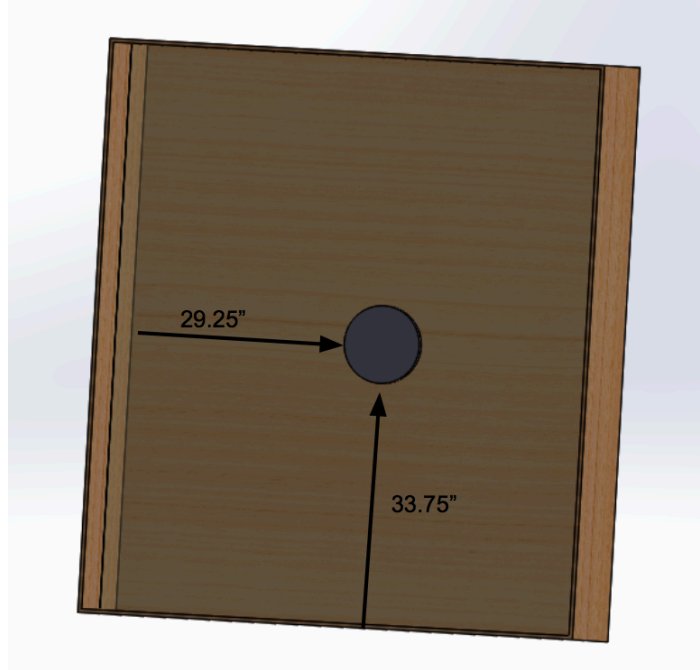


Figure 106: Weight Location

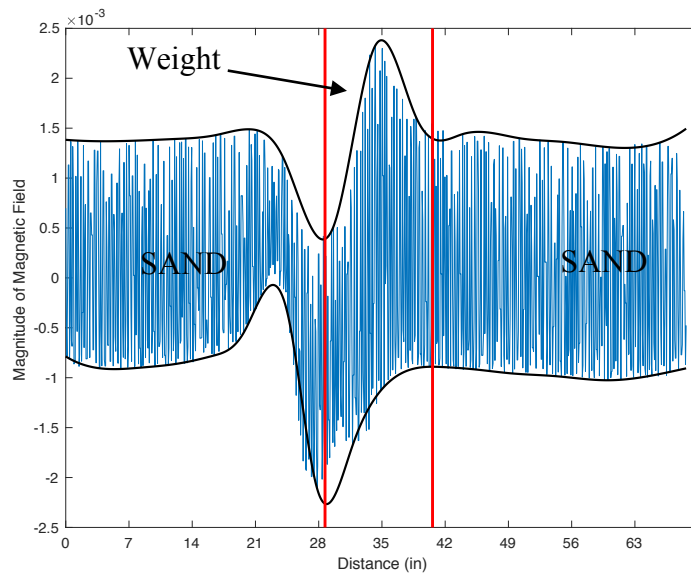


Figure 107: 2.5-Inch - Iron Weight Recorded X-Axis Data

When the weight is buried 2.5 inches below the surface, the results show an average magnitude change of approximately $\pm 0.002 \mu T$ in the X-direction, $\pm 0.0004 \mu T$ in the Y-

105

direction and $\pm 0.003 \mu T$ in the Z- direction. According to the magnetometer data the center of the iron weight is located 37" into the scan. When compared to the measured location of 37" seen in Figure 108, there is a location accuracy discrepancy of 2".

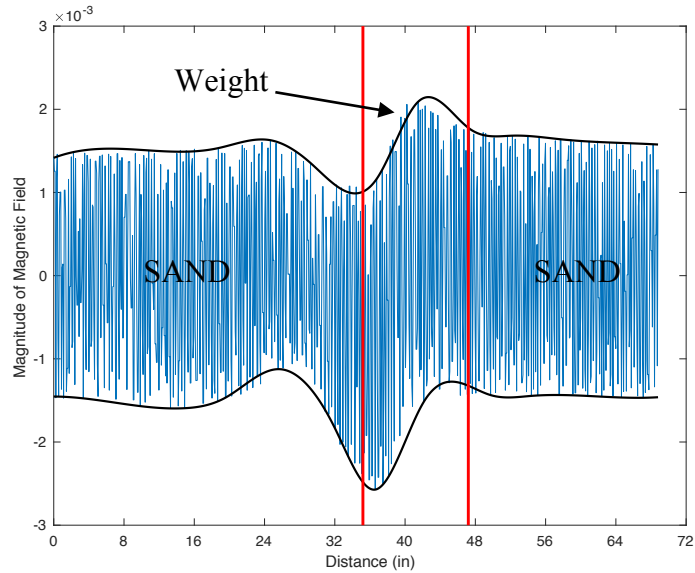


Figure 108: 4-Inch - Iron Weight Recorded X-Axis Data

When the weight is buried 4 inches below the surface, the results show an average magnitude change of approximately $\pm 0.0012 \mu T$ in the X-direction, $\pm 0.0002 \mu T$ in the Y-direction and $\pm 0.002 \mu T$ in the Z- direction. According to the magnetometer data the center of the iron weight is located 40" into the scan. When compared to the measured location of 37" seen in Figure 108, there is a location accuracy discrepancy of 3".

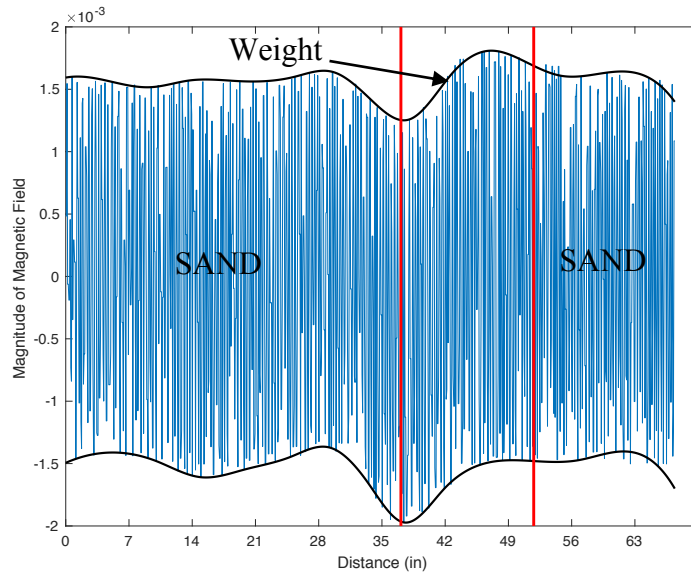


Figure 109: 5.5-Inch - Iron Weight Recorded Z-Axis Data

When the weight is buried 5.5 inches below the surface, the results show an average magnitude change of approximately $\pm 0.0005 \mu T$ in the X-direction, $\pm 0.0001 \mu T$ in the Y-direction and $\pm 0.0005 \mu T$ in the Z-direction. According to the magnetometer data the center of the iron weight is located 43” into the scan. When compared to the measured location of 37” seen in Figure 109, there is a location accuracy discrepancy of 6”.

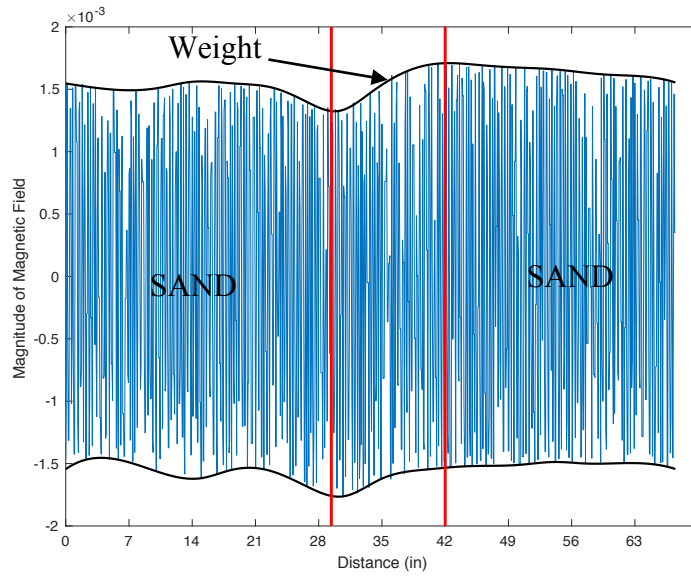


Figure 110: 7-Inch - Iron Weight Recorded Z-Axis Data

When the weight is buried 7 inches below the surface, the results show an average magnitude change of approximately $\pm 0.0003 \mu T$ in the X-direction, $\pm 0.0 \mu T$ in the Y-direction and $\pm 0.0005 \mu T$ in the Z-direction. According to the magnetometer data the center of the iron weight is located 36” into the scan. When compared to the measured location of 37” seen in Figure 110, there is a location accuracy discrepancy of 1”.

Similar to the iron cylinder and steel pipe test, there is a significant discrepancy in the amplitude of the signal over the target as the depth changes. As in the other two isolation tests as the depth of the target increases the location accuracy decreases.

5.2.3 Eddy Currents

Tests were run to determine whether the dual rotating magnet unit can induce eddy currents in non-ferromagnetic materials and be detected by the RM3100 magnetometer.

5.2.3.1 Extension Cord

The first test used a 100 ft extension cord coiled up with the male and female ends of the cord plugged into each other. The cord was buried 4 inches below the surface in the center of the sand box. The speed of the motor was set to 24 Hz. This explored the possibility of inducing a current into the copper wire of the extension cord. By plugging the two ends of the extension cord together it gives the current an easy path to travel, in theory making the copper wire easier to detect. The wire was orientated so the unit travels over one length of the coil, through the middle where there is no wire, and then over the other length of the coil.

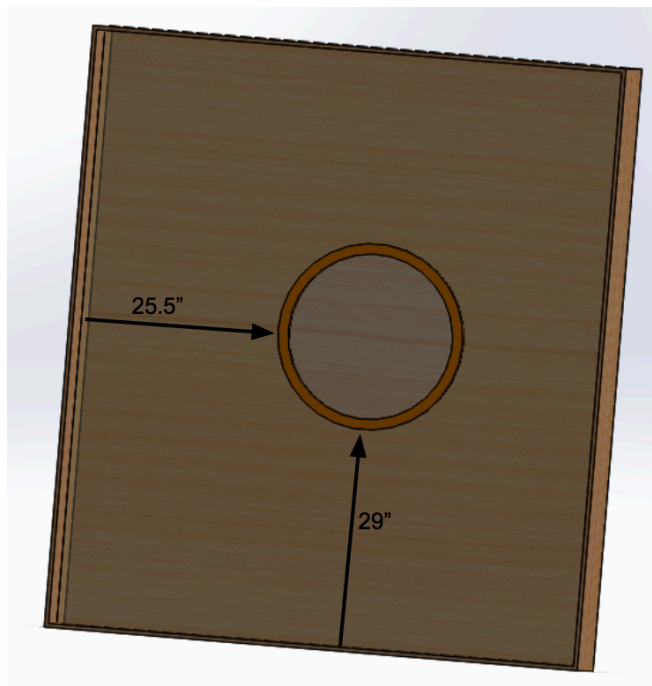


Figure 111: Extension Cord Location

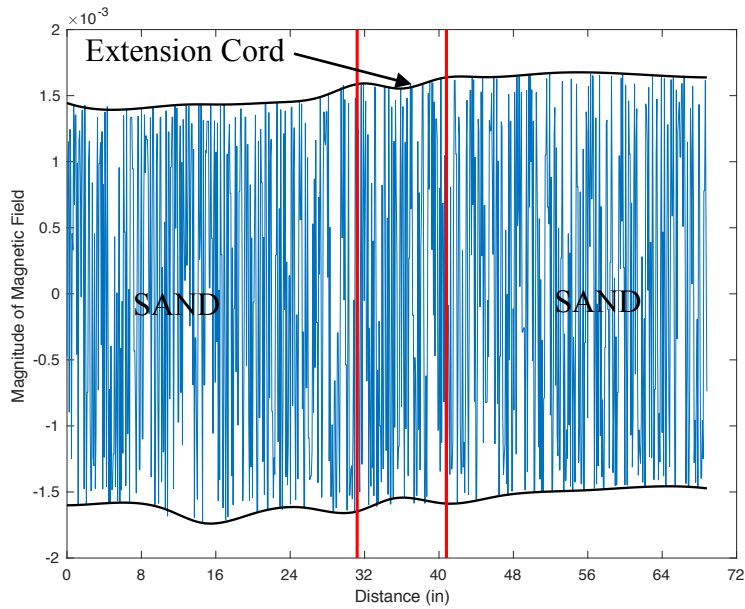


Figure 112: Plugged in Extension Cord X-Axis Data

The results from the plugged-in extension cord test show an average magnitude change of approximately $\pm 0.0001 \mu T$ in the X-direction, $\pm 0.0001 \mu T$ in the Y-direction and $\pm 0.0 \mu T$ in the Z-direction. In the X-direction plot, in Figure 112, the signal amplitude change shows the two lengths of the wire, which are marked by the vertical red lines.

5.2.3.1 Extension Cord Unplugged

The second test used the same 100ft extension cord coiled up with the male and female ends of the cord unplugged. The cord was buried 4 inches below the surface in the center of the sand box. The speed of the motor was set to 24 Hz. In theory since the two ends are unplugged the wire will be more difficult to detect because the induced current will not be able to loop in the coil.

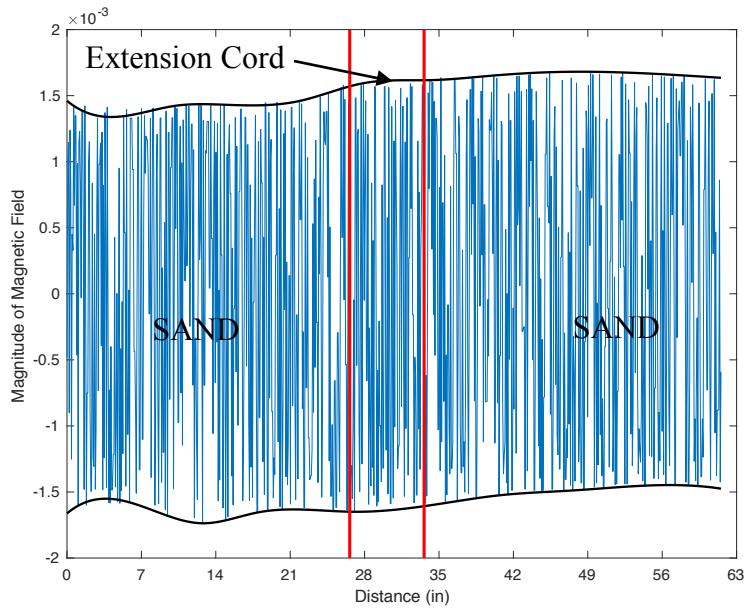


Figure 113: Extension Cord Recorded X-Axis Data

The results from the unplugged extension cord test show an average magnitude change of approximately $\pm .00005 \mu T$ in the X-direction, $\pm 0.0 \mu T$ in the Y-direction and $\pm 0.0 \mu T$ in the Z-direction. From the magnetometer data it is very difficult to understand where the extension cord is located. The X-direction magnetometer data, Figure 112, has a slight amplitude change around the location of the extension cord, but that is the only indication of the cord.

5.2.3.3 Aluminum

An eddy current test was conducted with an aluminum cylinder measuring 2”D x 33.5”L that was buried 4” below the surface of the sandbox. The test was performed at 3 different motor speeds (24 Hz, 4.8 Hz and 0 Hz) to determine if the unit was capable of inducing eddy currents into the aluminum cylinder.

For the first part of the test the motor speed was set at 24 Hz.

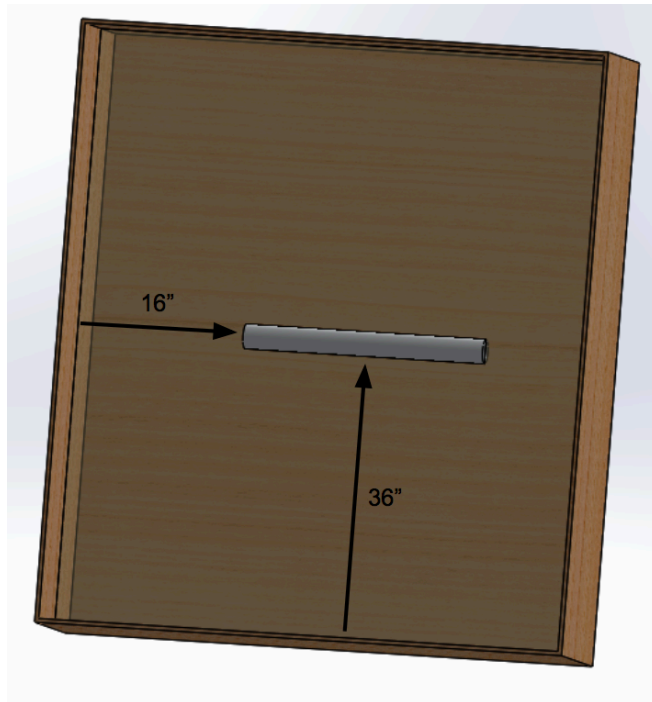


Figure 114: Aluminum Cylinder Location

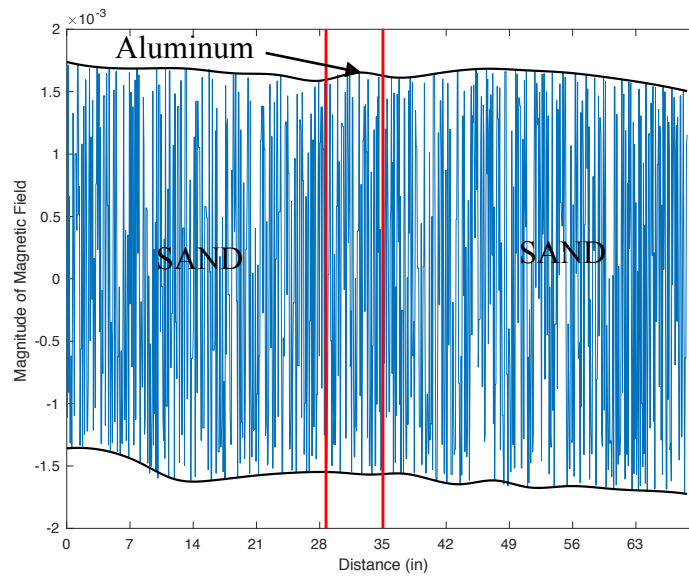


Figure 115: Speed 24 Hz: Aluminum Recorded X-Axis Data

The results at 24 Hz show an average magnitude change of approximately $\pm 0.0001 \mu T$ in the X-direction, $\pm 0.001 \mu T$ in the Y-direction and $\pm 0.0 \mu T$ in the Z-direction. In the X direction plot the increase in signal amplitude around the vertical red line proves that eddy currents can be induced and detected at speeds as low as 24 Hz. The location of the aluminum cylinder from the magnetometer reading is at 33 inches. The actual measured location is 36 inches.

The second test the motor speed was reduced to 4.8 Hz to see if it is still possible to see the aluminum cylinder.

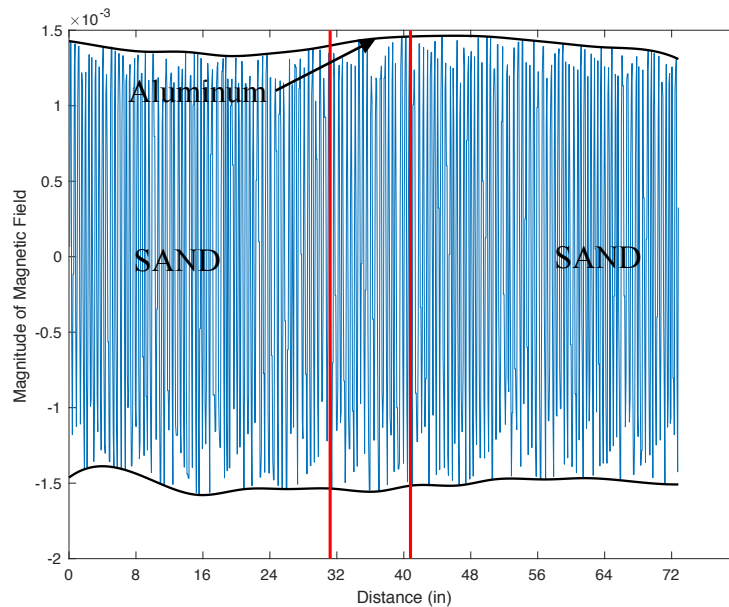


Figure 116: Speed 4.8 Hz: Aluminum Recorded X-Axis Data

The results show an average magnitude change of approximately $\pm 0.0 \mu T$ in the X-direction, $\pm 0.0 \mu T$ in the Y-direction and $\pm 0.0 \mu T$ in the Z-direction. The X, Y and Z

plots show little information about the location of the aluminum pipe. There is no signal variation that would indicate a buried aluminum pipe.

The third test was run without the magnets spinning, to see if the magnetometer without an induced field can detect the piece of aluminum.

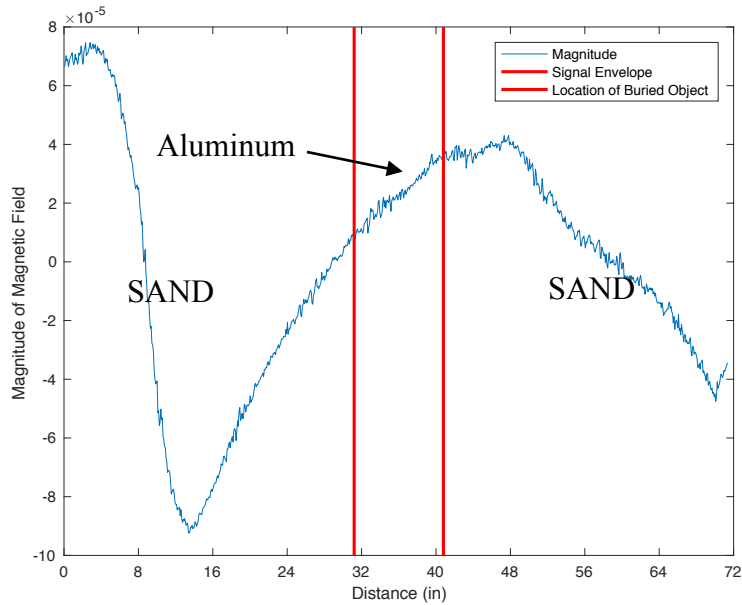


Figure 117: Speed 0 Hz: Aluminum Recorded X-Axis Data

From the plotted X, Y and Z magnetometer data, there is no signal variation that would indicate a buried aluminum pipe. The variation in the plots are caused by slight drifts in the signal, due to external magnetic materials in the lab. The drift is minimal and is the order of $1.0 \times 10^{-5} \mu T$.

The results from Section 5.2.3 indicate that the unit can induce and detect eddy currents in non-ferromagnetic magnetic materials. Shown by the 24 Hz test detecting the

location of the aluminum pipe through signal amplitude variation, while the 4.8 Hz test and 0 Hz test had no amplitude variation near the aluminum pipe.

5.2.4 Aluminum Depth Test

The final eddy current test was conducted to understand how the depth of the non-ferromagnetic object affects the locating accuracy of the dual magnet unit. This test explores the ability of the dual magnet unit to induce eddy currents at different depths. The aluminum cylinder was buried at 2.5", 4", 5.5" and 7".

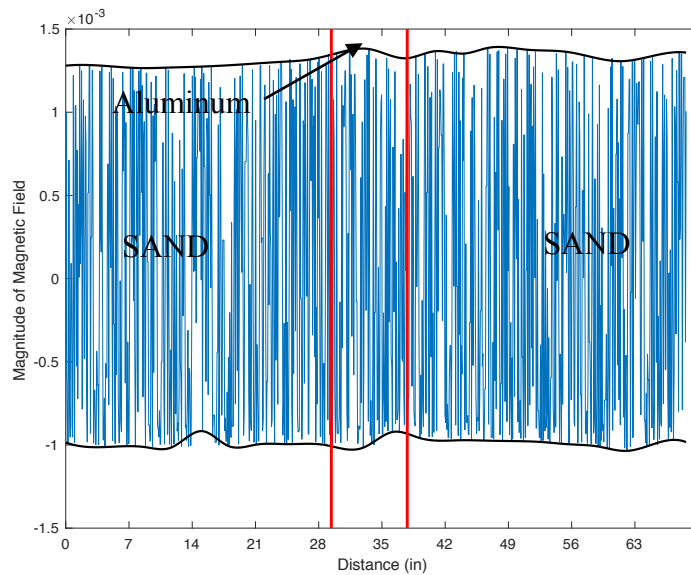


Figure 118: 2.5-Inch - Aluminum Recorded X-Axis Data

The 2.5-inch results show an average magnitude change of approximately $\pm 0.0002 \mu T$ in the X-direction, $\pm 0.0 \mu T$ in the Y-direction and $\pm 0.0005 \mu T$ in the Z direction. In the X direction plot the increase in signal amplitude around the vertical red lines confirms that eddy currents can be induced and detected at 2.5 inches below the surface. The

location from the magnetometer reading is at approximately 33.5 inches. The actual measured location is 36 inches and there is a location accuracy discrepancy of 2.5”.

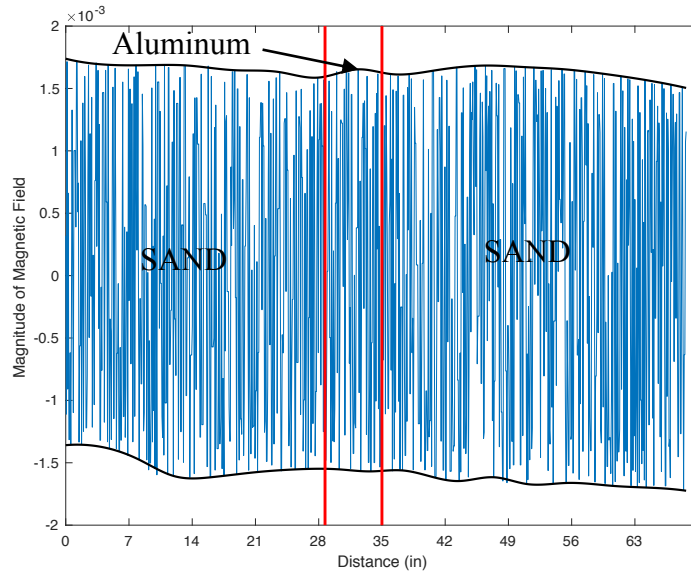


Figure 119: 4-Inch - Aluminum Recorded X-Axis Data

The 4-inch results show an average magnitude change of approximately $\pm 0.0002 \mu T$ in the X-direction, $\pm 0.0 \mu T$ in the Y-direction and $\pm 0.0005 \mu T$ in the Z direction. In the X direction plot the increase in signal amplitude around the vertical red lines confirms that eddy currents can be induced and detected at 4 inches below the surface. The location from the magnetometer reading is at approximately 33 inches. The actual measured location is 35 inches and there is a location accuracy discrepancy of 3”.

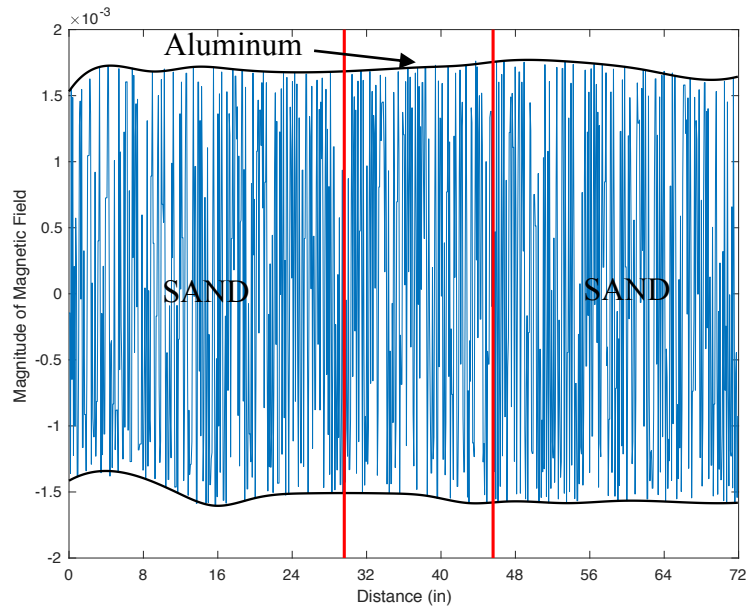


Figure 120: 5.5-Inch - Aluminum Recorded X-Axis Data

The 5.5-inch results show an average magnitude change of approximately $\pm 0.0 \mu T$ in the X-direction, $\pm 0.0 \mu T$ in the Y-direction and $\pm 0.0 \mu T$ in the Z-direction. At a depth of 5.5 inches there is a slight signal variation to determine the location of the aluminum pipe.

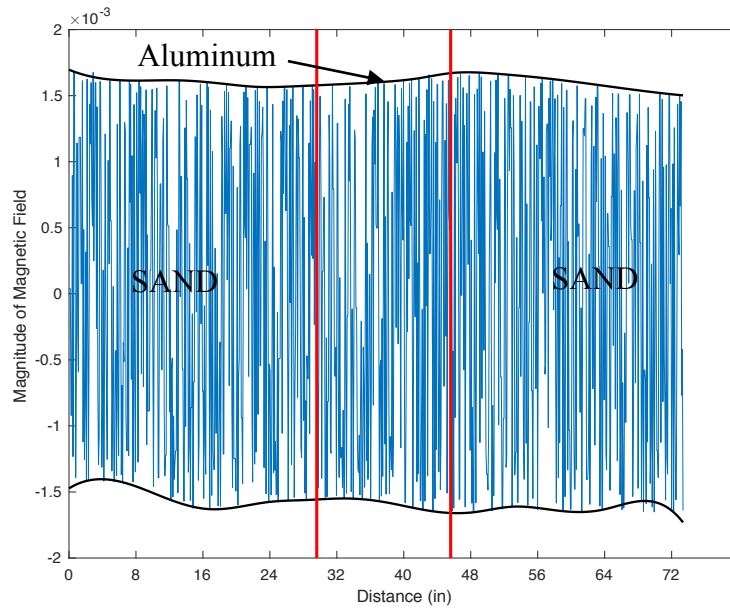


Figure 121: 7-Inch - Aluminum Recorded X-Axis Data

The 7-inch results show an average magnitude change of approximately $\pm 0.0 \mu T$ in the X-direction, $\pm 0.0 \mu T$ in the Y-direction and $\pm 0.0 \mu T$ in the Z-direction. At a depth of 7 inches there is a slight signal variation to indicate the location of the aluminum pipe.

At 4 inches the unit was able to induce eddy currents into the aluminum cylinder and detect the location of the object. As the distance increased to 5.5 inches and then 7 inches the unit was unable to detect the aluminum. Possible reasons for this include: 1) the motor speed and 2) the strength of the magnets. The motor speed could possibly be too slow to induce eddy currents at a farther distance because the magnets are not spinning fast enough to induce a large enough current. The strength of the magnets could also limit the ability of the unit to induce currents at larger depths.

5.2.5 Martian Soil Simulant Testing

To test the dual rotating magnet unit in Martian applications a series of tests were run to demonstrate its capabilities. A Martian simulant was made using steel wool that was rusted using water and salt. A steel wool and sand mixture was contained in a plastic bag measuring 10”L x 8”W x 0.5”H and was buried in the sandbox test bed to represent Mars’ iron-based soil. The mixture was composed of 13 percent by weight steel wool and the remaining 87 percent was sand.

5.2.5.1 Single Martian Simulant

The first test used a single simulant sample buried 2 inches below the surface to determine if the dual rotating magnet could locate the anomaly. The same test was conducted using a ground penetrating radar unit in order to compare the results.

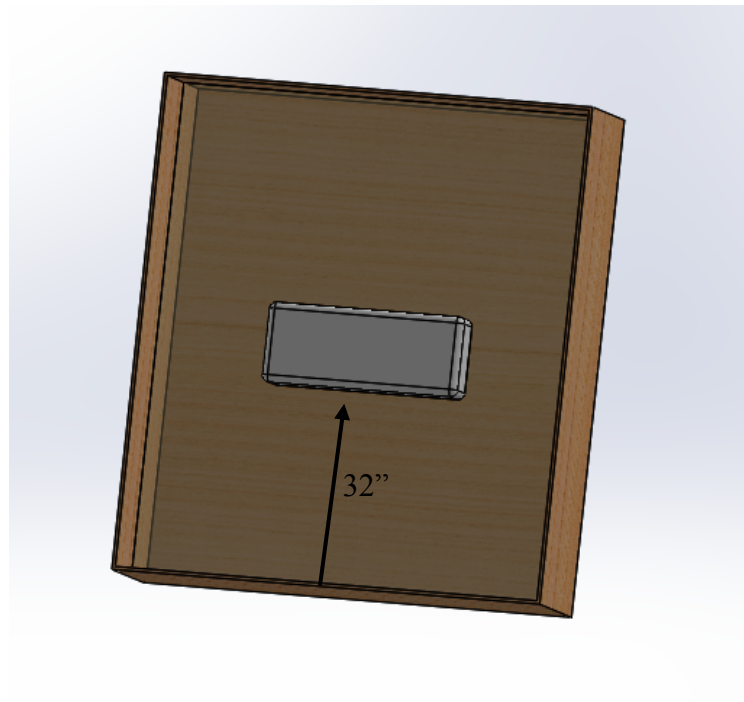


Figure 122: Single Martian Simulant Test Setup

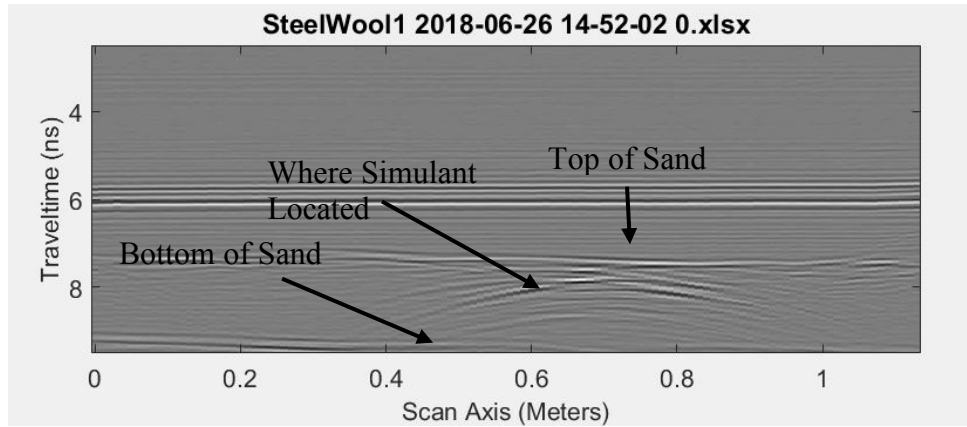


Figure 123: Martian Simulant GPR Data with Simulant

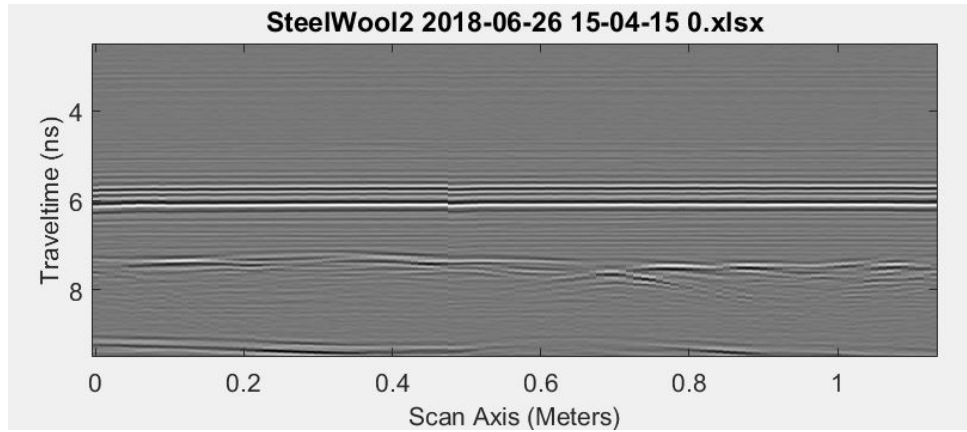


Figure 124: GPR Data without Simulant

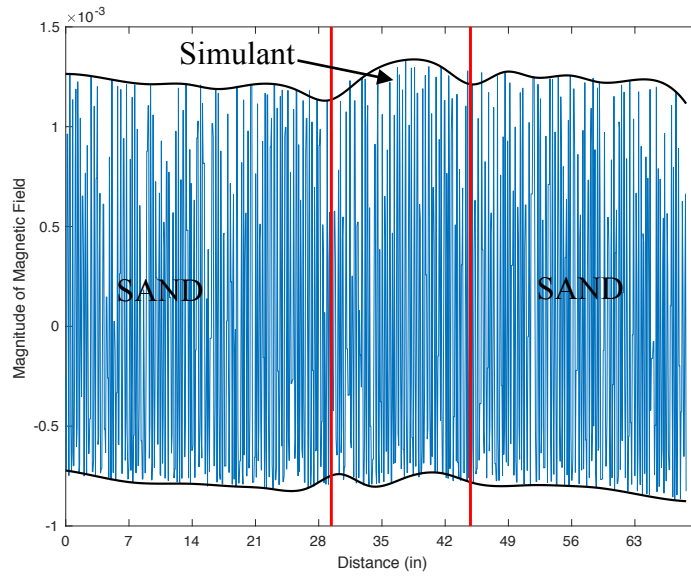


Figure 125: Martian Simulant - Magnet X-Axis Data

The Martian simulant was unable to be located by GPR. By comparing Figure 123 and Figure 124 with and without the simulant, there is little difference between the two GPR scans confirming the simulant cannot be detected by the GPR unit. The results from the dual rotating unit in Figure 125 show the simulant is clearly detected; the location is represented by the vertical red lines. The X-axis data has a maximum amplitude change of $2.5 \times 10^{-4} \mu T$.

5.2.5.2 Two Martian Simulants

The second test took the single sample test one step farther and had two buried simulant samples 2 inches below the surface. The samples were spaced 12 inches apart, as seen in Figure 126.

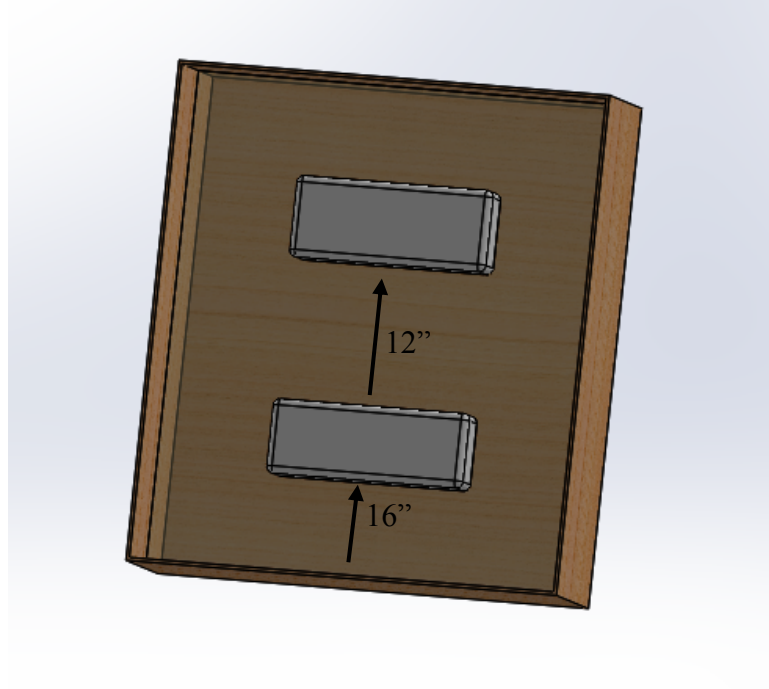


Figure 126: Two Martian Simulants Test Setup

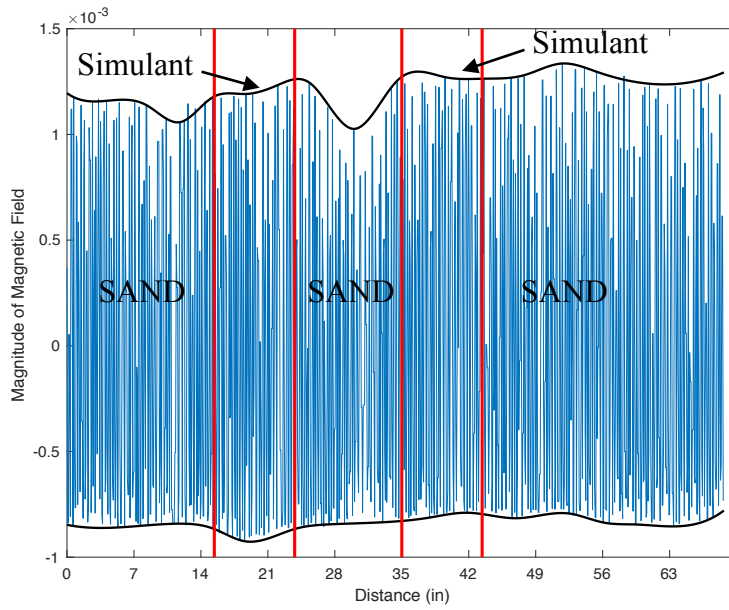


Figure 127: 2 Buried Martian Simulants X-Axis Data

The rotating magnet unit was able to detect both Martian simulants. The buried simulants are clearly located in Figure 127 by the change in amplitude of $2.0 \times 10^{-4} \mu T$ at both locations of the simulant, represented by the vertical red lines.

5.2.5.3 Martian Simulant – Air, Water, and Ice Tests

The air, ice and water tests were designed to represent a situation encountered on Mars. The test setup used the same two samples of Martian simulant used in Section 5.2.5.2 with the addition of an air, water, or ice pocket between the samples. The air pocket was represented by an empty plastic container, the water pocket was represented by a plastic container filled with water, and the ice pocket was represented by a plastic container filled with ice. Each sample measured 12”L x 12”W x 4”D and the top of the sample was buried 2” below the surface of the sand. This situation could represent Martian soil with a water, ice or air pocket just beneath the surface. NASA is specifically interested in this topic because they want the rovers to be able to avoid soft pockets and therefore avoid getting stuck. Additionally, locating water or ice is a high priority for NASA to determine the possibilities of past and future life on Mars.

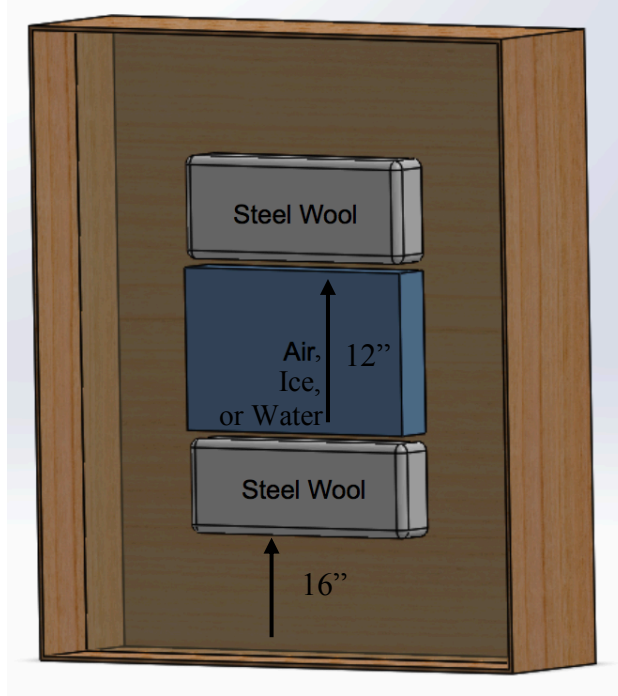


Figure 128: Air, Water, and Ice Tests Setup

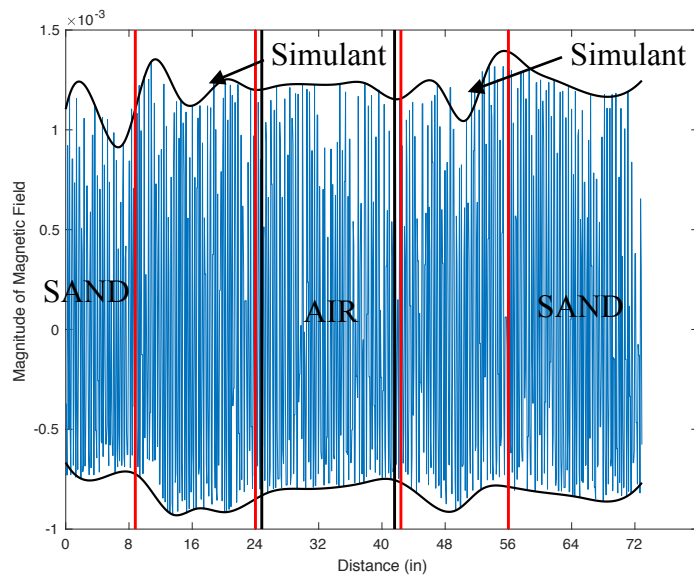


Figure 129: Martian Simulant with Air Pocket: X-Axis Data

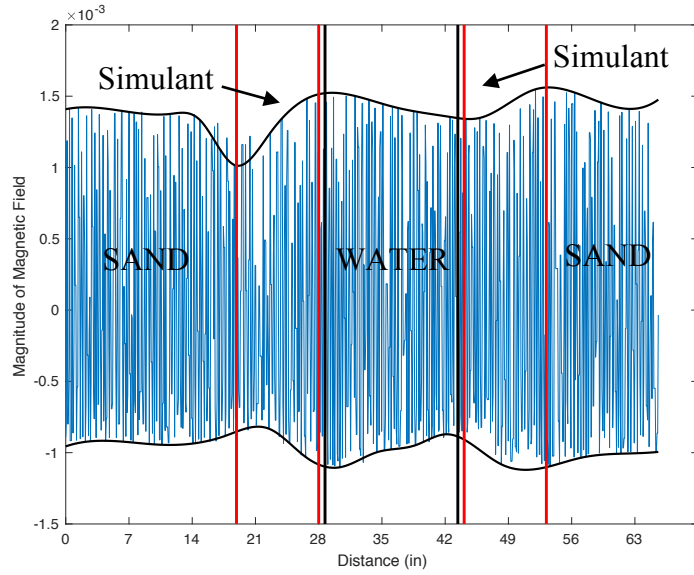


Figure 130: Martian Simulant with Water Pocket: X-Axis Data

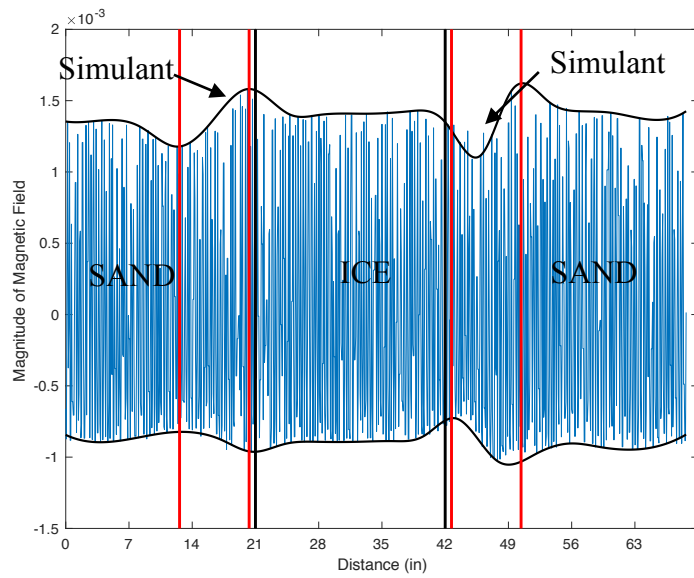


Figure 131: Martian Simulant with Ice Pocket: X-Axis Data

The rotating magnet unit was able to detect both subsurface anomalies and show that there is no magnetic object between them in the air, water and ice tests. The buried simulants are clearly located in Figure 129 by the change in amplitude of $3.0 \times 10^{-4} \mu T$ at

both locations of the simulant, represented by the vertical red lines. In Figures Figure 130Figure 131 the simulants are located by the $5.0 \times 10^{-4} \mu T$ amplitude change. The air, water and ice pockets are located by the decrease in amplitude between the two simulants.

The results confirm that the dual rotating magnet device is capable of sensing soil anomalies, specifically with Martian applications. By demonstrating the ability to sense the steel wool simulant, the unit can in theory sense changes in soil densities and pockets of air, water, or ice in high content iron-based soils.

5.3 Additional Post Processing

To improve the sensing ability of the dual rotating unit, additional post processing steps were taken. The X-axis data from the three buried objects test in Section 5.2.1.1 were used. The raw three buried objects data easily located the subsurface objects, allowing for easy comparison between the results. Two different post processing tests were run to see if the sensitivity of the unit could be improved.

The first test removes the magnetic field produced by the motors spinning from the three buried object results. The results from Section 5.1.2 (Spinning Motor Test) were subtracted from the results in Section 5.2.1.1 (3 Buried Objects Test).

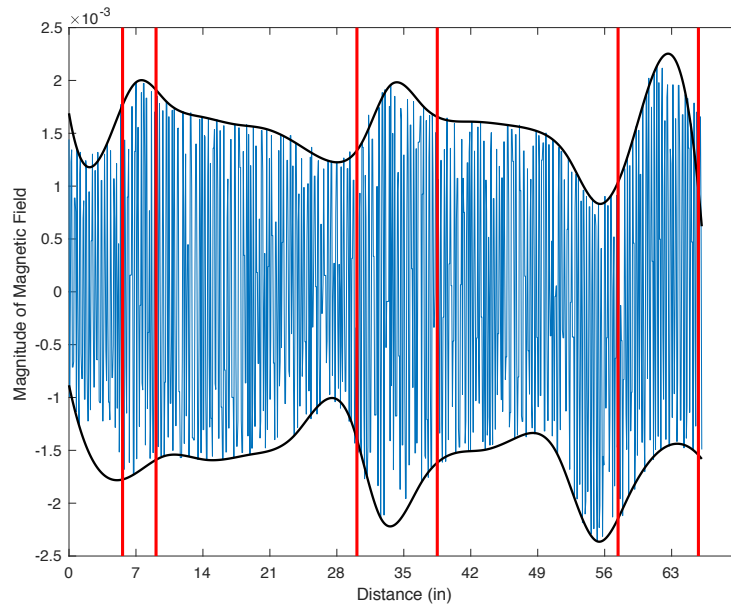


Figure 132: Original 3 Buried Objects X-Axis Data

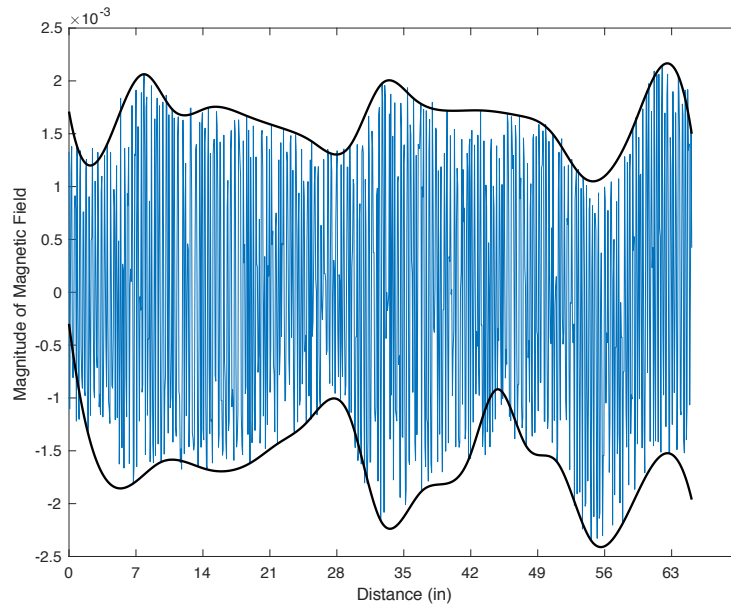


Figure 133: 3 Buried Objects Test X-Axis Data with Motor Field Removed

Comparing Figure 132 and Figure 133 the amplitude of the recorded signal is larger in the plot with the spinning motor signal removed. The amplitude changes in Figure 133 are $0.8 \times 10^{-3} \mu T$, $0.7 \times 10^{-3} \mu T$, and $1.3 \times 10^{-3} \mu T$ for each object respectively. The amplitude changes in Figure 132 are $0.15 \times 10^{-3} \mu T$, $0.25 \times 10^{-3} \mu T$, and $0.3 \times 10^{-3} \mu T$. This confirms that the sensitivity is increased by removing the magnetic field produced by the motor.

The second test removes the background magnetic field from the three-buried objects test. The background magnetic field is where the motors and magnets are spinning while the unit is moving the length of the sandbox.

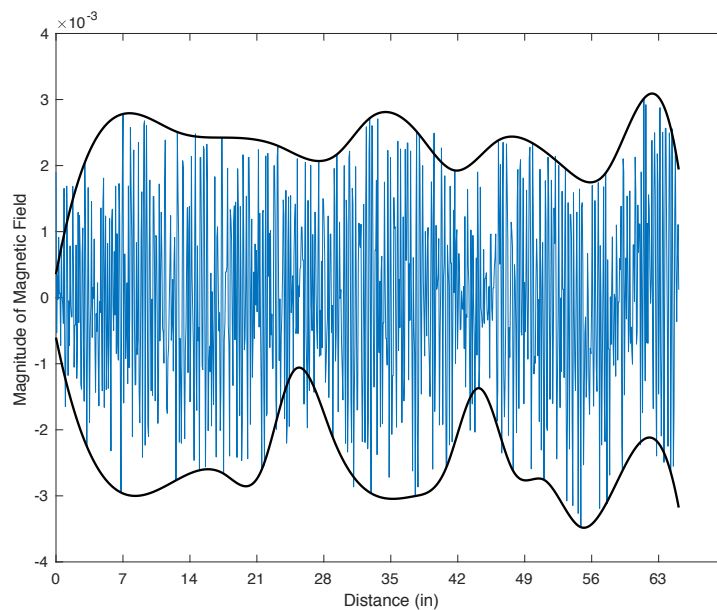


Figure 134: 3 Buried Objects Test X-Axis Data with Background Field Removed

The amplitude changes in Figure 134 are $1.2 \times 10^{-3} \mu T$, $0.8 \times 10^{-3} \mu T$, and $1.2 \times 10^{-3} \mu T$ for each object respectively. When comparing the amplitude change in

Figure 132 and Figure 134 it is confirmed that the sensitivity is increased by removing the background magnetic field.

In both tests the results improve the sensing ability of the dual rotating magnet unit. Comparing Figure 133 and Figure 134 the change in amplitude is on average $0.134 \times 10^{-3} \mu T$ larger when the background magnetic field is removed than when the motor field is removed. Further analysis of the two figures shows that the shape of the curve in Figure 133 (motor field removed) makes the buried objects more apparent. Although the change in amplitude is $0.134 \times 10^{-3} \mu T$ smaller, more details about the location of the objects can be deduced by the pronounced shape of the curves in Figure 133 with the motor field removed.

5.4 Discussion

The ability of the unit to detect both ferromagnetic and non-ferromagnetic materials is confirmed by the testing results. Both materials can be detected at high speeds and only magnetic materials can be detected at slow speeds. Using the results at both high and low speeds and the process of elimination, the magnetic properties of the material can be determined.

The results show that the unit has difficulty sensing at depths larger than 5.5 inches for both ferromagnetic and non-ferromagnetic materials. In Section 5.3 two post processing tests were successfully run to improve the locating accuracy of the data. This is an additional step when processing the data, but it could significantly improve the sensitivity of the unit without having to make additional changes to the unit.

The location accuracy of the raw data could be improved by increasing the magnet strength. The magnets used in the testing have an approximate pull force of 40 lbs. By using a stronger magnet, the magnetic field strength would increase and improve the sensitivity of the unit. Additionally, increasing the sampling rate of the magnetometer to allow for higher motor speeds would increase the induced eddy currents allowing detection at larger depths of non-ferromagnetic objects.

Chapter 6: Conclusions and Future Work

6.1 Results

6.1.1 Ferromagnetic Results

The ferromagnetic testing was successful in locating shallow subsurface objects. As the depth increased the sensitivity of the unit decreased. Comparing the measured location versus the detected location of the object, the location determined by the x axis data in all cases was the closest to the actual location. By analyzing the low depth tests, quality information about the subsurface objects can be obtained.

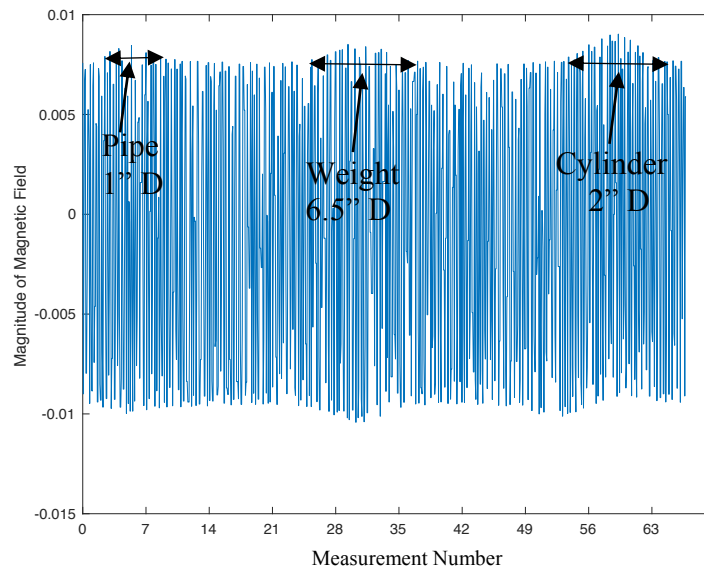


Figure 135: 3 Buried Objects Test: Z Axis Data

In the three-buried object test, the exact location and size of each object is known and can be related to the test data to understand how the amplitude change corresponds to the size of the buried object. By analyzing the three peaks in Figure 135 there is a direct correlation between the peak and the diameter of the object. A larger focal width of the

curve correlates to a larger diameter object. For example, for the 4-inch depth test, the iron pipe has a 1-inch diameter and the focal width in Figure 135 is approximately 100 measurements corresponding to 8 inches, meaning the magnetometer detected the 1-inch pipe for 8 inches during the scan. The cylinder has a 2-inch diameter and focal width of 200 measurements or 16 inches. This proves that for a cylinder-shaped object a focal width of 8 inches is equivalent to a 1-inch object. The weight has a 6.5-inch diameter with a focal width of 350 measurements or 28 inches. For a circular shaped object, the correlation is a focal width of 4.3 inches per object inch.

There are a number of unanswered questions from testing. It is still unknown how to differentiate object depth versus size of object. Theoretically only the amplitude of the curve will be dependent on depth and the focal width will remain the same. Therefore, the focal width can be measured, and the size of the object can be determined. The depth of the object can then be determined based on the amplitude. Unfortunately, during testing the magnets used were not strong enough to have accurate results below 4 inches, so this theory could not be tested.

6.1.2 Eddy Current Results

One of the main advantages of the dual rotating magnet unit is its ability to detect both ferromagnetic and non-ferromagnetic materials and the unit's ability to differentiate between them. The eddy current testing confirmed that this is possible by showing, at higher speeds, both magnetic and nonmagnetic objects can be detected, but at speeds lower than 10 Hz only magnetic objects can be detected. Similar to the ferromagnetic testing, the eddy current results showed difficulty sensing at greater depths. Results at a depth of

4 inches were repeatedly able to locate the object, but as depth increased locating became difficult.

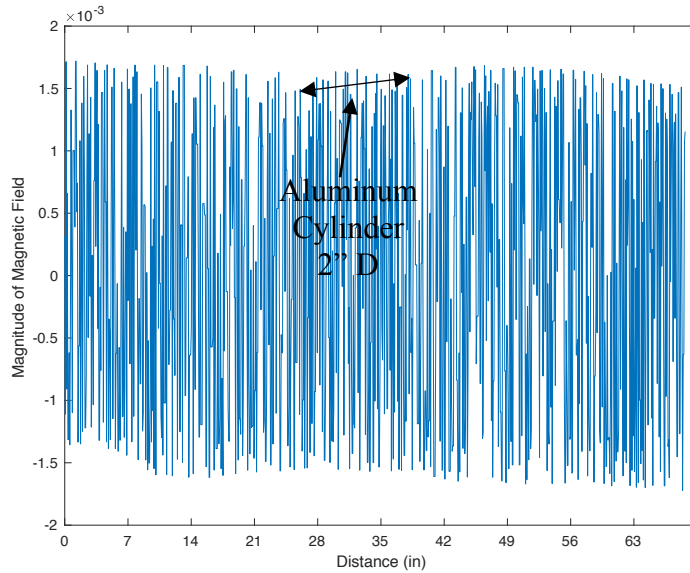


Figure 136: Aluminum X Axis Data

The correlation between the curve and the size of the object discussed in Section 6.3 holds true for the aluminum cylinder. The measured focal width in Figure 136 is approximately 16 inches corresponding to a 2” diameter cylinder.

The next step for eddy current testing is to determine if differentiating between different types of non-ferromagnetic objects is possible. For example, is it possible to tell the difference between a copper pipe, aluminum pipe and a lead pipe? All are non-ferromagnetic but are used for different applications.

6.1.3 Martian Simulant

The unit proved the ability to sense a simulant of Martian soil, showing the possibilities of extraterrestrial applications. By analyzing the graphs in Section 5.2.5, the difference between the simulant, air, water, ice, and sand can be distinguished. Further testing is required to be able to quantify the amplitude change to the percentage of iron in the soil. As in the other tests, larger magnets would improve the sensitivity of the unit, magnifying the soil anomalies and improving the post processing.

6.1.4 Post Processing

The post processing tests in Section 5.3 increased the sensitivity of the unit. The test confirmed that by removing the magnetic field produced by the spinning permanent magnet in the motors and the magnetic field produced by the spinning magnets, both increased the change in amplitude over the subsurface objects. Initial findings determined that removing the motor field was the most effective way to improve the locating accuracy. Further testing is required to understand if this is the case for both ferromagnetic and non-ferromagnetic materials.

6.2 Unit

Four different test units were designed, each with the premise of rotating two diametrically polarized magnets in a synchronized orientation. The final iteration seen in Figure 85 addressed the problems of the three previous iterations. Using the Galil motion controller, the motors can rotate at speeds up to 13500 rpm while maintaining phase control between the two motors. The unit is designed to work in the sandbox test bed. An improvement to the unit would be to design a magnet holder to accommodate larger

cylinder magnets. Being able to test with larger magnets would explore the theory that stronger magnets increase sensitivity, enabling the units to sense objects at larger depths. The magnets used for testing were neodymium magnets with a dimension of 1/2”D x 1”L and an approximate pull force of 40 pounds. There are numerous options, but Applied Magnets offers a 1”D x 1”L cylinder magnet that has a pull force of approximately 90 lbs. This would be a simple upgrade to the unit to see if it would improve functionality at larger depths.

Once the final unit was built and testing began an issue arose with the Faulhaber motors and encoders. The motors suddenly stopped initializing, meaning the controller was unable to determine the initial position of the motors and could not initiate motion. Using a Goldstar OS-9020A 20 MHz oscilloscope it was determined that the Hall sensors were no longer working. The motors were then sent back to Faulhaber and replaced with the same motor, but a slightly longer body. The reason for the failure of the Hall sensors is undetermined.

6.3 Magnetometer

The PNI RM3100 paired with the PNI communication board, according to the specification and compact size, made it the correct choice for the application. According to the data sheet the magnetometer has a maximum sample rate of 1600 Hz or 533.3 Hz per axis without compromising sensitivity. Numerous issues occurred throughout the testing process. First, upon arrival the unit failed to work, after multiple weeks of debugging the board it was determined that the unit had never been programmed and was returned to PNI for a programmed unit. Once testing began the magnetometer worked

properly. The default settings on the magnetometer are set to sample at 37 Hz per axis. In an attempt to change the default settings, it was determined that the communication board is unable to exceed a sample rate greater than 60 Hz per channel. By using an Arduino Uno instead of the PNI Communication board this problem could be solved. An Arduino Uno can sample at rates as high as 8.9 kHz.

Works Cited

- [1] Hysteresis. www.ndeed.org/EducationResources/CommunityCollege/MagParticle/Graphics/BHCurve.gif.
- [2] What's Hysteresis?, www.lassp.cornell.edu/sethna/hysteresis/WhatIsHysteresis.html.
- [3] 2450GR GROUND PENETRATING RADAR. <https://subsite.com/uploads/2450GR-specs.pdf>.
- [4] HOLMBERG, HANS-CHRISTER, and STEFAN LINDINGER. "Biomechanical Analysis of Double Poling InElite Cross-Country Skiers." American College of Sports Medicine, Dec. 2004. Web. 8 May 2017.m'
- [5] Ferromagnetism-Physics, Encyclopedia Britannica. [Online]. Available: <https://www.britannica.com/science/ferromagnetism>. [Accessed: 06-Dec-2017].
- [6] G. Klingelhfer et al., Jarosite and Hematite at Meridiani Planum from Opportunity's Mossbauer Spectrometer, Science, vol. 306, no. 5702, pp. 1740-1745, Dec. 2004.
- [7] Minerals.net. Jarosite: The Mineral Jarosite Information and Pictures, www.minerals.net/mineral/jarosite.aspx.
- [8] Minerals.net. Hematite: The Mineral Hematite Information and Pictures, www.minerals.net/mineral/hematite.aspx.
- [9] Overview - Mars 2020 Rover. NASA, NASA, mars.nasa.gov/mars2020/mission/overview/.
- [10] NASA, NASA, mars.nasa.gov/mer/mission/spacecrafts/overview.html.
- [11] Van Dam, Remke L, et al. Iron Oxides as a Cause of GPR Reflections. GEOPHYSICS, 2002.
- [12] EngineersGarage, Magnetometers, 6-2012. [Online]. Available: <https://www.engineersgarage.com/articles/magnetometer>. [Accessed: 16-Jan-2018].
- [13] Doolittle, James A., and Eric C. Brevik. The Use of Electromagnetic Induction Techniques in Soils Studies. Geoderma, vol. 223-225, 2014, pp. 3345., doi:10.1016/j.geoderma.2014.01.027.
- [14] Y. Zhang, L. Collins, H. Yu, C. E. Baum, and L. Carin, Sensing of unexploded ordnance with magnetometer and induction data: theory and signal processing, IEEE Transactions on Geoscience and Remote Sensing, vol. 41, no. 5, pp. 1005-1015, May 2003.
- [15] The Editors of Encyclopedia Britannica. Lenz's Law. Encyclopedia Britannica, Encyclopedia Britannica, Inc., 4 Jan. 2018, www.britannica.com/science/Lenzs-law.
- [16] The Editors of Encyclopedia Britannica. Faraday's Law of Induction. Encyclopedia Britannica, Encyclopedia Britannica, Inc., 6 Sept. 2013, www.britannica.com/science/Faradays-law-of-induction.
- [17] Dunbar, Brian. MISSION, GOALS, OBJECTIVES. NASA, NASA, www.nasa.gov/offices/emd/home/mgo.html.
- [18] Winn, John Sterling. Stoichiometry of Iron Oxides. Iron Oxides, 6 Jan. 2004, www.dartmouth.edu/genchem/0304/winter/5w04/lecture/rust.html.
- [19] HMR2300-D21-232. Honeywell Microelectronics and Precision Sensors Sensors, Transducers DigiKey, www.digikey.com/product-detail/en/honeywell-

- microelectronics – precision – sensors/HM R2300 – D21 – 232/342 – 1016 – N D/334171.
- [20] USB Magnetometer - Sensors - MultiDimension Technology, The Leading Supplier of TMR Magnetic Sensors, www.dowaytech.com/en/sensor/usb_magnetometer.html.
 - [21] Eddy Currents. Princeton.edu, Princeton University, www.princeton.edu/ssp/joseph-henry-project/eddy-currents/eddy_wiki.pdf.
 - [22] KREUTZBRUCK, M., et al. DC Field Compensation for Eddy Current Measurements on Steel Parts Using Dc-Coupled Magnetometer. DC Field Compensation for Eddy Current Measurements on Steel Parts Using Dc-Coupled Magnetometer, www.ndt.net/article/wcndt00/papers/idn290/idn290.htm.
 - [23] LATEST. All About Circuits, www.allaboutcircuits.com/textbook/direct-current/chpt-14/electromagnetic-induction/.
 - [24] Mars Exploration Rover - Spirit. NASA, NASA, www.jpl.nasa.gov/missions/mars-exploration-rover-spirit-mer/.
 - [25] appliedmagnets.com/images/0.375x1-TD.jpg.
 - [26] <https://www.kjmagnetics.com/images/blog/magsw9.jpg>
 - [27] <https://solarscience.msfc.nasa.gov/images/Dipole2e.gif>
 - [28] www.kjmagnetics.com/images/blog/halbachsalt.png.
 - [29] "Micromo DC Motor Calculations." <https://www.micromo.com/technical-library/dc-motor-tutorials/motor-calculations#stepone>
 - [30] M. Beryl, M. Princ, and P. Sustek, "BLDC Motor with Hall Sensors and Speed Closed Loop, Driven by eTPU on MPC5554," 2006.
 - [31] B. Olshausen, "Aliasing," 2000.
 - [32] "PNI Communication Board Data Sheet." 2017. <https://www.pnicorp.com/support/>
 - [33] "PNI RM3100 Data Sheet," 2017. <https://www.pnicorp.com/support/>
 - [34] "Motor Follower- Electronic Gearing," 2002. <http://www.machinedesign.com/basics-design/motor-follower-electronic-gearing>
 - [35] "Electronic Gearing." Galil. <http://www.galil.com/news/electronic-gearing>
 - [36] "Advanced Applications of Electronic Gearing." Galil. http://www.galil.com/download/whitepapers/wp_gearing_part1.pdf
 - [37] D. Huston. Multi-dipole Magnetic Field. University of Vermont. 2018
 - [38] T. Agarwal. Magnetometers-Types and Applications like Metal Detectors and Geographical Surveys. <https://www.elprocus.com/magnetometers-types-applications/>
 - [39] <https://www.quora.com/How-can-you-explain-an-eddy-current-AC-or-DC>

Appendix A Steps for Processing Data in Matlab

A.1 Upload File Function to Matlab

First using Microsoft Excel to take the .txt file from the magnetometer and organize the data by choosing the correct rows and deleting the spaces after each bit of data to make 3 bit strings for each reading. After saving the Excel file as a .txt this Matlab function uploads the data and converts it from a table to a string array.

```
function FILENAMEin1 = importfile(filename, startRow, endRow)
%IMPORTFILE Import numeric data from a text file as a matrix.
%   BOT3BURIED4IN1 = IMPORTFILE(FILENAME) Reads data from text file
%   FILENAME for the default selection.
%
%   BOT3BURIED4IN1 = IMPORTFILE(FILENAME, STARTROW, ENDROW) Reads data
from
%   rows STARTROW through ENDROW of text fileFILENAME.
%
% Example:
%   BOT3BURIED4in1 = importfile('BOT_3BURIED4in.txt', 1, 981);
%
%   See also TEXTSCAN.

% Auto-generated by MATLAB on 2018/06/22 16:07:43

%% Initialize variables.
delimiter = '\t';
if nargin<=2
    startRow = 1;
    endRow = inf;
end

%% Read columns of data as text:
% For more information, see the TEXTSCAN documentation.
formatSpec = '%s%s%s%[\n\r]';

%% Open the text file.
fileID = fopen(filename,'r');

%% Read columns of data according to the format.
% This call is based on the structure of the file used to generate this
% code. If an error occurs for a different file, try regenerating the
code
% from the Import Tool.
dataArray = textscan(fileID, formatSpec, endRow(1)-startRow(1)+1,
'Delimiter', delimiter, 'TextType', 'string', 'HeaderLines',
startRow(1)-1, 'ReturnOnError', false, 'EndOfLine', '\r\n');
```



```

for block=2:length(startRow)
    frewind(fileID);
    dataArrayBlock = textscan(fileID, formatSpec, endRow(block)-
startRow(block)+1, 'Delimiter', delimiter, 'TextType', 'string',
'HeaderLines', startRow(block)-1, 'ReturnOnError', false, 'EndOfLine',
'\r\n');
    for col=1:length(dataArray)
        dataArray{col} = [dataArray{col};dataArrayBlock{col}];
    end
end

%% Close the text file.
fclose(fileID);

%% Convert the contents of columns containing numeric text to numbers.
% Replace non-numeric text with NaN.
raw = repmat({''},length(dataArray{1}),length(dataArray)-1);
for col=1:length(dataArray)-1
    raw(1:length(dataArray{col}),col) = mat2cell(dataArray{col},
ones(length(dataArray{col}), 1));
end
numericData = NaN(size(dataArray{1},1),size(dataArray,2));

%% Split data into numeric and string columns.
rawNumericColumns = {};
rawStringColumns = string(raw(:, [1,2,3]));

%% Create output variable
BOT3BURIED4in1 = raw;

```

A.2 Function to Convert from 2's Complement to Decimal Number

This function is necessary for converting the data in the .txt file from a hex representation of 2's complement to a decimal number.

```

function [x]=nhex2dec(hexstring,n)
% hexstring : hex representation of two's complement of
xmydec=hex2dec(hexstring);
% x : input decimal number
% n : number of bits to perform 2's complements
x = hex2dec(hexstring);
x = x - (x >= 2.^(n-1)).*2.^n;

```

A.3 Evaluate Function nhex2dec and Plot Envelope

This script takes the string array generated from A.1 and evaluates each cell at of the array into a decimal number and then plots the value. The envelope of the oscillating signal is then solved.

```
A = BOT3BURIED6in; %table2array(TEST1); %Converts from table to array
X=linspace(0,981,981)'; %Creates x vector
D= nhex2dec(A,24); %Calls function nhex2dec and converts from hex to
dec
F=(D/8388607)*3; %Converts from voltage to micro Tesla's

plot(X,F(:,1)); %Plots x values
xlabel('Time (s)');
ylabel('Magnitude');
title('X AXIS');
figure
plot(X,F(:,2)); %Plots y values
xlabel('Time (s)');
ylabel('Magnitude');
title('Y AXIS');
figure
plot(X,F(:,3)); %Plots z values
xlabel('Time (s)');
ylabel('Magnitude');
title('Z AXIS');

figure
envelope(F(:,1),45,'peak')
xlabel('Time (s)');
ylabel('Magnitude');
title('X Axis Peak Upper and Lower Envelope');

figure
envelope(F(:,2),50,'peak')
xlabel('Time (s)');
ylabel('Magnitude');
title('Y Axis Peak Upper and Lower Envelope');

figure
envelope(F(:,3),46,'peak')
xlabel('Time (s)');
ylabel('Magnitude');
title('Z Axis Peak Upper and Lower Envelope');
%ylim([-0.022, .022]);
figure
[up,lo] = envelope(F(:,1),50,'peak');
plot(X,up,X,lo,'linewidth',1.5)
xlabel('Time (s)');
```

```
ylabel('Magnitude');
title('X Axis Upper and Lower Envelope');
```

```
figure
[up,lo] = envelope(F(:,2),50,'peak');
plot(X,up,X,lo,'linewidth',1.5)
xlabel('Time (s)');
ylabel('Magnitude');
title('Y Axis Upper and Lower Envelope');
```

```
figure
[up,lo] = envelope(F(:,3),50,'peak');
plot(X,up,X,lo,'linewidth',1.5)
xlabel('Time (s)');
ylabel('Magnitude');
title('Z Axis Upper and Lower Envelope');
```

```
figure
[up,lo] = envelope(F(:,1),45,'peak');
plot(X,up,'linewidth',1.5)
xlabel('Time (s)');
ylabel('Magnitude');
title('X Axis Upper Envelope');
```

```
figure
[up,lo] = envelope(F(:,2),50,'peak');
plot(X,up,'linewidth',1.5)
xlabel('Time (s)');
ylabel('Magnitude');
title('Y Axis Upper Envelope');
```

```
figure
[up,lo] = envelope(F(:,3),50,'peak');
plot(X,up,'linewidth',1.5)
xlabel('Time (s)');
ylabel('Magnitude');
title('Z Axis Upper Envelope');
```

A.4 Plots Location of Objects

Code takes the plotted curve from A.3 and plots a vertical red line at the location of each subsurface object.

```
A = BOTDEPTHCYL7; %table2array(TEST1); %Converts from table to array
X=linspace(0,981,981)'; %Creates x vector
D= nhex2dec(A,24); %Calls function nhex2dec and converts from hex to
dec
F=(D/8388607)*3; %Converts from voltage to micro Tesla's
```

```

figure
envelope(F(:,1),45,'peak')
xlabel('Time (s)');
ylabel('Magnitude');
title('X Axis Peak Upper and Lower Envelope');

hold on
yL = get(gca,'YLim');
line([480 480],yL,'Color','r','LineWidth',2);
%line([500 500],yL,'Color','r','LineWidth',2);
%line([900 900],yL,'Color','r','LineWidth',2);
legend('Magnitude','Location of Buried Object');
title('3 Buried Targets X Axis');
xlabel('Time (s)');
ylabel('Magnitude');

figure
envelope(F(:,2),30,'peak')
xlabel('Time (s)');
ylabel('Magnitude');
title('Y Axis Peak Upper and Lower Envelope');

hold on
yL = get(gca,'YLim');
line([480 480],yL,'Color','r','LineWidth',2);
%line([500 500],yL,'Color','r','LineWidth',2);
%line([900 900],yL,'Color','r','LineWidth',2);
legend('Magnitude','Location of Buried Object');
title('3 Buried Targets Y Axis');
xlabel('Time (s)');
ylabel('Magnitude');

figure
envelope(F(:,3),45,'peak')
xlabel('Time (s)');
ylabel('Magnitude');
title('Z Axis Peak Upper and Lower Envelope');

hold on
yL = get(gca,'YLim');
line([480 480],yL,'Color','r','LineWidth',2);
%line([500 500],yL,'Color','r','LineWidth',2);
%line([900 900],yL,'Color','r','LineWidth',2);
legend('Magnitude','Peak Envelope');
title('3 Buried Targets Z Axis');
xlabel('Time (s)');
ylabel('Magnitude');

```

A.5 Dual Magnet Vector Plot

```
mu=1386532.885;%Constant C for B Field
```

```

theta1=90;
theta2=270;
l_x=6;%domain size
l_y=4;
Nx=40;%number of domain points
Ny=40;
deltax=l_x/Nx;%number of points per unit L
deltay=l_y/Ny;
N=(Nx+1)*(Ny+1);%total number of points in domain
pc=zeros(N,2);%point coords
c=1;
for j=0:Nx % creates a domain
    for i=0:Ny
        pc(c,1)=j*deltax;
        pc(c,2)=l_y-i*deltay;
        c=c+1;
    end
end

m=[1 3;2.25 3];%magnet position
R=zeros(2,2,5);%creates array for rotation matrix
%Rotation matrices
R(:,:,1)=[cosd(theta1) sind(theta1);-sind(theta1) cosd(theta1)];
R(:,:,2)=[cosd(theta2) sind(theta2);-sind(theta2) cosd(theta2)];

Dx=zeros(Ny+1,Nx+1);%
Dy=zeros(Ny+1,Nx+1);

for j=1:2 %solves for each magnet
    Rj=R(:,:,j);%Works through rotation matrices
    Rt=Rj';%Transpose of rotation matrices
    for i=1:N
        pm=m(j,:); %calls position of magnet
        pp=pc(i,:);%calls position of point
        rv = pp-pm; % R vector global coordinates
        rvr=Rj*rv';%Rotates R vector to local coordinates
        r=norm(rv);%takes magnitude of R
        costheta = rvr(1)/r; %solves for angles
        sintheta=rvr(2)/r;
        cosphi=0;
        sinphi=1;
        if r > .2 %Filters out large vectors R
            Bx=mu/r^3*(2*costheta^2-sintheta^2); %solves for B field in
local
            By=mu/r^3*(3*costheta*sintheta*sinphi);
            Bz=mu/r^3*(3*costheta*sintheta*cosphi);
        else
            Bx = 0;
            By = 0;
            Bz = 0;
        end
        B=[Bx By]; %Organizes B field
        BG=Rt*B'; %solves B field in Global
    end
end

```

```

        Dx(i)=Dx(i) + BG(1); %Moves through each point and solves B
field
        Dy(i)=Dy(i) + BG(2);
    end
end

pcx=pc(:,1);%calls point position
pcy=pc(:,2);

u = Dx(:);%calls B field values
v = Dy(:);
un=u./sqrt(u.^2+v.^2);
vn=v./sqrt(u.^2+v.^2);

figure(); %plots B field with respect to position
%quiver(pcx, pcy, u, v);
quiver(pcx, pcy, un, vn);
xlabel('l_x');
ylabel('l_y');
title('Two Cylindrical Magnets');
hold on

    pos = [.75 2.75 .5 .5];
    rectangle('Position',pos,'Curvature',[1
1],'facecolor','k','EdgeColor','b',...
'LineWidth',3)
    axis equal
    hold on
    pos = [2 2.75 .5 .5];
    rectangle('Position',pos,'Curvature',[1
1],'facecolor','k','EdgeColor','b',...
'LineWidth',3)
    axis equal
xlim([.25, 3.1]);
ylim([1.9, 4.1]);

```

A.5 Halbach Vector Plot

```

mu=1386532.885;%Constant C for B Field
l_x=6;%domain size
l_y=4;
Nx=40;%number of domain points
Ny=40;
deltax=l_x/Nx;%number of points per unit L
deltay=l_y/Ny;
N=(Nx+1)*(Ny+1);%total number of points in domain
pc=zeros(N,2);%point coords
c=1;
for j=0:Nx % creates a domain
    for i=0:Ny

```

```

        pc(c,1)=j*deltax;
        pc(c,2)=l_y-i*deltay;
        c=c+1;
    end
end

m=[1 3;1.5 3;2 3;2.5 3; 3 3];%magnet position
R=zeros(2,2,5);%creates array for rotation matrix
R(:,:,1)=[1 0;0 1];%Rotation matrices
R(:,:,2)=[0 1;-1 0];
R(:,:,3)=[-1 0;0 -1];
R(:,:,4)=[0 -1;1 0];
R(:,:,5)=[1 0;0 1];
Dx=zeros(Ny+1,Nx+1);%
Dy=zeros(Ny+1,Nx+1);

for j=1:5 %solves for each magnet
    Rj=R(:,:,j);%Works through rotation matrices
    Rt=Rj';%Transpose of rotation matrices
    for i=1:N
        pm=m(j,:); %calls position of magnet
        pp=pc(i,:);%calls position of point
        rv = pp-pm; % R vector global coordinates
        rvr=Rj*rv';%Rotates R vector to local coordinates
        r=norm(rv);%takes magnitude of R
        costheta = rvr(1)/r; %solves for angles
        sintheta=rvr(2)/r;
        cosphi=0;
        sinphi=1;
        if r > .2 %Filters out large vectors R
            Bx=mu/r^3*(2*costheta^2-sintheta^2); %solves for B field in
local
            By=mu/r^3*(3*costheta*sintheta*sinphi);
            Bz=mu/r^3*(3*costheta*sintheta*cosphi);
        else
            Bx = 0;
            By = 0;
            Bz = 0;
        end
        B=[Bx By]; %Organizes B field
        BG=Rt*B'; %solves B field in Global

        Dx(i)=Dx(i) + BG(1); %Moves through each point and solves B
field
        Dy(i)=Dy(i) + BG(2);
    end
end

pcx=pc(:,1);%calls point position
pcy=pc(:,2);

u = Dx(:);%calls B field values
v = Dy(:);

```

```

%un=u./sqrt(u.^2+v.^2);
%vn=v./sqrt(u.^2+v.^2);

figure(); %plots B field with respect to position
quiver(pcx, pcy, u, v);
xlabel('l_x');
ylabel('l_y');
title('Halbach Array Vector Field');
hold on
rectangle('Position',[.75,2.75,.5,.5],'facecolor','k','EdgeColor','b',...
...
'LineWidth',3)
hold on
rectangle('Position',[1.25,2.75,.5,.5],'facecolor','k','EdgeColor','b',...
...
'LineWidth',3)
hold on
rectangle('Position',[1.75,2.75,.5,.5],'facecolor','k','EdgeColor','b',...
...
'LineWidth',3)
hold on
rectangle('Position',[2.25,2.75,.5,.5],'facecolor','k','EdgeColor','b',...
...
'LineWidth',3)
hold on
rectangle('Position',[2.75,2.75,.5,.5],'facecolor','k','EdgeColor','b',...
...
'LineWidth',3)

xlim([.25, 3.75]);
ylim([1.9, 4.1]);

```


Appendix B Initial Testing

Tests were run to determine the viability of the dual rotating magnet system. Two are high-lighted below.

Three Buried Objects

Three different objects were buried in the test bed. A 2ft by 1in diameter iron pipe, a 1ft by 3in diameter steel cylinder and a 5-pound dumbbell with a 6.25-inch diameter. They were orientated as pictured in Figure 94. The unit was run in the x direction from one end of the sand box to the other. The following plotted data is the magnitude of the magnetic field recorded by the USB2510A magnetometer.

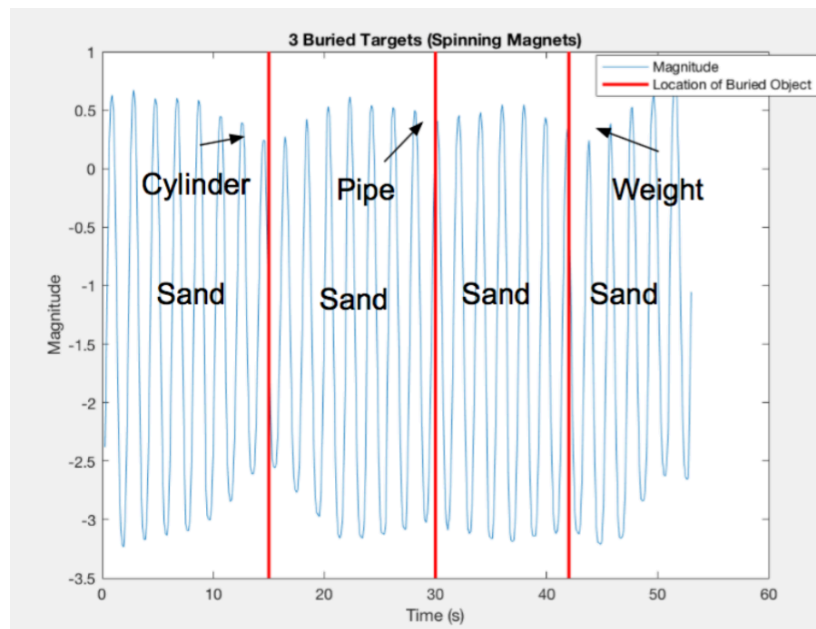


Figure 137: Initial 3 Buried Object Test

In Figure 137 the location of the three buried objects are labeled. The location of the buried targets is where the magnetometer reading drops of in a parabola shape. The center of the parabola or axis of symmetry is where the middle of the object lies. The depth

of the parabola determines the size and magnetic strength of the object. The results show the ability of the unit to accurately sense and locate underground infrastructure.

Martian Soil Test

In an effort to create a Martian soil simulate, steel wool was mixed in with sand in a sealed bag. Two bags with this mixture were placed in the sandbox 2 feet apart with an air pocket in between, as pictured in Figure 34. This simulates a water or air pocket beneath the Martian surface. The following plots are from the recorded magnetometer data.

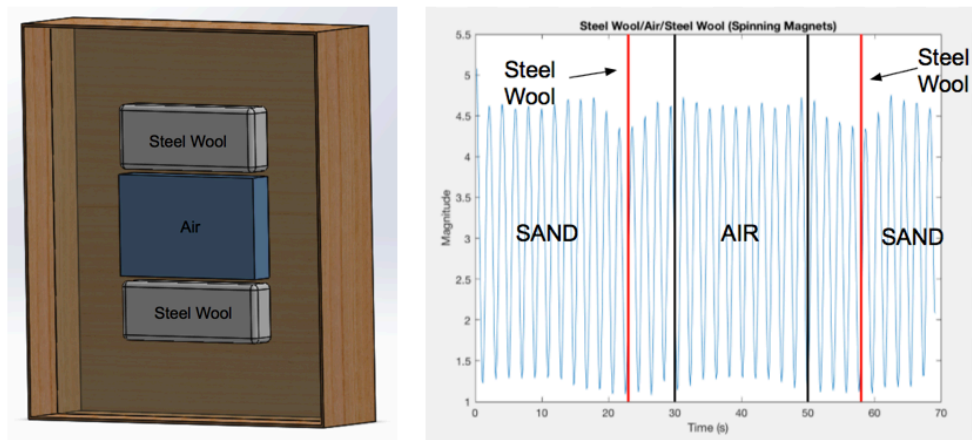


Figure 138: Initial Martian Soil Test

Figure 138 shows the location of the two steel wool mixtures and the air pocket. Again, where the magnetometer magnitude drops off is the location of the steel wool mixture. The depth of the two upside down parabolas varies because the steel wool mixture on the left side of the graph has more steel wool in it, making it more magnetic. This makes the magnitude reading drop off more when the dual rotating unit senses the steel wool mixture. The results show the ability of the unit to sense and locate the abnormalities in the Martian surface.

Appendix C Additional Results

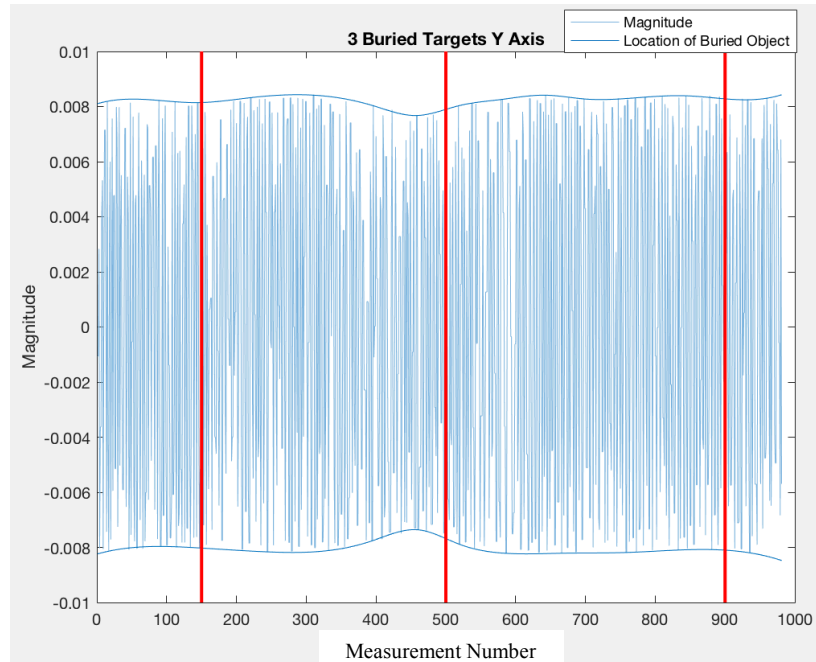


Figure 139: 3 Buried Targets Recorded Y Axis Data

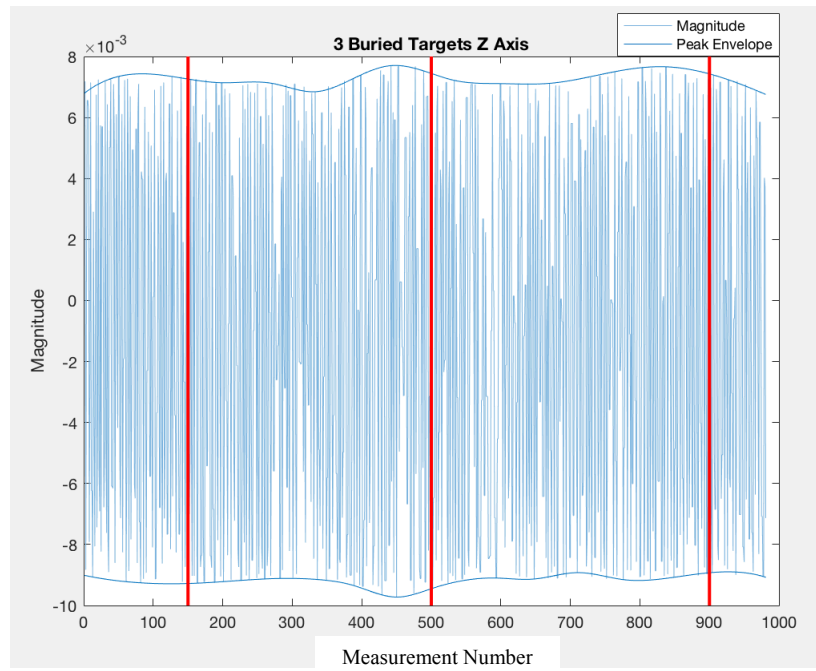


Figure 140: 3 Buried Targets Recorded Z Axis Data

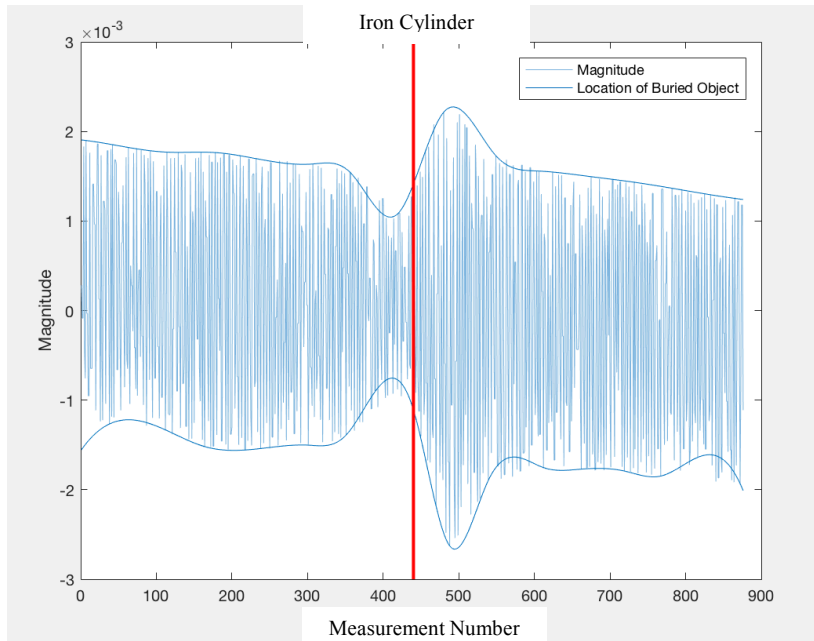


Figure 141: Iron Cylinder Recorded X Axis Data

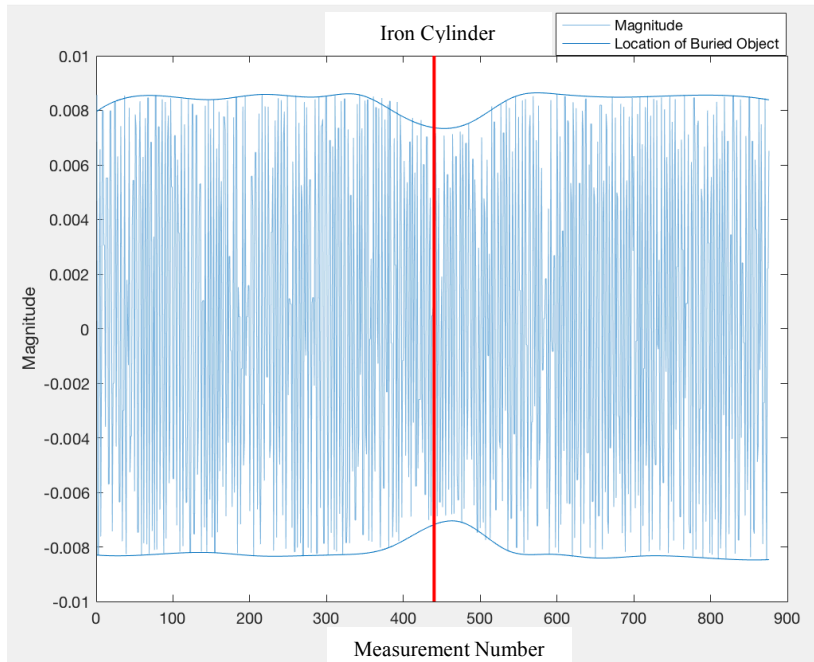


Figure 142: Iron Cylinder Recorded Y Axis Data

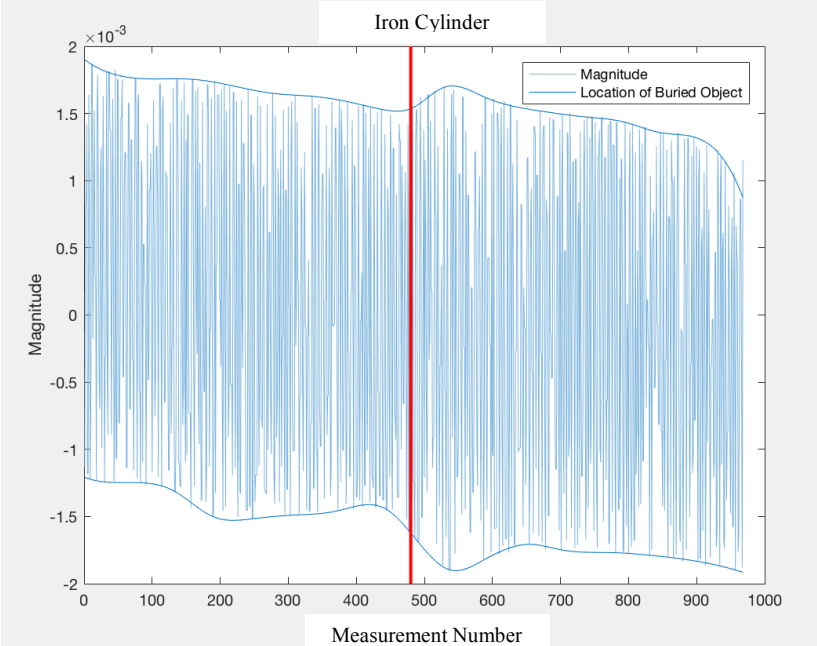


Figure 143: Iron Cylinder Recorded X Axis Data

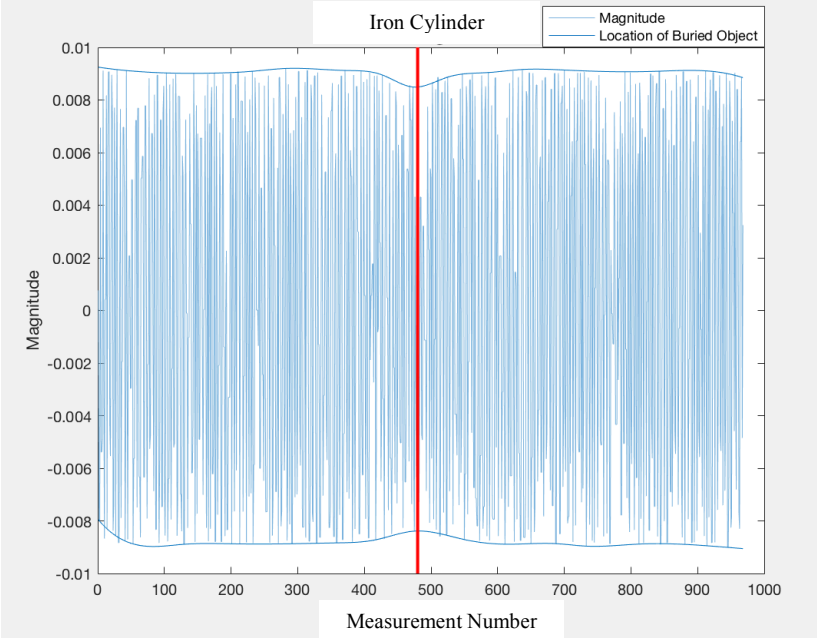


Figure 144: Iron Cylinder Recorded Y Axis Data

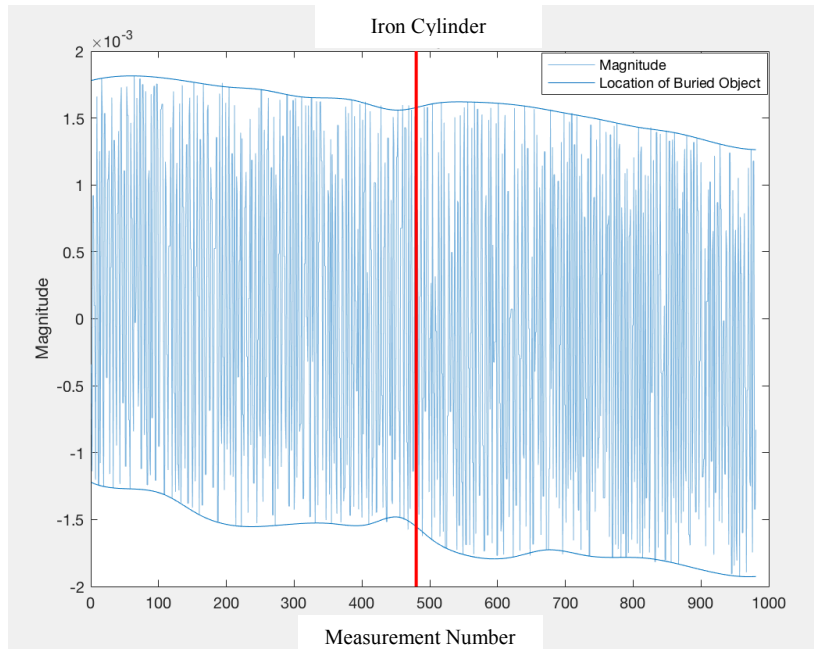


Figure 145: Iron Cylinder Recorded X Axis Data

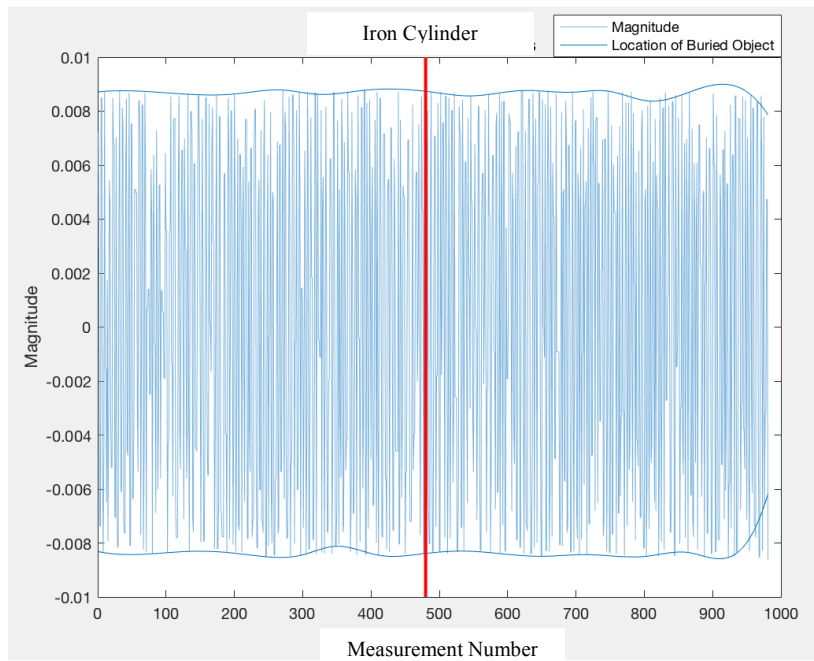


Figure 146: Iron Cylinder Recorded Y Axis Data

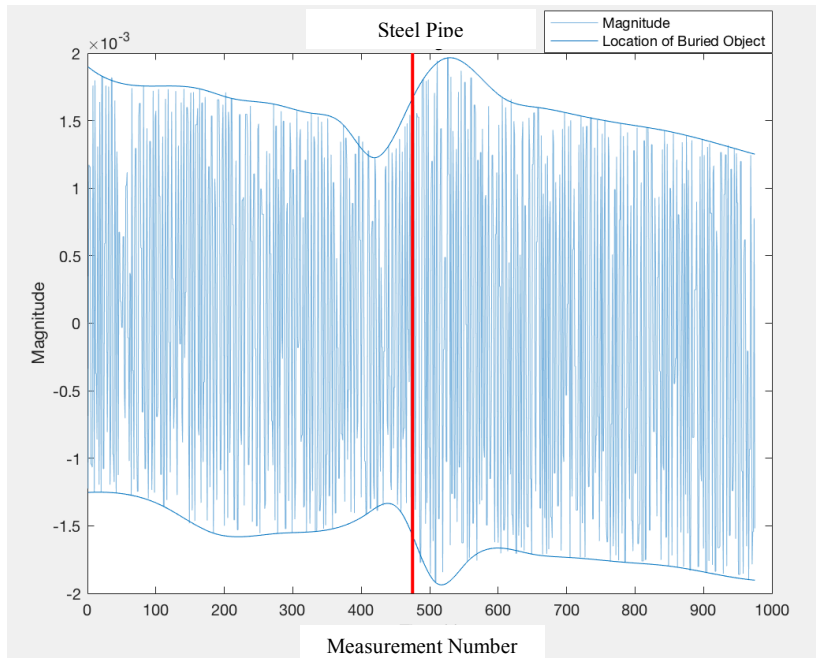


Figure 147: Steel Pipe Recorded X Axis Data

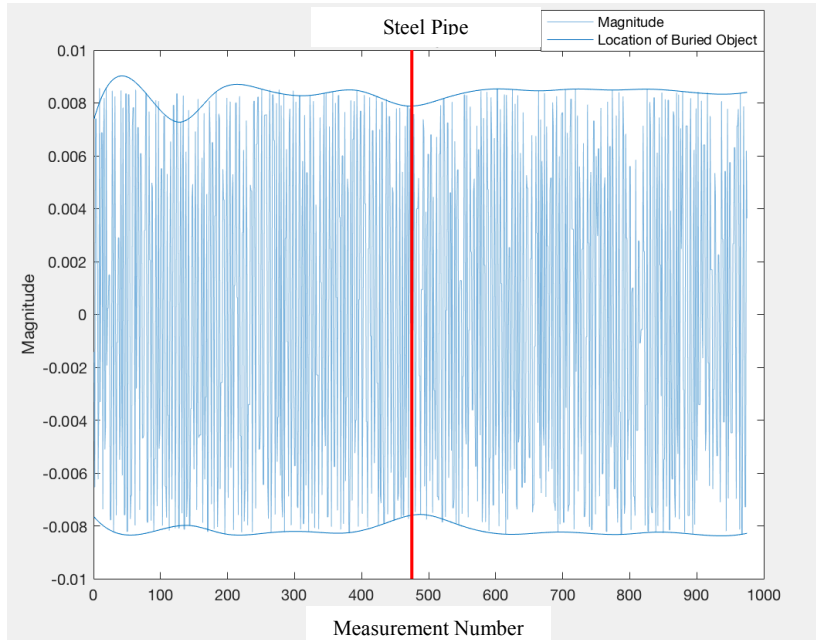


Figure 148: Steel Pipe Recorded Y Axis Data

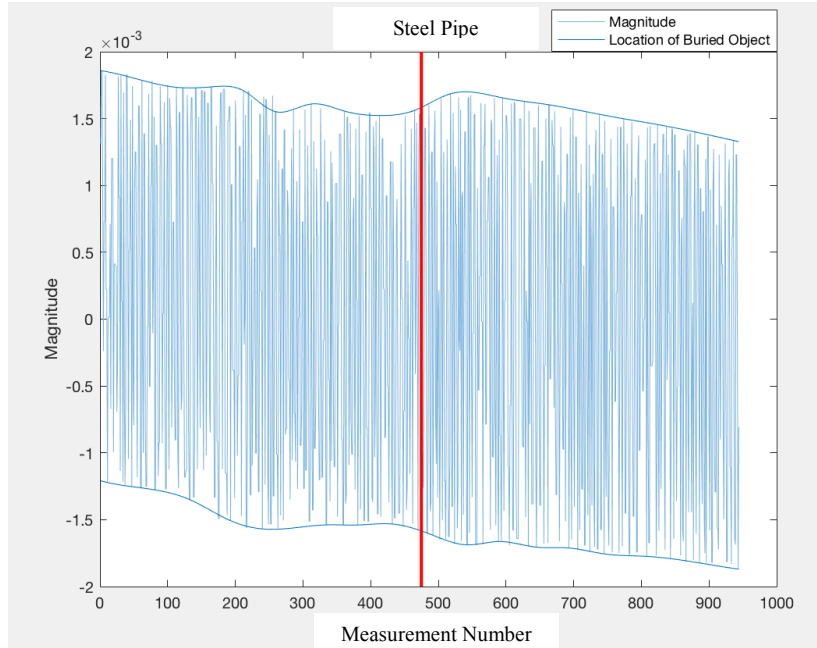


Figure 149: Steel Pipe Recorded X Axis Data

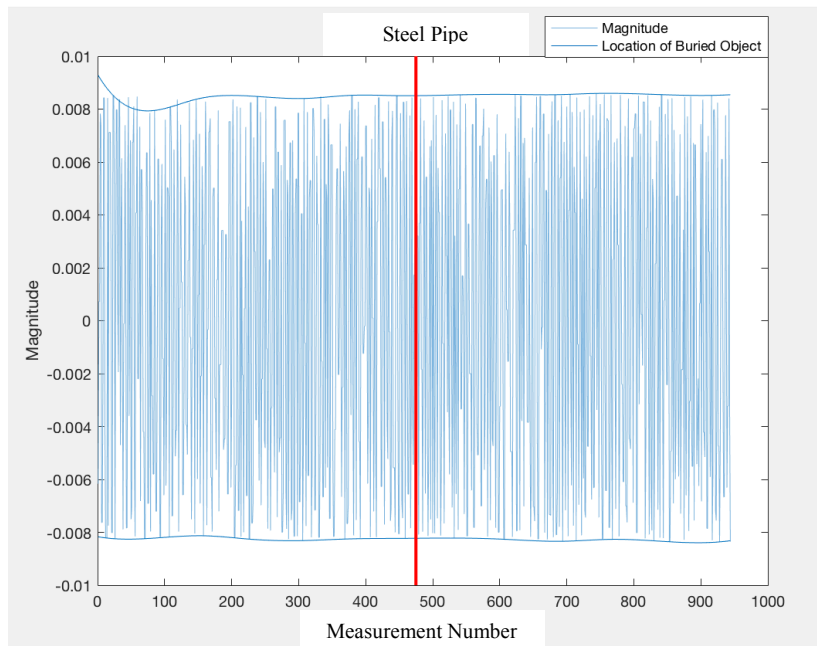


Figure 150: Steel Pipe Recorded Y Axis Data

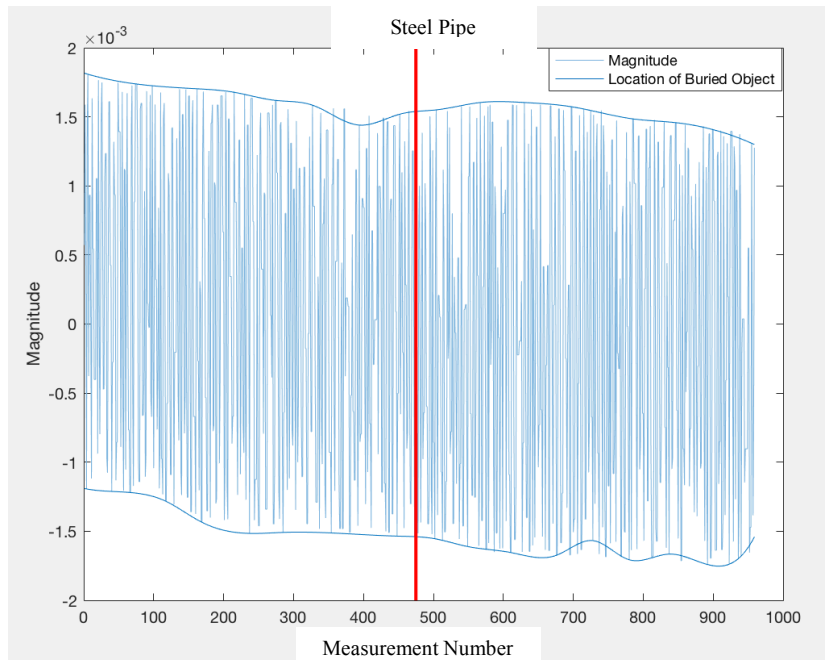


Figure 151: Steel Pipe Recorded X Axis Data

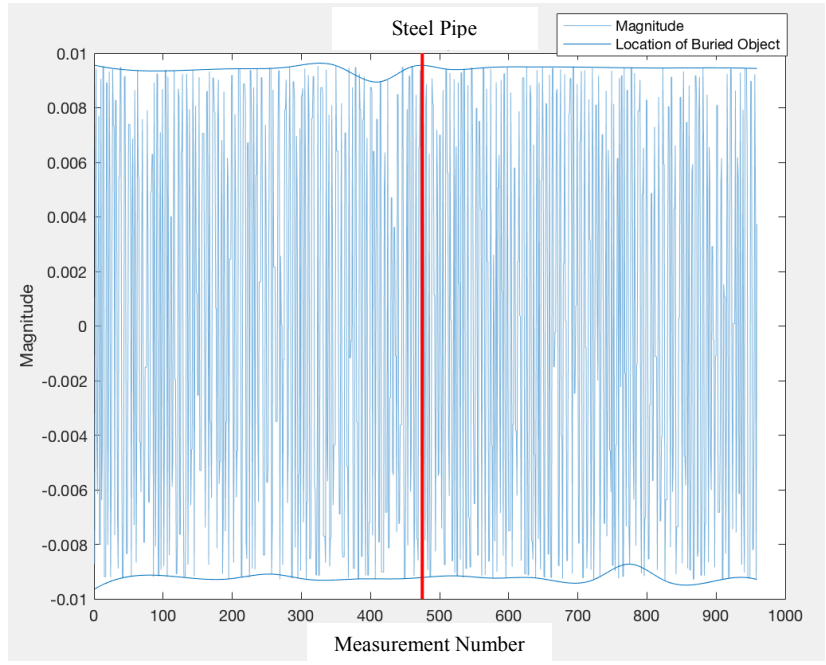


Figure 152: Steel Pipe Recorded Y Axis Data

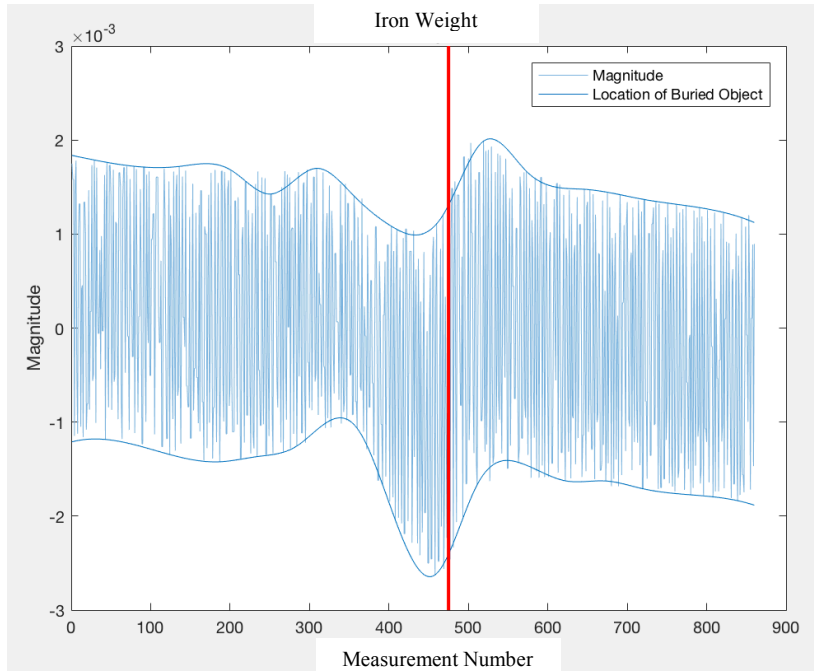


Figure 153: Iron Weight Recorded X Axis Data

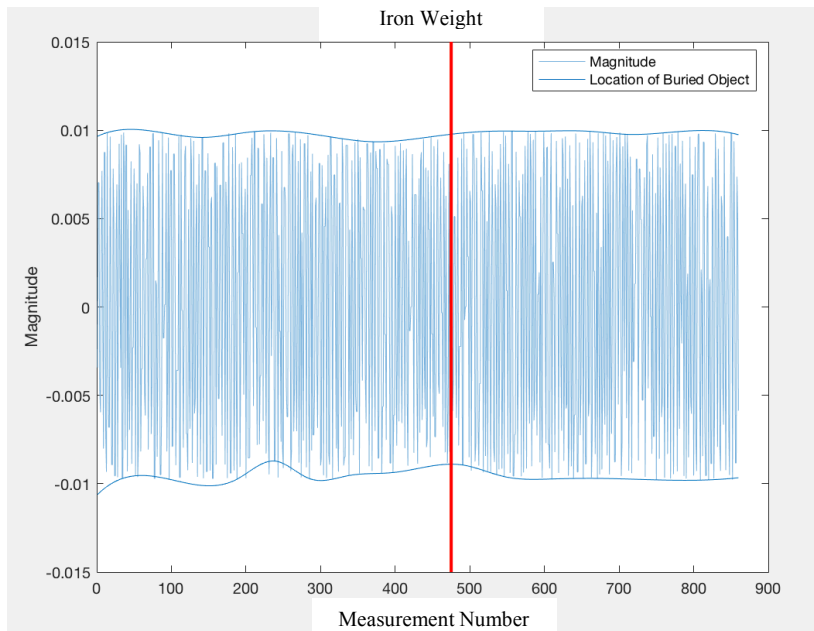


Figure 154: Iron Weight Recorded Y Axis Data

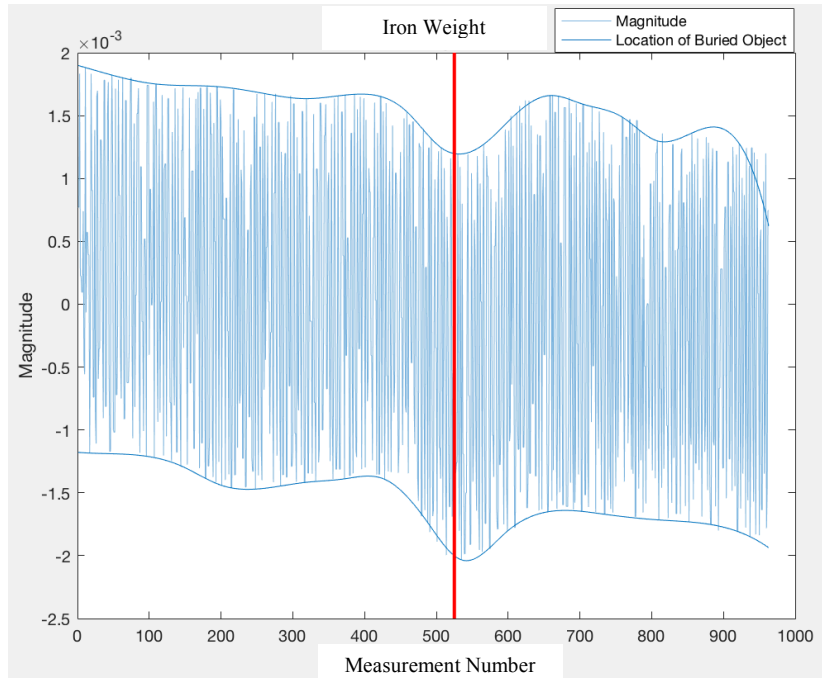


Figure 155: Iron Weight Recorded X Axis Data

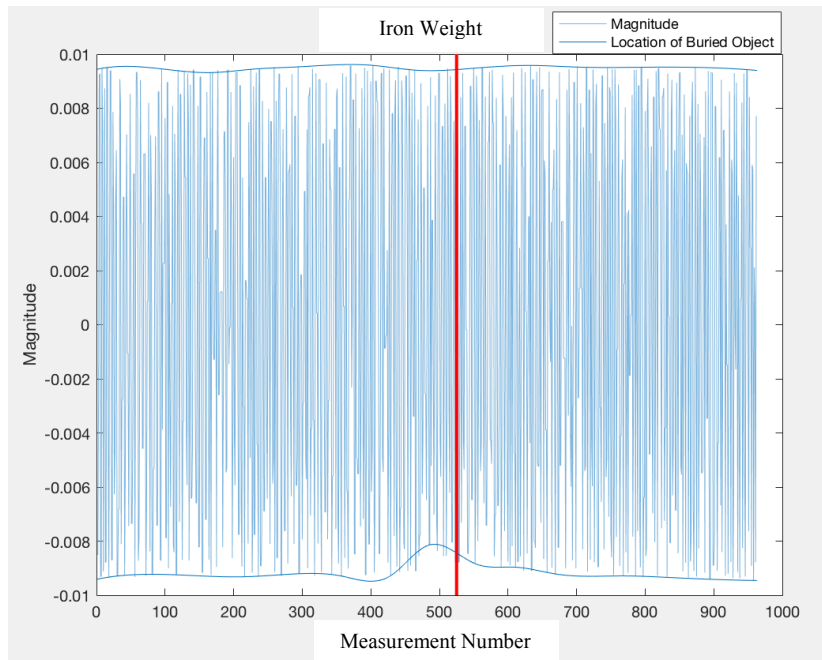


Figure 156: Iron Weight Recorded Y Axis Data

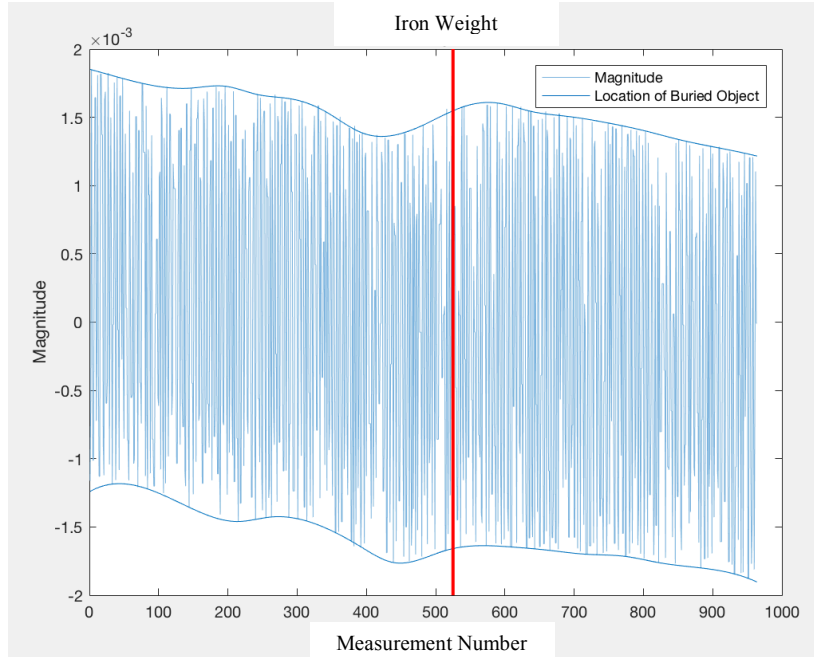


Figure 157: Iron Weight Recorded X Axis Data

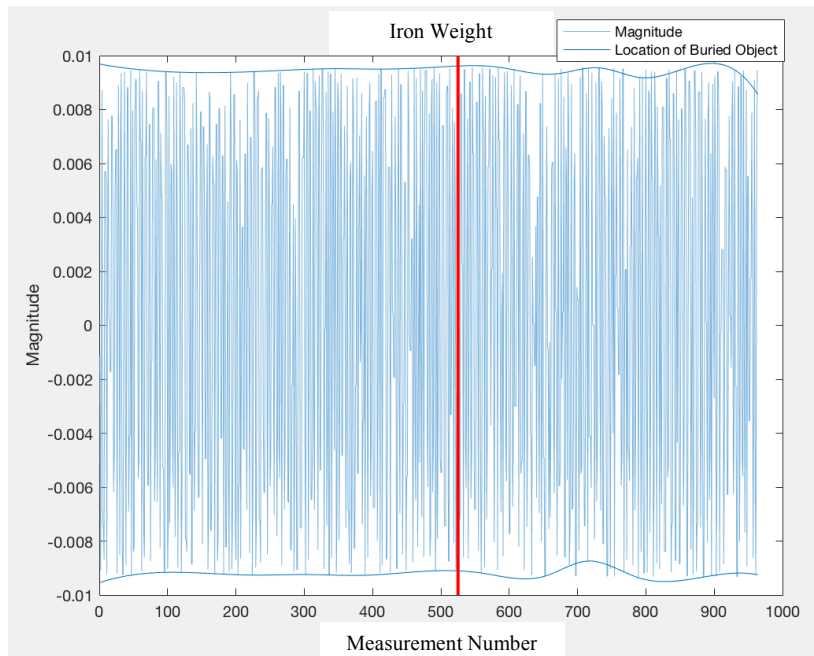


Figure 158: Iron Weight Recorded Y Axis Data

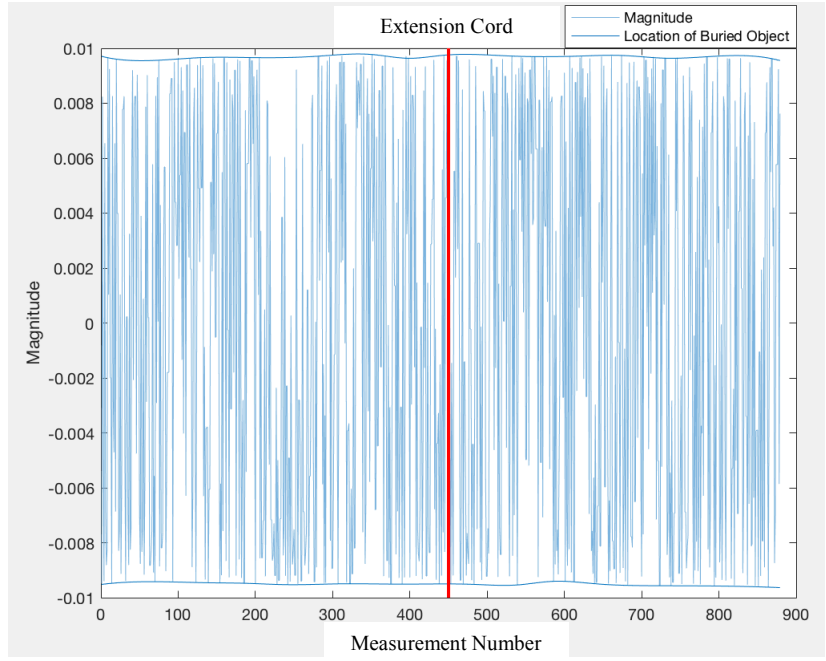


Figure 159: Extension Cord Recorded Y Axis Data

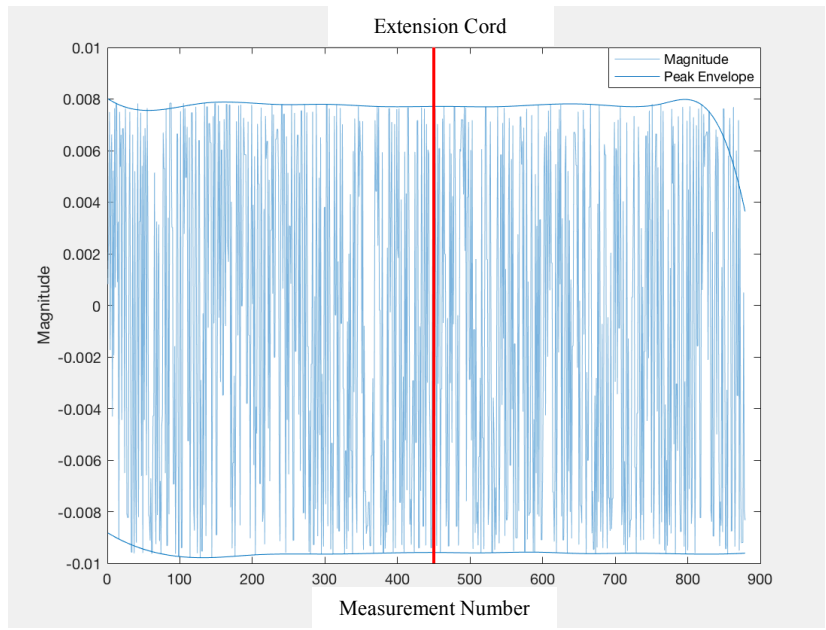


Figure 160: Extension Cord Recorded Z Axis Data

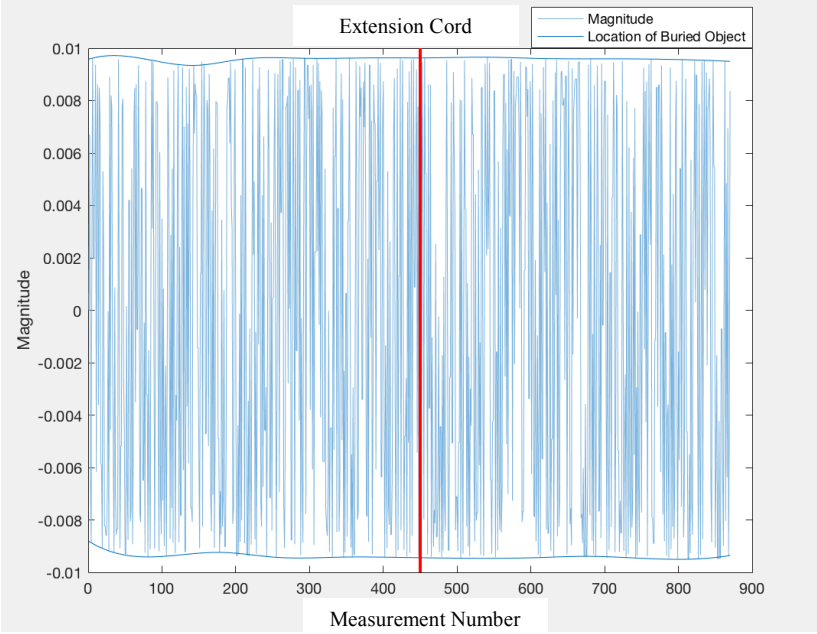


Figure 161: Extension Cord Recorded Y Axis Data

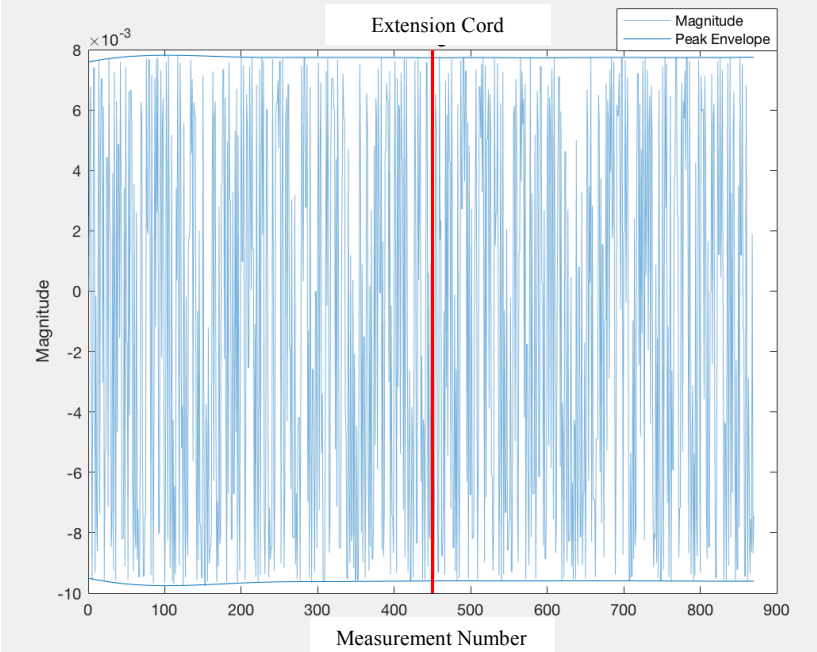


Figure 162: Extension Cord Recorded Z Axis Data

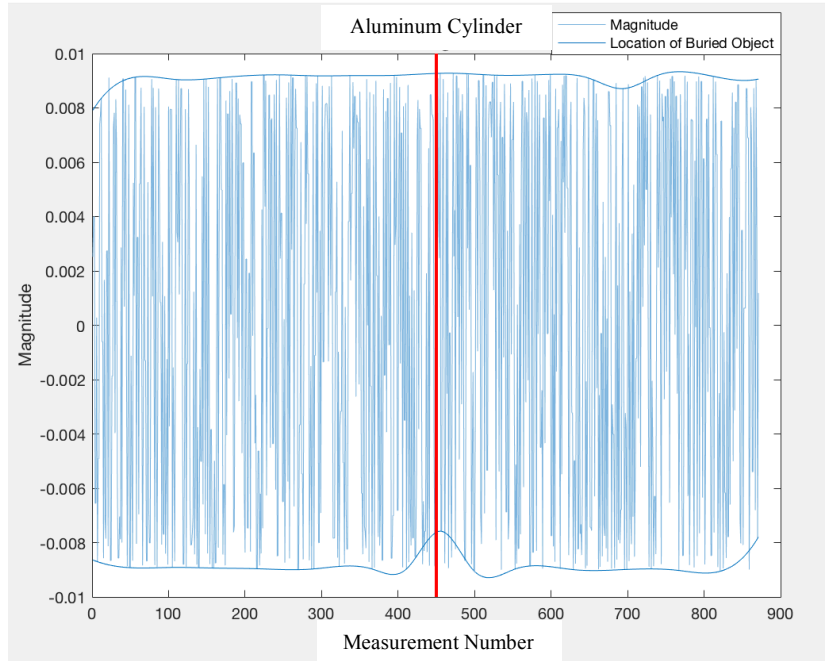


Figure 163: Aluminum Recorded Y Axis Data

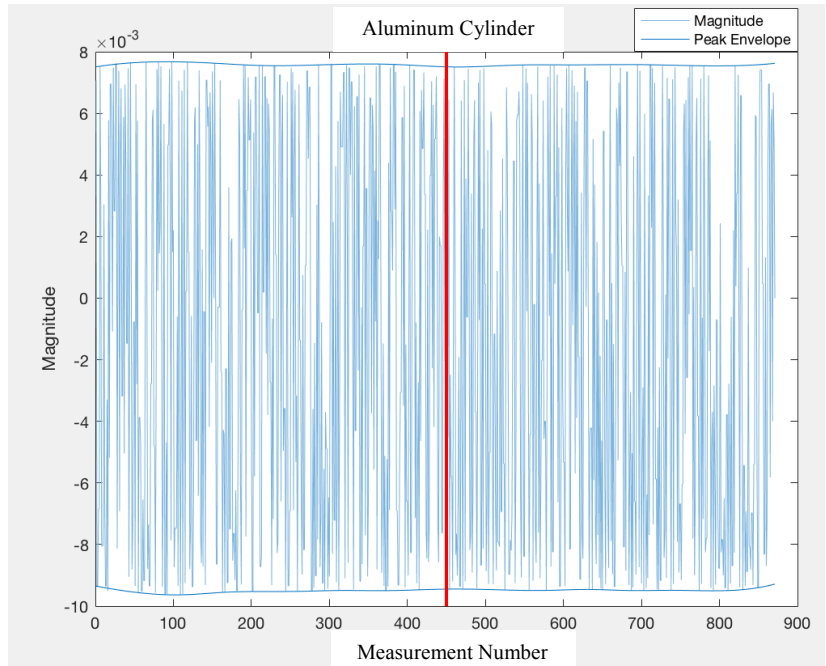


Figure 164: Aluminum Recorded Z Axis Data

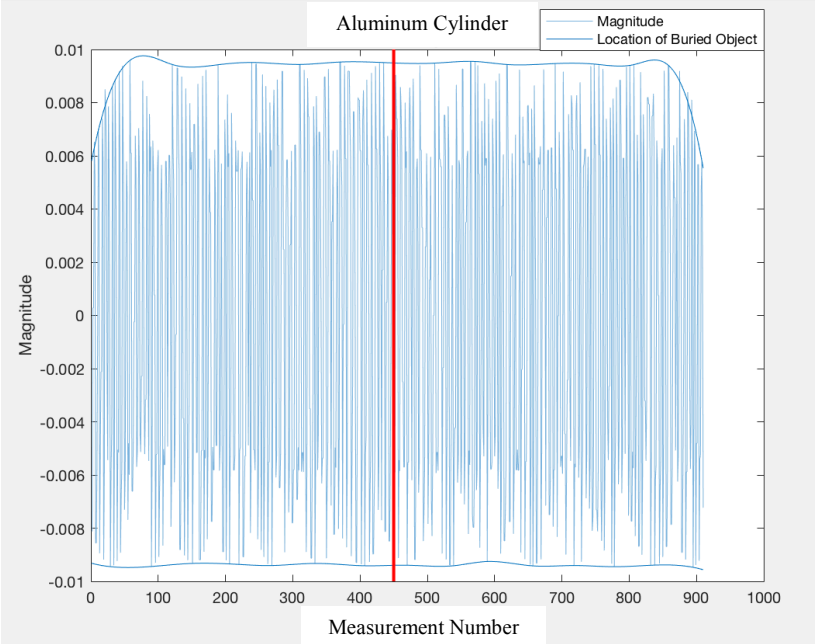


Figure 165: Aluminum Recorded Y Axis Data

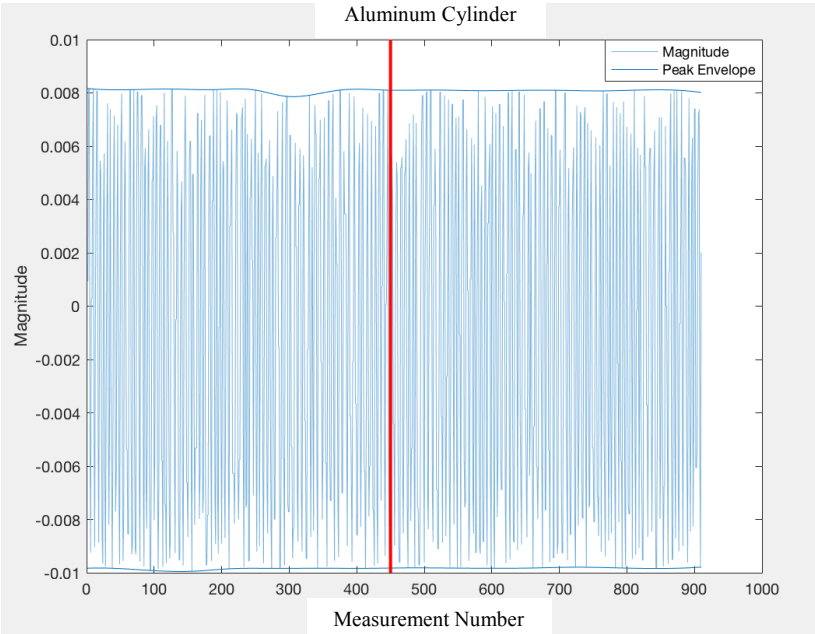


Figure 166: Aluminum Recorded Z Axis Data

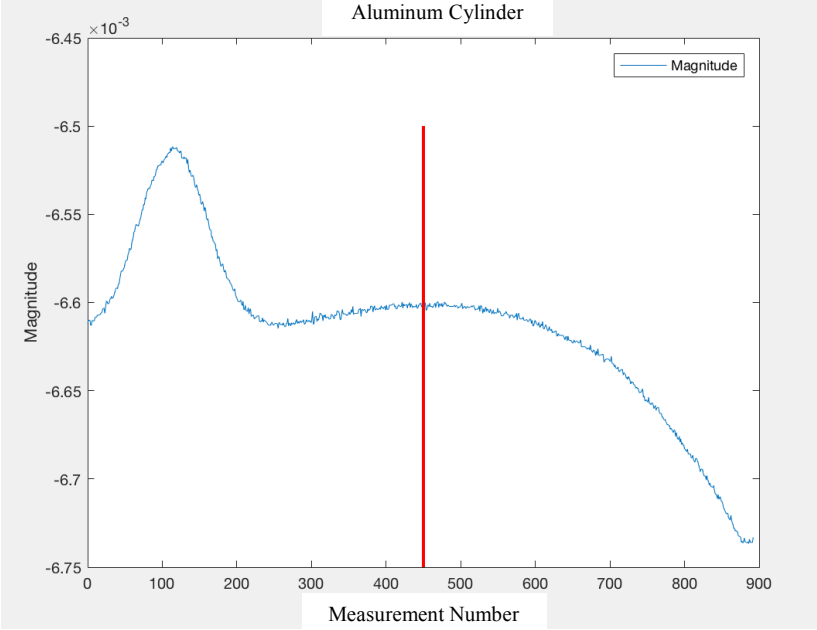


Figure 167: Aluminum Recorded Y Axis Data

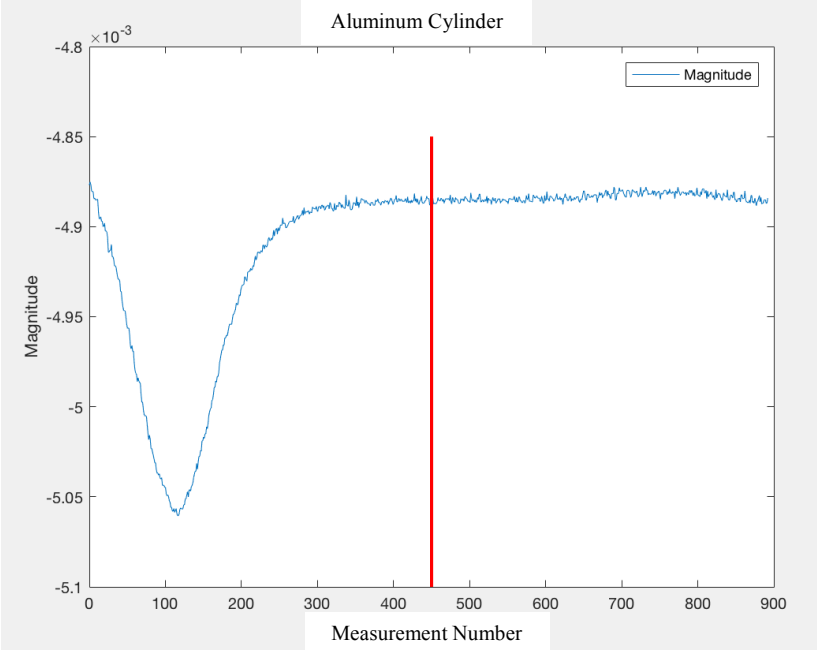


Figure 168: Aluminum Recorded Z Axis Data

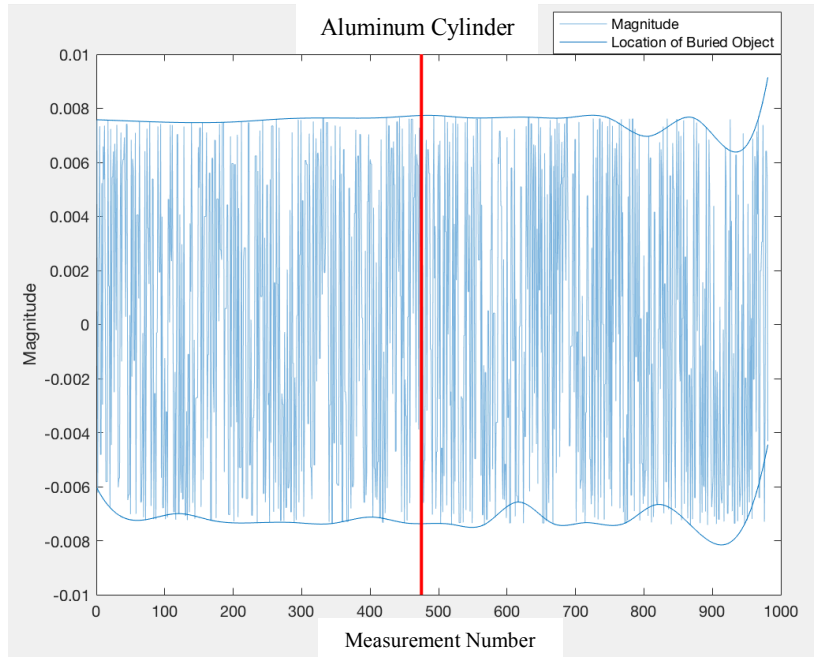


Figure 169: Aluminum Recorded Y Axis Data

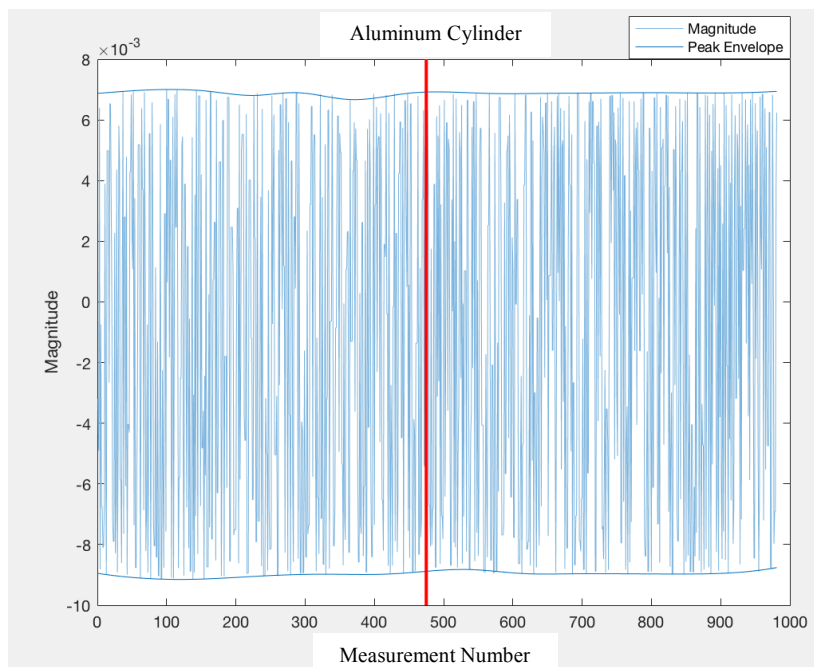


Figure 170: Aluminum Recorded Z Axis Data

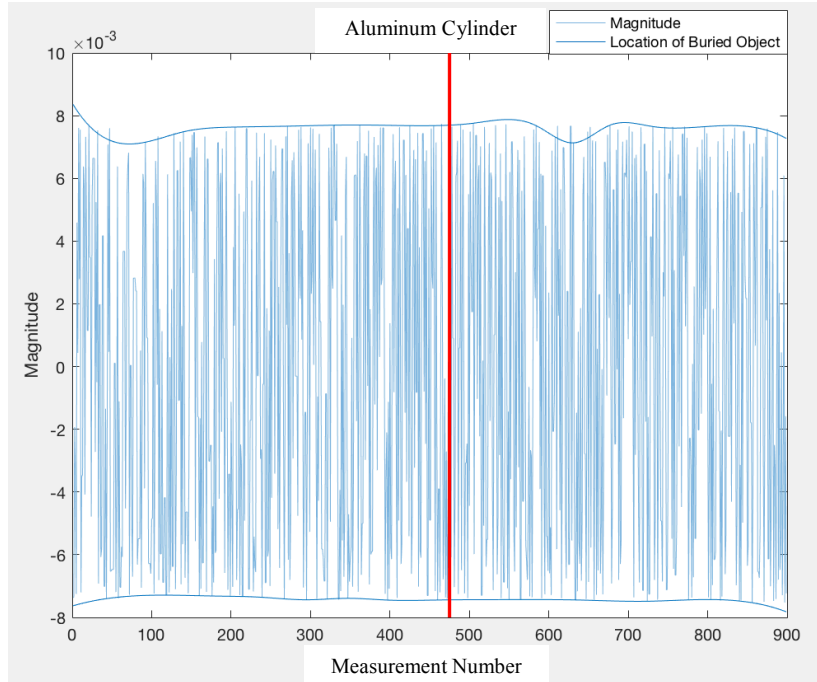


Figure 171: Aluminum Recorded Y Axis Data

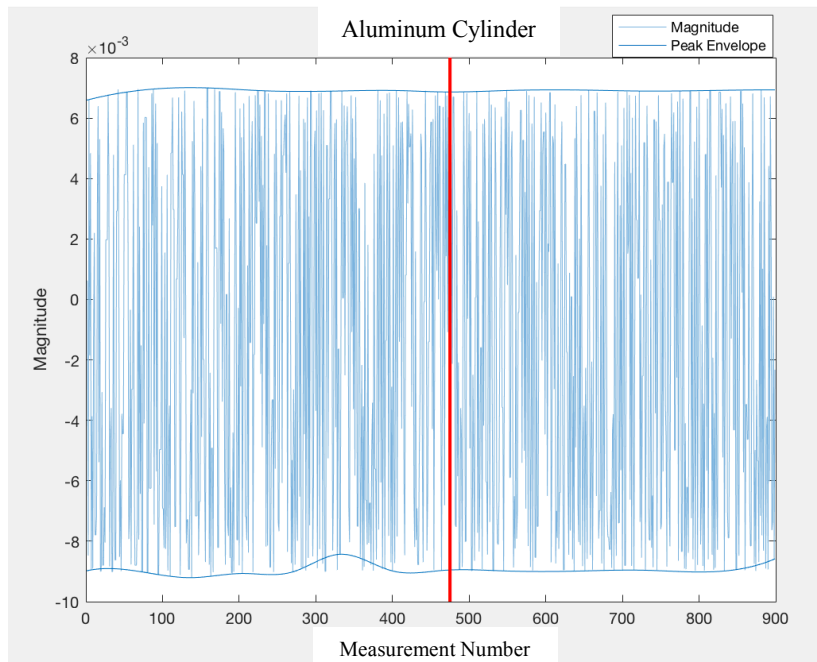


Figure 172: Aluminum Recorded Z Axis Data

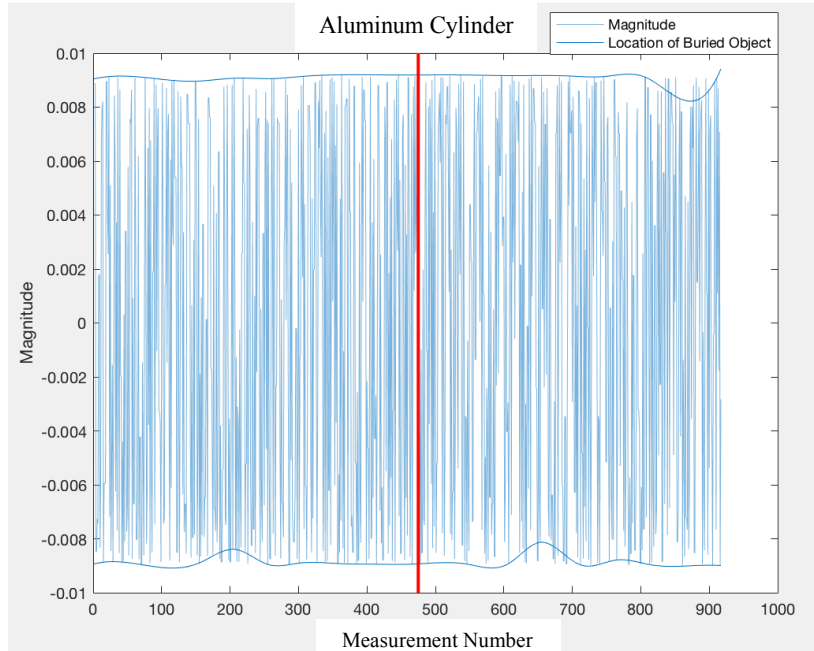


Figure 173: Aluminum Recorded Y Axis Data

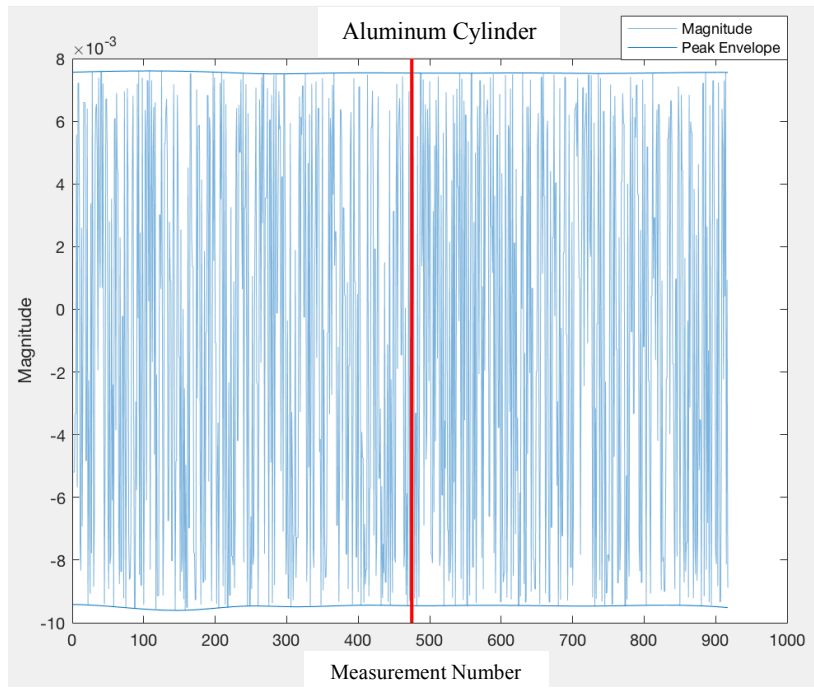


Figure 174: Aluminum Recorded Z Axis Data

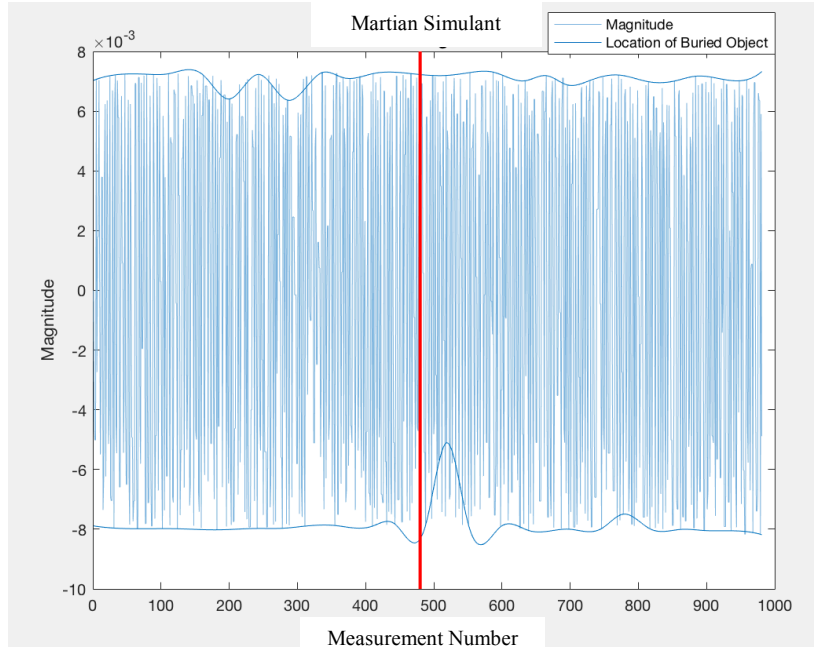


Figure 175: Martian Simulant Y Axis Test 1

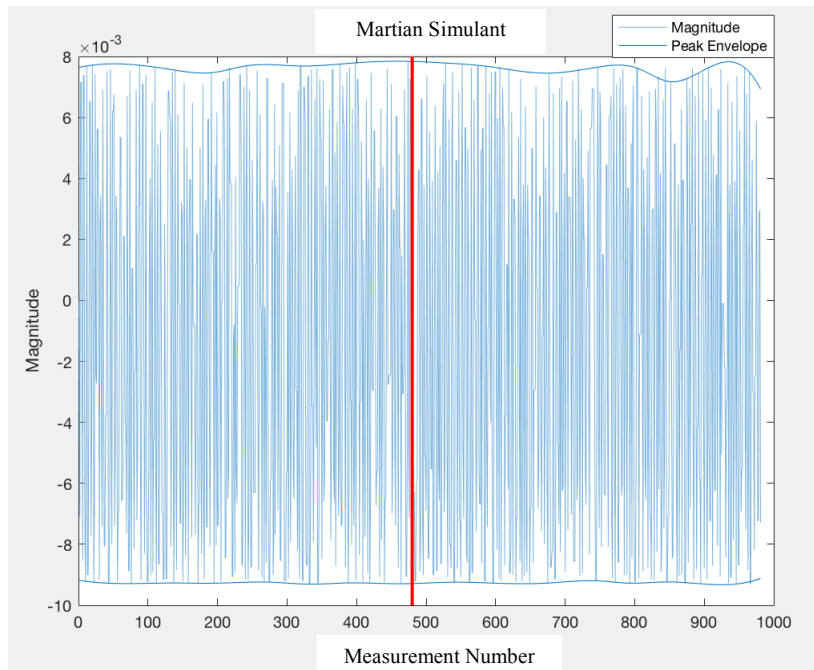


Figure 176: Martian Simulant Z Axis Test 1

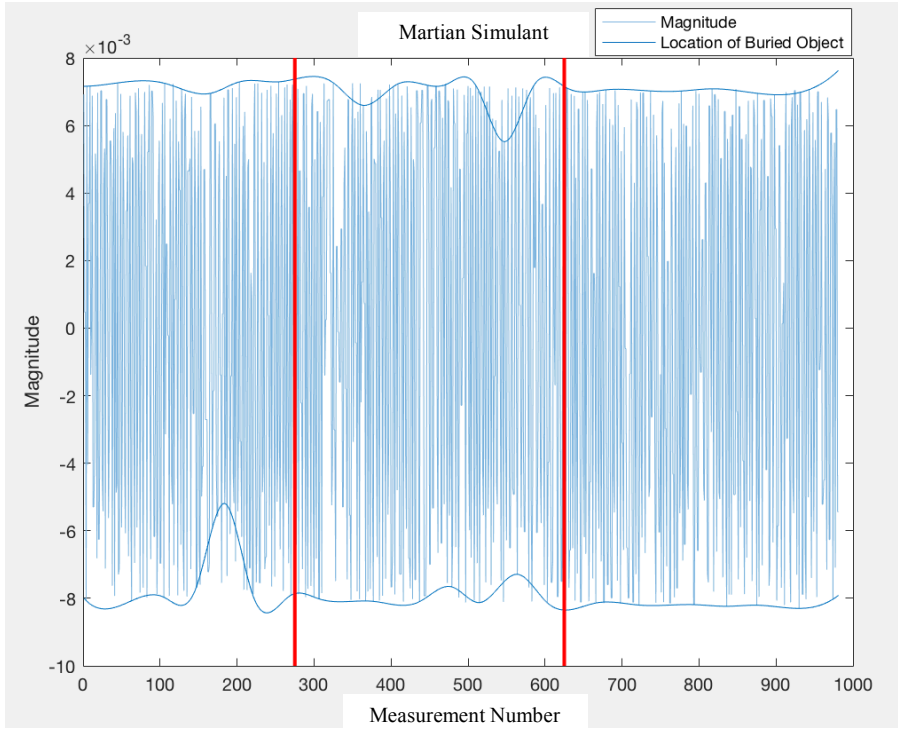


Figure 177: Martian Simulant Y Axis Test 2

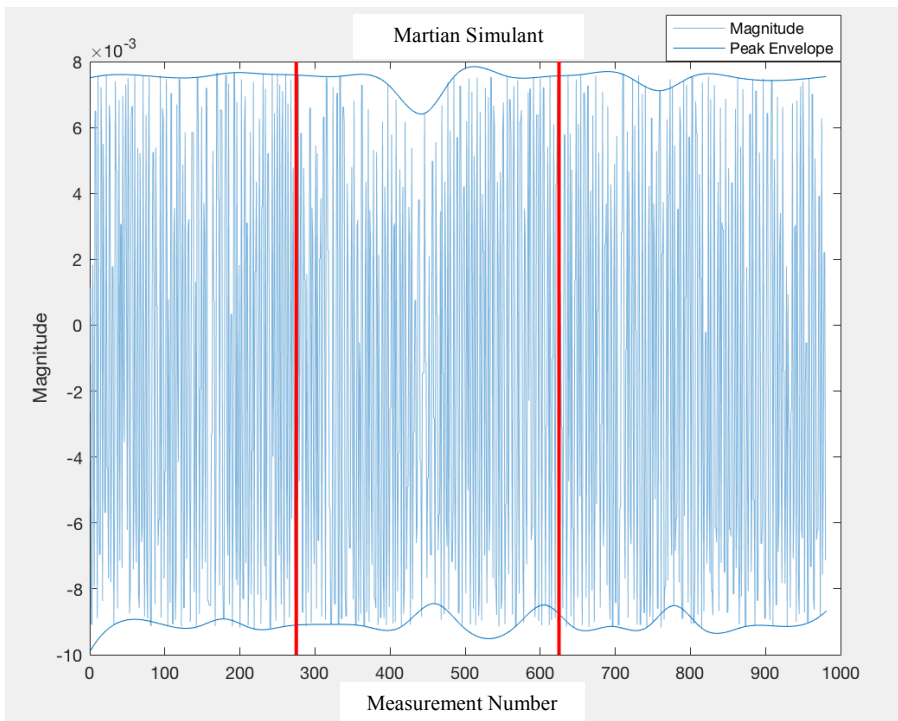


Figure 178: Martian Simulant Z Axis Test 2

Appendix D Additional SolidWorks Models

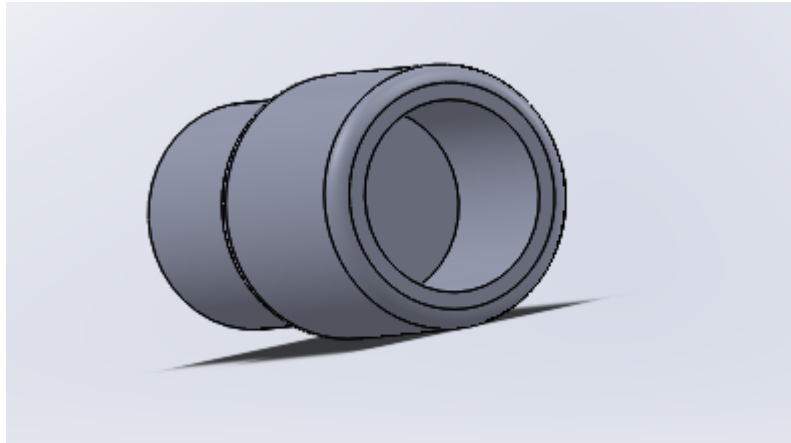


Figure 179: SolidWorks Model of Magnet Holder

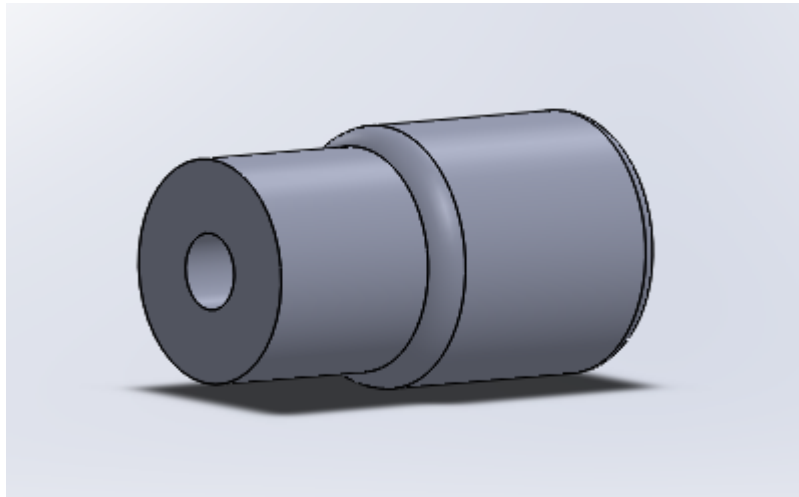


Figure 180: SolidWorks Model of Magnet Holder

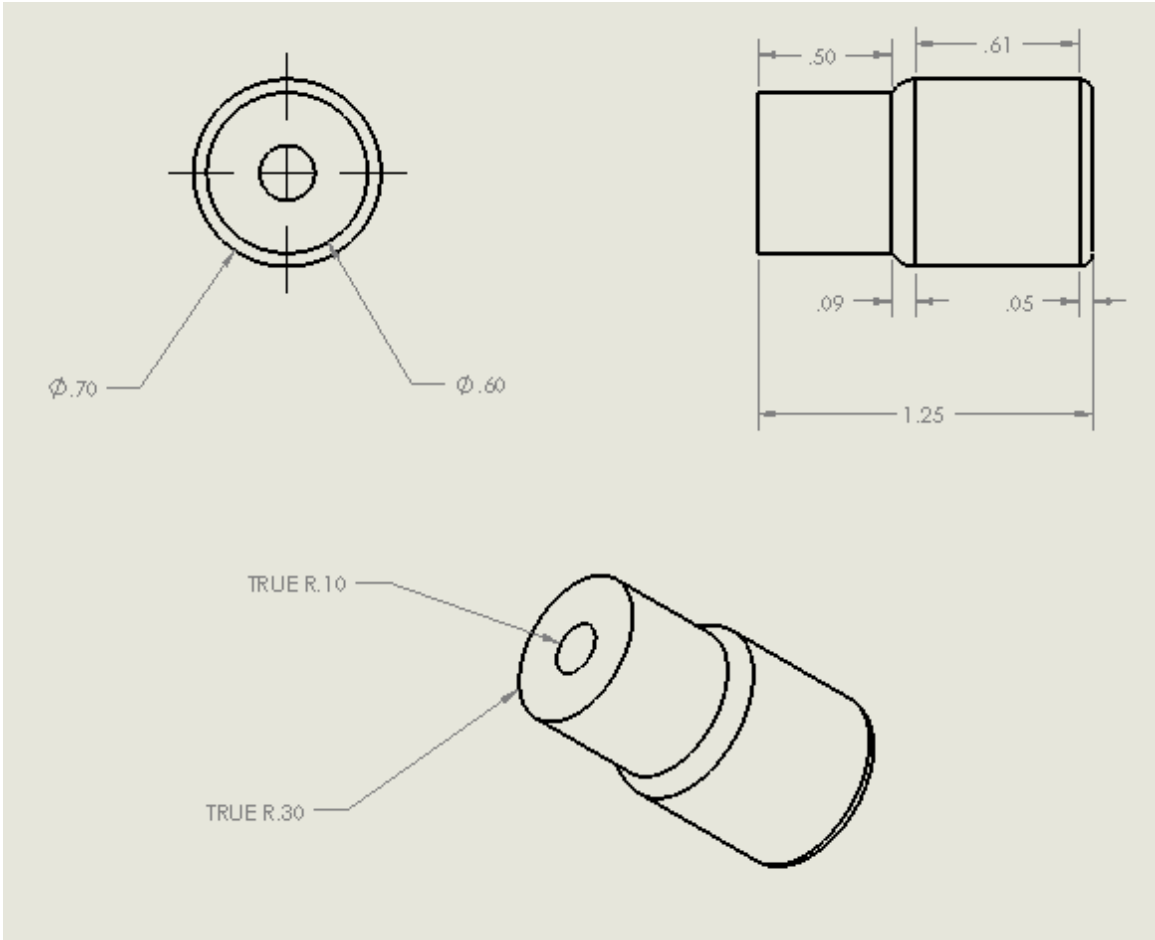


Figure 181: Dimensioned Schematic of Magnet Holder